SENSITIVITY AND EVANESCENT FIELD STUDY OF A UNIAXIAL ANISOTROPIC PLANAR WAVEGUIDE BASED OPTICAL SENSOR[†]

Abdelbaki Cherouana[a], Idris Bouchama[b,c], Abdelhalim Bencheikh[d], Samah Boudour[e,*], Muhammad Saeed Akhtar[f]

[a]*Research Unit in Optics and Photonics – University of Sétif 1, Center for development of advanced technologies, Algiers, Algeria*
[b]*Department of Electronic, Faculty of Technology, University of Msila, Msila, Algeria*
[c]*Research Unit on Emerging Materials (RUEM), University Ferhat Abbas, Setif, Algeria*
[d]*Department of Electromechanics, University of BBA, Algeria*
[e]*Research Center in Industrial Technologies CRTI, P.O. Box 64, Cheraga 16014, Algiers, Algeria*
[f]*Department of Physics, University of Education, Lahore, 54770, Pakistan*
Corresponding authors: Dr. Samah Boudour, Research Center in Industrial Technologies CRTI, P.O. Box 64, Cheraga, 16014, Algiers, Algeria. E-mail: s.boudour@crti.dz

The effect of source, geometrical and physical parameters of slab waveguide on the sensitivity of optical sensor and its evanescent field have been investigated. The wave guiding film was the LiNbO₃ and the observations revealed that, the maximal sensitivities of Transverse Magnetic (TM) modes and their corresponding frequencies are greater than those for Transverse Electric (TE) modes. Furthermore, the optimal source parameters improve the maximal sensitivity and evanescent field in the cover. However, the increment in the core thickness reduces the sensitivity of sensor due to reduction in evanescent field in the cover. The sensitivity of sensor was observed as a function of refractive indices of cover, core and the substrate. The increase in refractive indices of cover and core, directly affect the sensitivity while an inverse relation has been observed regarding increase in the refractive index of the substrate. It is worth noting that, any changes in the physical parameters of waveguide sensor show insignificant effect on the evanescent fields.
Keywords: *Planar waveguide sensor; Birefringence; Source parameters; Geometrical and physical parameters; Sensor sensitivity; Evanescent field*
PACS: 42.25.-p, 42.25.Bs, 42.82.Et, 87.85.fk, 07.07.Df, 42.82.-m, 42.81.Gs, 42.79.Pw

Planar waveguide based optical sensors use the exponential decay of evanescent field in the external medium, to sense alterations occurring in the vicinity of a waveguide surface. This feature makes evanescent wave based optical sensor enable monitoring of chemical and biochemical interactions in real-time with high sensitivity and stability. Furthermore, sensors based on optical LOC systems would sense selective analytes just by choosing the appropriate biological receptors [1]. Recently, it has been reported that plasmonic and silicon photonics-based biosensors are among the most employed evanescent-wave biosensors to analyze nucleic acids with potential applicability in the clinical diagnosis [2]. In addition, Lithium Niobate (LN) is among one of the widely used materials for integrated sensor applications due to its excellent optical, ferroelectric, piezoelectric, and thermoelectric properties [3]. In fact, the fabrication of LiNbO₃ thin film crystals exhibiting optical properties comparable to those for bulk crystals along with coupled TE and TM modes [4]. Sensitivity, being most important parameter of an optical sensor has attracted significant research interest [5-7]. Thus, planar waveguides comprising left-handed material (LHMs) with different configurations [8], as well as binary and ternary photonic crystal with LHMs layers [9, 10]; have been investigated as optical sensors. It has also been observed that the sensitivity of the proposed structures can be significantly improved by the optimization of physical and geometrical parameters of the waveguide layers.

In this paper, the sensitivity and evanescent fields of a slab waveguide sensor constituted of uniaxial anisotropic crystals have been investigated. The influence of light source in addition to the physical and geometrical parameters of the waveguide, on the sensor sensitivity and evanescent fields have been studied in detail for the two kinds of modes propagating simultaneously in a waveguide. In our previous work [11], the influence of physical parameters was briefly studied.

THEORETICAL MODELING

The planar waveguide for an optical sensor was constituted by three layers of uniaxial crystals of lossless and non-magnetic materials, as presented in Fig. 1. The core refractive index tensor is $\overline{\overline{n_f}}$, whereas, the refractive index tensors of the media above and below the film guide are, respectively, $\overline{\overline{n_c}}$ and $\overline{\overline{n_s}}$. Then:

$$\overline{\overline{n_i}} = \varepsilon_0 \begin{bmatrix} n_i^2 & 0 & 0 \\ 0 & n_i^2 & 0 \\ 0 & 0 & n_{iz}^2 \end{bmatrix},$$

where, i = c, f, s (cover, film, substrate), ε_0 is the dielectric constant of vacuum, $n_i = n_{ix} = n_{iy}, n_{iz}$ are, ordinary and extraordinary refractive indices of each layer, respectively.
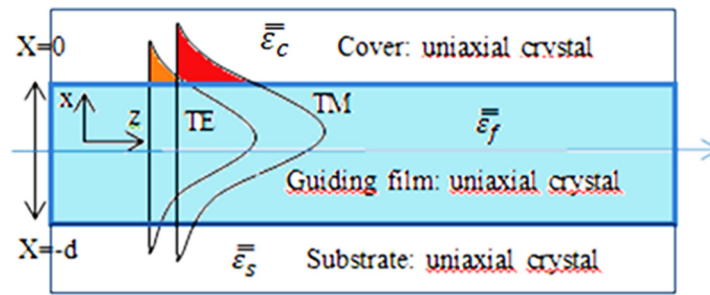
Figure 1. Uniaxial anisotropic slab waveguide-based sensor

Two waves (TE and TM) are propagated separately in the core of such slab waveguide, considered as an ordinary and extraordinary wave, respectively [12].

Sensitivity of a Birefringent Planar Waveguide Based Sensor

The sensitivity is defined as the rate of change in modal effective refractive index relative to the cover refractive index:

$$S = (\partial n_p / \partial N)^{-1},\tag{1}$$

The two expressions of the sensor sensitivity for both TE and TM modes are given as [12]:

$$S_{TE} = \sqrt{\frac{1-a_c}{1-X}} \frac{X}{a_c} \frac{1}{\sqrt{a_c-X}} \frac{1}{\left[T + \frac{1}{\sqrt{a_s-X}} + \frac{1}{\sqrt{a_c-X}}\right]},\tag{2}$$

where

$$T = k_0 d n_f = \frac{arctan\sqrt{\frac{a_s-X}{X}} + arctan\sqrt{\frac{a_c-X}{X}} + m\pi}{\sqrt{X}}.\tag{3}$$

For TE modes

$$S_{TM} = \frac{\frac{X(1-2X+a_c)\sqrt{1-a_c}}{\sqrt{1-X}\sqrt{a_c-X}[a_c(1-X(1-Xa_{cz}))-Xa_{cz}]}}{\left[T'K + \frac{a_c(1-a_c)}{\sqrt{(a_c-X)}[a_c(1-X(1-Xa_{cz}))-Xa_{cz}]} + K\sqrt{\frac{1-a_{sz}}{1-a_s}} \frac{a_s(1-a_s)}{\sqrt{(a_s-X)}[a_s(1-X(1-Xa_{sz}))-Xa_{sz}]}\right]},\tag{4}$$

where

$$T' = k_0 d n_{fz} = \frac{arctan\frac{1}{\sqrt{1-a_c}\sqrt{1-a_{cz}}}\sqrt{\frac{a_c-X}{X}} + arctan\frac{1}{\sqrt{1-a_s}\sqrt{1-a_{sz}}}\sqrt{\frac{a_s-X}{X}} + m\pi}{\sqrt{X}}.\tag{5}$$

For TM modes,

$$a_s = 1 - \frac{n_s^2}{n_f^2}; \ a_c = 1 - \frac{n_c^2}{n_f^2}; \ X = 1 - \frac{N^2}{n_f^2}; \ a_{sz} = 1 - \frac{n_{sz}^2}{n_{fz}^2}; \ a_{cz} = 1 - \frac{n_c^2}{n_{fz}^2}; \ K = \frac{n_{fz}}{n_f},$$

N is the effective refractive index, m is the mode order, d is the core thickness and k_0 is the free-space wavenumber.
The sensitivity can be expressed as a function of evanescent field intensity [13]:

$$S = \Gamma_s \left[\sqrt{\frac{1-a_c}{1-X}} + 2P\left(\sqrt{\frac{1-X}{1-a_c}} - \sqrt{\frac{1-a_c}{1-X}}\right)\right],\tag{6}$$

where, $P = 0$ for TE polarization. However, $P = 1$ for TM polarization.
The intensity of evanescent field can be represented by a confinement factor Γ_s, which is the ratio of an electric field intensity in the sensitive region or layer to the entire mode distribution of the guiding mode [14], defined as:

$$\Gamma_s = \frac{\iint_s |E(x,y)|^2 dx dy}{\iint_\infty |E(x,y)|^2 dx dy}.\tag{7}$$

Fields Distribution in Each Region for TE Modes

Guided TE modes exhibit exponentially decreasing behavior in the cover and substrate, and a sinusoidal behavior in the film region. Afterwards, by using boundary conditions, components of the EM field E_y, H_x and H_z in each region as a function of the amplitude can be extracted as [15]:

$$E_y = A \begin{cases} e^{-\gamma_c x} & x \geq 0 \\ \left(cos\gamma_f x - \frac{\gamma_c}{\gamma_f} sin\gamma_f x \right) & -d < x < 0 \\ \left(cos\gamma_f d + \frac{\gamma_c}{\gamma_f} sin\gamma_f d \right) e^{\gamma_s(x+d)} & x \leq -d \end{cases}, \tag{8}$$

$$H_x = \frac{\beta A}{\omega\mu_0} \begin{cases} e^{-\gamma_c x} & x \geq 0 \\ \left(cos\gamma_f x - \frac{\gamma_c}{\gamma_f} sin\gamma_f x \right) & -d < x < 0 \\ \left(cos\gamma_f d + \frac{\gamma_c}{\gamma_f} sin\gamma_f d \right) e^{\gamma_s(x+d)} & x \leq -d \end{cases}, \tag{9}$$

$$H_z = \frac{jA}{\omega\mu_0} \begin{cases} -\gamma_c e^{-\gamma_c x} & x \geq 0 \\ -\gamma_f \left(sin\gamma_f x + \frac{\gamma_c}{\gamma_f} cos\gamma_f x \right) & -d < x < 0 \\ \gamma_s \left(cos\gamma_f d + \frac{\gamma_c}{\gamma_f} sin\gamma_f d \right) e^{\gamma_s(x+d)} & x \leq -d \end{cases}, \tag{10}$$

where

$$\gamma_f = \sqrt{k_0^2 \varepsilon_f - \beta^2}.$$

$$\gamma_c = \sqrt{\beta^2 - k_0^2 \varepsilon_c}.$$

$$\gamma_s = \sqrt{\beta^2 - k_0^2 \varepsilon_s}.$$

Fields Distribution in Each Region for TM Modes

Similarly, different components of the EM field for TM modes can be expressed as:

$$H_y = A \begin{cases} e^{-\gamma_c' x} & x \geq 0 \\ cos\gamma_f' x - \frac{n_f^2}{n_c^2} \frac{\gamma_c'}{\gamma_f'} sin\gamma_f' x & -d < x < 0 \\ \left(cos\gamma_f' d + \frac{n_f^2}{n_c^2} \frac{\gamma_c'}{\gamma_f'} sin\gamma_f' d \right) e^{\gamma_s'(x+d)} & x \leq -d \end{cases}, \tag{11}$$

$$E_x = \frac{\beta A}{\omega\varepsilon_0 \varepsilon_i} \begin{cases} e^{-\gamma_c' x} & x \geq 0 \\ cos\gamma_f' x - \frac{n_f^2}{n_c^2} \frac{\gamma_c'}{\gamma_f'} sin\gamma_f' x & -d < x < 0 \\ \left(cos\gamma_f' d + \frac{n_f^2}{n_c^2} \frac{\gamma_c'}{\gamma_f'} sin\gamma_f' d \right) e^{\gamma_s'(x+d)} & x \leq -d \end{cases}, \tag{12}$$

$$E_z = \frac{-jA}{\omega\varepsilon_0 \varepsilon_{iz}} \begin{cases} -\gamma_c e^{-\gamma_c' x} & x \geq 0 \\ -\gamma_f' \left(sin\gamma_f' x + \frac{n_f^2}{n_c^2} \frac{\gamma_c'}{\gamma_f'} cos\gamma_f' x \right) & -d < x < 0 \\ \gamma_s' \left(cos\gamma_f' d + \frac{n_f^2}{n_c^2} \frac{\gamma_c'}{\gamma_f'} sin\gamma_f' d \right) e^{\gamma_s'(x+d)} & x \leq -d \end{cases}. \tag{13}$$

The dielectric constant ε_i differs from region to region, $i=c, f, s$ (cover, film, substrate).
where

$$\gamma_f' = \sqrt{k_0^2 \varepsilon_{fz} - \beta^2 \frac{\varepsilon_{fz}}{\varepsilon_f}},$$

$$\gamma_c' = \sqrt{\beta^2 \frac{\varepsilon_{cz}}{\varepsilon_c} - k_0^2 \varepsilon_{cz}},$$

$$\gamma_s' = \sqrt{\beta^2 \frac{\varepsilon_{sz}}{\varepsilon_s} - k_0^2 \varepsilon_{sz}}.$$

Influence of Waveguide and Source Parameters on the Sensor Sensitivity and Evanescent Fields

As, the sensitivity expressions and evanescent field components can be expressed as functions of waveguide and the light source parameters. We have developed a program in Matlab tool to observe the influence of physical, geometrical and the source parameters on the sensitivities of TE and TM modes as well as their influence on the evanescent fields in

the cover of a waveguide. For TE mode, H_z and H_x components are observed to be very small as compared to the E_y. However, for TM mode, the dominant components are E_x and E_z, while, H_y is unimportant. For the above said reason, small components are not represented in the figures. Basically, the slab waveguide consists of a core of $LiNbO_3$ on a glass substrate; the wavelength of the source was taken as 650 nm.

Effect of the Source's Parameters

Effect of the Field Amplitude. Equation (6) describes that the sensor becomes more sensitive as the intensity of evanescent field increases, where the intensities of the electric and magnetic evanescent fields are function of their amplitudes.

Fig. 2 illustrates the sensitivity as a function of the frequency for TE_0 and TM_0 modes for different fraction of modal power located in the cover. The observations revealed that, the sensitivity increases with the increase fraction of modal power located in the cover. Though, for TE_0, the sensitivity observed to be maximum for lower frequencies however, decreases for higher frequencies. Whereas, for TM_0, the sensitivity is minimal at lower frequencies while improves at higher frequencies.
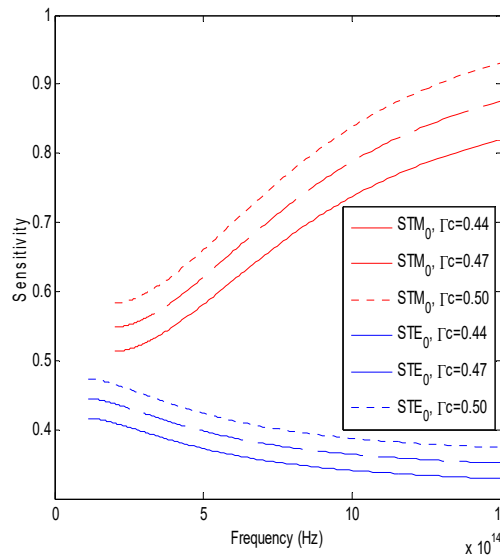

Figure 2. Sensitivity as a function of the frequency for TE_0 and TM_0 modes for different fraction of modal power located in the cover layer, (n_s=1.72, n_c=1.628, d=100 nm, $LiNbO_3$ as guiding film)

The improved sensitivities at higher modal power located in the cover resulted from enhanced amplitudes of evanescent field in the region, as illustrated in Fig. 3 and 4. It has also been observed that, amplitudes of evanescent field components of TM modes are more important than those of TE modes, hence, the sensitivity of TM modes are always greater than that of TE modes.
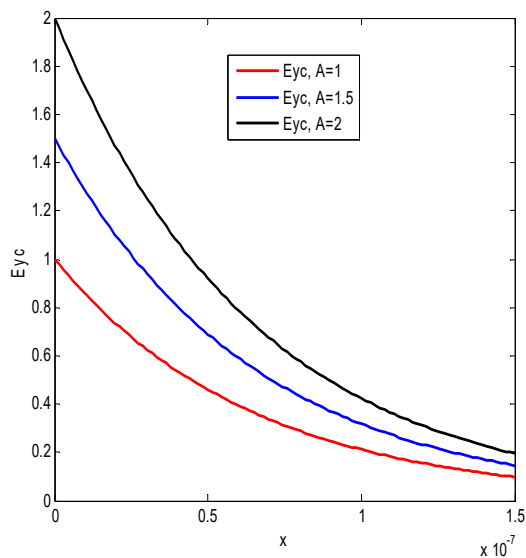

Figure 3. Evanescent field component E_{yc} in the cover versus x of TE_0 mode for different field amplitudes, (n_s=1.72, n_c=1.628, d=100 nm, $LiNbO_3$ as guiding film)
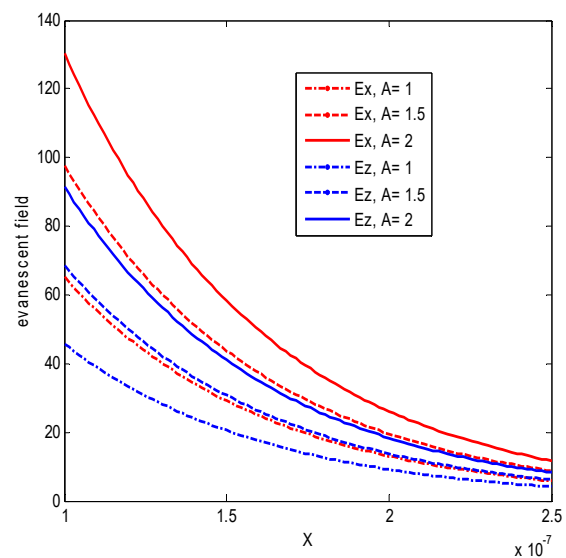
Figure 4. Evanescent field components (E_x, E_z) in the cover versus x of TM_0 mode for different amplitudes of field, (n_s=1.72, n_c=1.628, d=100 nm, $LiNbO_3$ as guiding film)

Effect of the Source's Wavelength. Sensitivities as a function of the core thickness for TE$_0$ and TM$_0$ modes, are presented in Fig. 5 observed at different source's wavelengths. The curves show that, sensitivity of the planar waveguide-based sensor increases by increasing the wavelength of source, however, the curves are shifted towards higher core thicknesses. This implies that, at higher wavelengths, maximum sensitivities can be obtained for higher core thicknesses and vice versa.
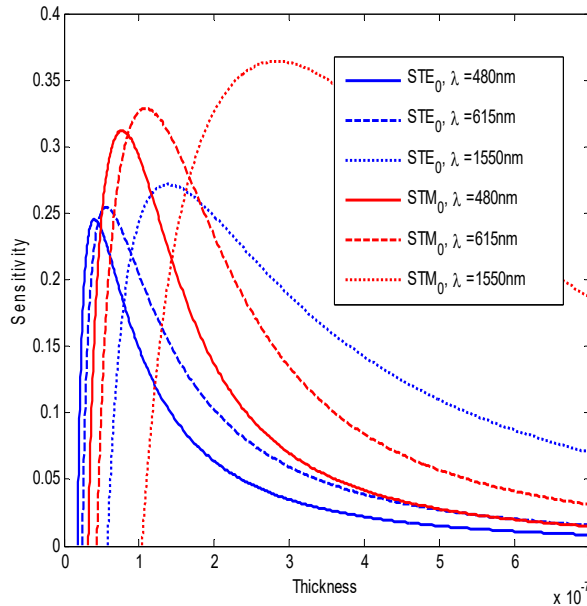

Figure 5 – Sensitivity as a function of the core thickness for TE$_0$ and TM$_0$ modes for different wavelength source, (n$_s$=1.72, n$_c$=1.628, d=100 nm, LiNbO$_3$ as guiding film)

The increase of the sensitivity for higher source's wavelengths can be justified by an increase in the intensities of evanescent field, as illustrated in Fig. 6 and 7.
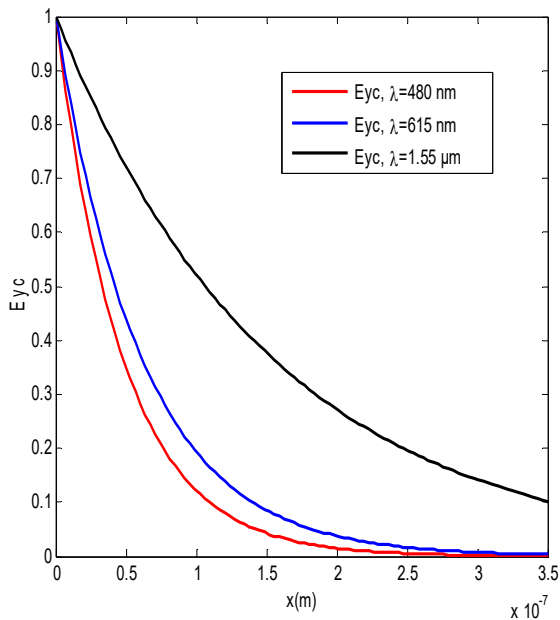

Figure 6. – Evanescent field components E$_{yc}$ in the cover versus x of TE$_0$ mode for different source's wavelengths, (n$_s$=1.72, n$_c$=1.628, d=100 nm, LiNbO$_3$ as guiding film)
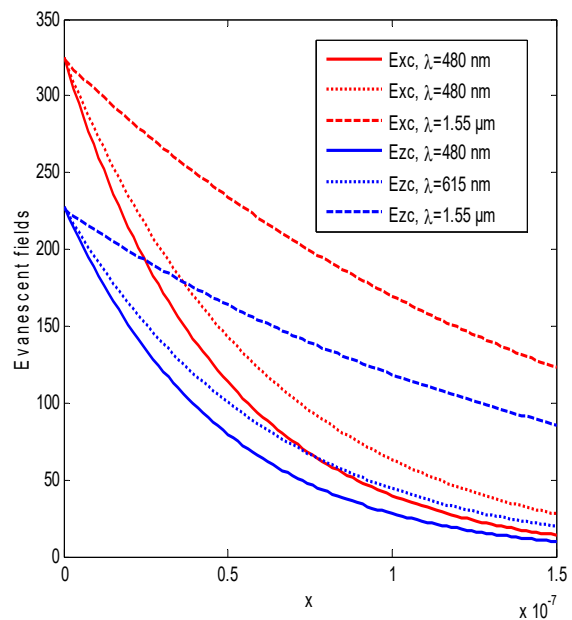

Figure 7. Evanescent field components (E$_x$, E$_z$) in the cover versus x of TM$_0$ mode for different source's wavelengths, (n$_s$=1.72, n$_c$=1.628, d=100 nm, LiNbO$_3$ as guiding film)

Effect of the Geometrical Parameter

Fig. 8, represents the sensitivity as a function of the frequency for TE$_0$ and TM$_0$ modes at different core thickness. The observations revealed that, by increasing the core thickness, sensitivity of the sensor decreases and curves shifted towards the lower frequencies. The reduced sensitivity is resulted from the decrease in sensing area limited by the evanescent fields, normal to the waveguide at z = 0 and the super surface of the waveguide (x = 0).
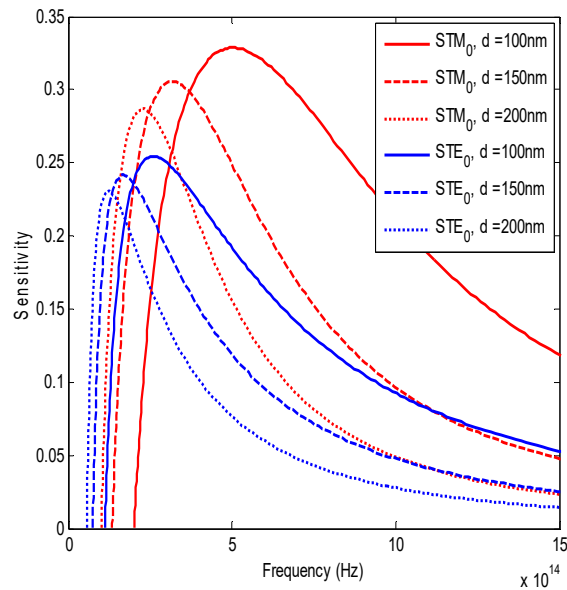
Figure 8. Sensitivity as a function of the frequency for TE_0 and TM_0 modes for different core thicknesses,
(n_s=1.72, n_c=1.628, $LiNbO_3$ as guiding film).

In fact, at greater core thickness, maximum part of an optical signal enters into the core of waveguide as energy and ultimately reduces the evanescent field intensities, as illustrated in Fig. 9 and 10.
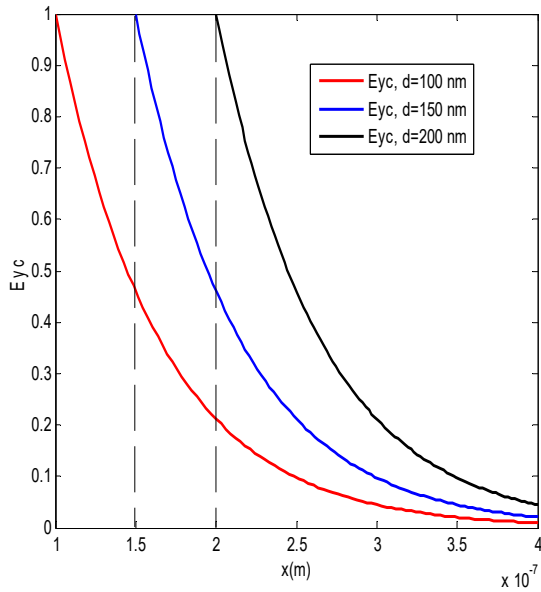

Figure 9. Evanescent field component E_{yc} in the cover versus x of TE_0 mode for different core thicknesses, (n_c=1.628, n_s =1.72, $LiNbO_3$ as guiding film)
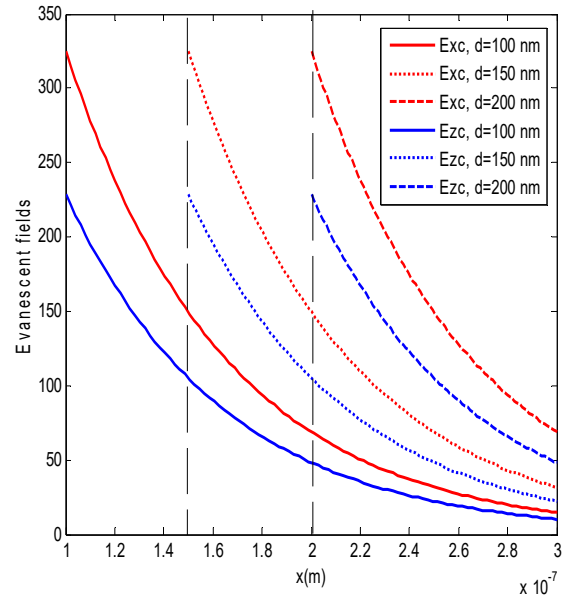
Figure 10. Evanescent field components in the cover versus x of TM_0 mode for different core thicknesses, (n_c=1.628, n_s =1.72, $LiNbO_3$ as guiding film)

Effect of the Physical Parameters

Physical parameters studied are the refractive indices of cover, substrate and the core of waveguide. Expressions (2) and (4) demonstrated the influence of physical parameters of waveguide on the sensitivity of the sensor. However, their influence on the evanescent fields are expressed by the electromagnetic field components in the cover.

Effect of the Cover Refractive Index. Fig. 11 illustrated the sensitivities as a function of the frequency of TE_0 and TM_0 modes when the refractive index of cover was taken as 1.48 and 1.70. For TE_0, the observed maximal sensitivities are 0.15 and 0.37, corresponding to the frequencies 3×10^{14} Hz and 1.25×10^{14} Hz, respectively. However, for TM_0, the observed maximal sensitivities are 0.23 and 0.47, corresponding to the frequencies 6.25×10^{14} Hz and 3.25×10^{14} Hz, respectively.
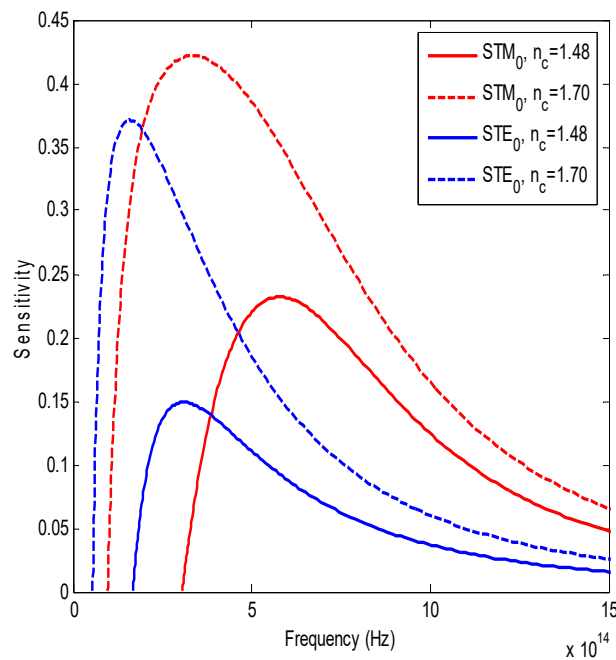
Figure 11. Sensitivity as a function of the frequency for TE_0 and TM_0 modes for different refractive index of the cover material n_c, (n_s=1.72, d=100 nm, $LiNbO_3$ as guiding film)

The curves show that, sensitivity of slab waveguide-based sensor increases by increasing the cover refractive index for both TE and TM modes. In addition to that, the position of maximal sensitivities exhibit shift toward lower frequencies. As the refractive index of cover must be always lesser than that for the substrate, one can conclude that, for both TE and TM modes, the sensitivity of a sensor increases by making the cover refractive index as close as possible to that for the substrate.

Nevertheless, for different cover refractive indices, small changes in the evanescent field components are evident, near to the cut-off frequencies, Fig. 12 and 13. These changes are caused by the variation in effective refractive indices of TE_0 and TM_0 modes induced by fluctuations in core refractive index, Fig. 14. These changes in evanescent field components in the cover, close to cut-off frequencies, have minimal influence on sensitivity of the slab waveguide-based sensor.
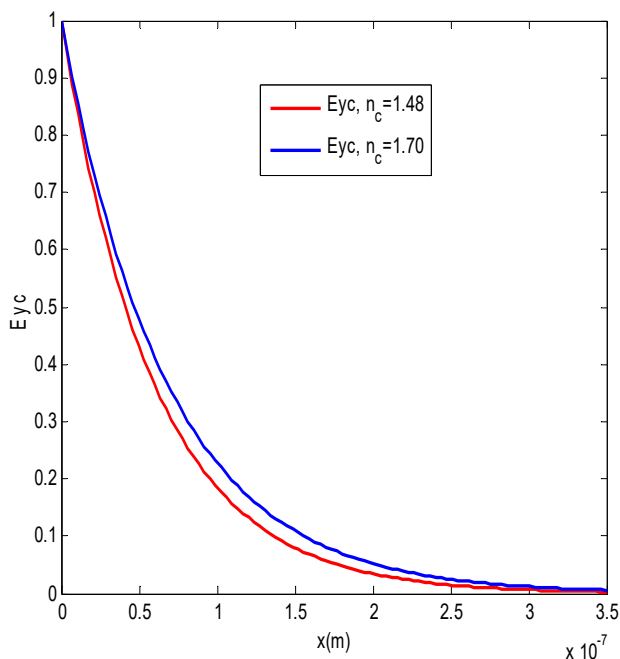

Figure 12. Evanescent field components E_{yc} in the cover versus x of TE_0 mode for different cover refractive indices, (n_s=1.72, d=100 nm, $LiNbO_3$ as guiding film)
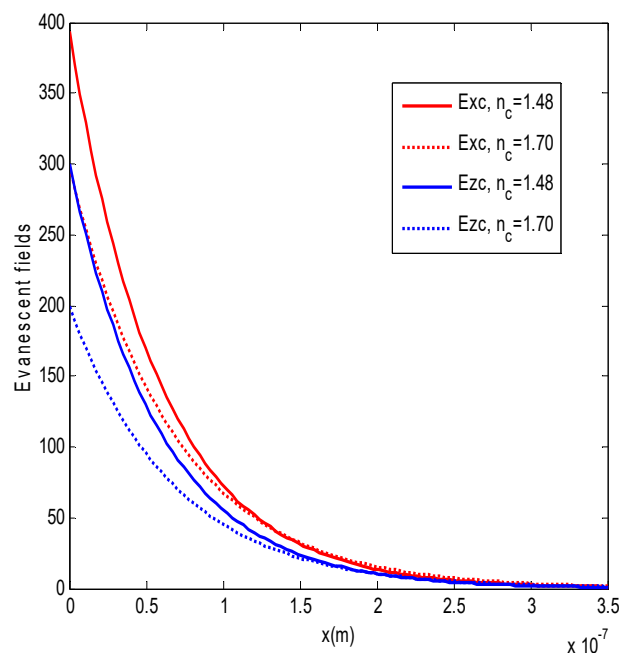
Figure 13. Evanescent field components (E_{xc}, E_{zc}) in the cover versus x of TM_0 mode for different cover refractive indices, (n_c=1.48, d=100 nm, $LiNbO_3$ as guiding film)
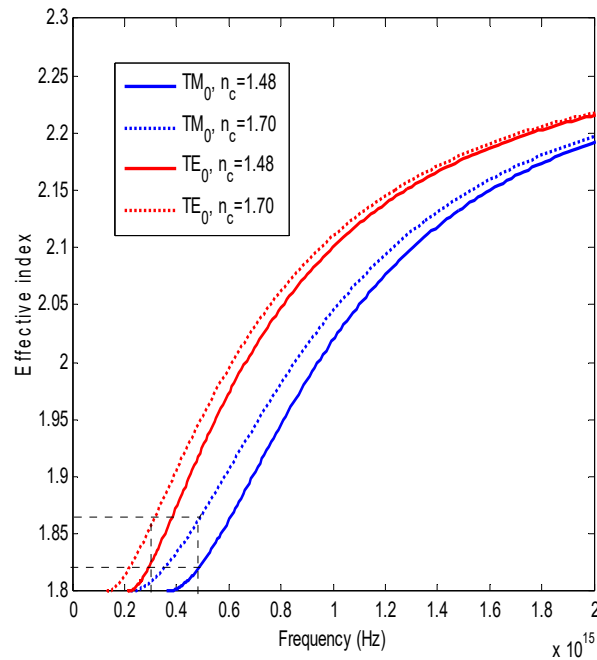
Figure 14. Effective index versus frequency of TE_0 and TM_0 modes in slab waveguide for different cover indices, (n_s=1.72, d=100 nm, $LiNbO_3$ as guiding film)

Effect of the Substrate Refractive Index. Fig. 15 represents the sensitivities of TE_0 and TM_0 modes as a function of the frequency, for various refractive index of substrate. Graphs depicted the maximal values of sensitivities and their corresponding frequencies. For TE_0, maximal sensitivities are observed to be 0.245 and 0.11, corresponding to 2×10^{14} Hz and $4 \ 10^{14}$ Hz frequency, respectively. For TM_0, maximal sensitivities are 0.34 and 0.175, corresponding to the frequencies as $5 \ 10^{14}$ Hz and $6 \ 10^{14}$ Hz, respectively. The sensitivity of sensor decreases as a function of substrate refractive index for both TE and TM modes. Furthermore, the position of maximal sensitivities exhibit shifts toward higher frequencies.
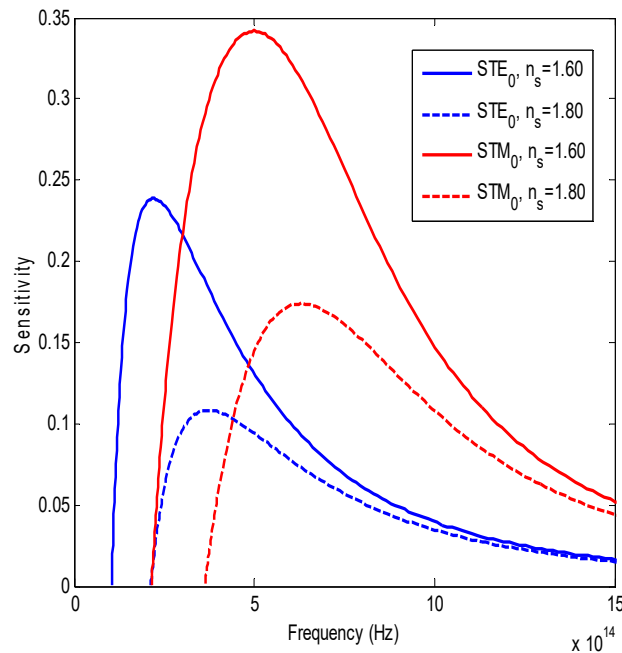

Figure 15. Sensitivity as a function of the effective index for TE_0 and TM_0 modes for different refractive index of the substrate n_s, (n_c=1.48, d=100 nm, $LiNbO_3$ as guiding film)

Evanescent field components of TE_0 and TM_0 modes, for different substrate refractive indices are depicted in Fig. 16 and 17 respectively.

Figure 16. Evanescent field components E_{yc} in the cover versus x of TE_0 mode for different substrate refractive indices, (n_c=1.48, d=100 nm, $LiNbO_3$ as guiding film)

Figure 17. Evanescent field components (E_x, E_z) in the cover versus x of TM_0 mode for different substrate refractive indices, (n_c=1.48, d=100 nm, $LiNbO_3$ as guiding film).

Curves show a small change in the evanescent field components caused by of the variation in refractive index of substrate; and, these small changes occur near the cut-off frequencies of each mode. Far from these frequencies, there has been no changes in evanescent field components. However, these changes are caused by small variation in effective refractive indices of substrate, Fig. 18. One can conclude that, change in evanescent field have negligible influence on the sensitivity of a slab waveguide sensor Fig. 15.
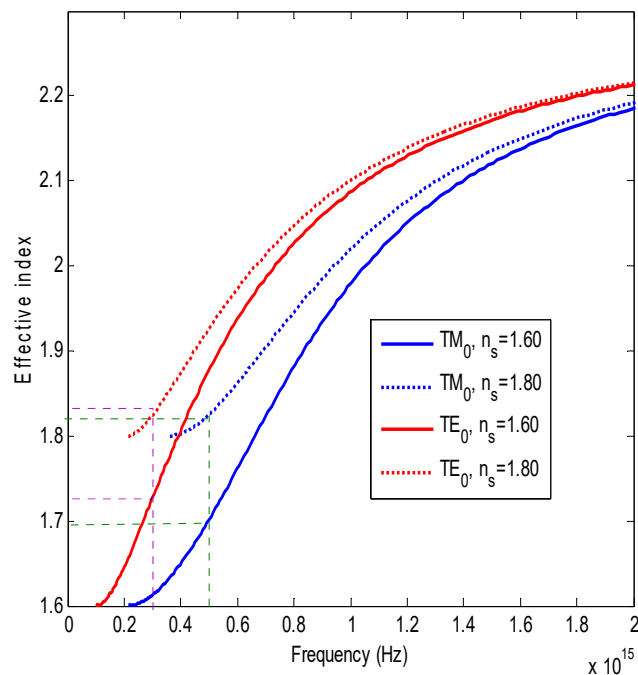
Figure 18. Effective index versus frequency of TE_0 and TM_0 modes in slab waveguide for different substrate refractive indices, (n_c=1.48, d=100 nm, $LiNbO_3$ as guiding film)

Effect of the Core Refractive Index. The sensitivities of TE_0 and TM_0 modes as a function of the frequency, for different core refractive index are illustrated in Fig. 19.
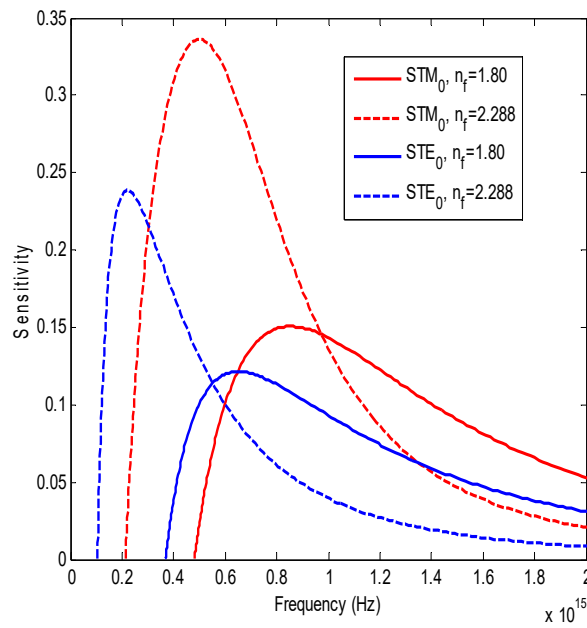
Fig. 19. Sensitivity as a function of the effective index for TE$_0$ and TM$_0$ modes for different refractive index of the core n$_f$, (n$_c$=1.48, n$_s$=1.60, d=100 nm,)

For TE$_0$, maximal sensitivities are observed to be 0.125 and 0.24 corresponding to 6 x 10^{14} Hz and 2 x 10^{14} Hz, respectively. However, for TM$_0$, maximal sensitivities are 0.15 and 0.34 corresponding to 8 x 10^{14} Hz and 5 x 10^{14} Hz, respectively. The observations revealed that, sensitivity of the planar waveguide-based sensor increases as a function of core refractive index for both TE and TM modes. In addition to that, the position of the maximal sensitivities exhibit shifts toward lower values of frequency.

On the other hand, evanescent field components as illustrated in Fig. 20 and 21 for different core refractive indices, exhibit moderate changes caused by variation in core refractive index; in fact, these changes occur far from the cut-off frequencies of each mode. These changes are caused by the variation in effective refractive indices of TE$_0$ and TM$_0$ modes induced at different core refractive index, Fig. 22. These changes in evanescent field, far from the cut-off frequencies, have negligible influence on the sensitivity of a slab waveguide sensor, since the sensitivity peaks appeared near the cut-off frequencies.
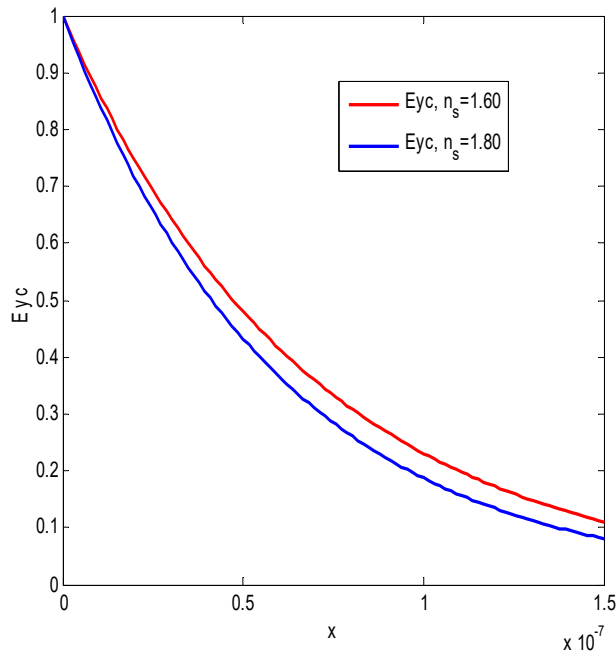

Figure 20. Evanescent field component E$_{yc}$ in the cover versus x of TE$_0$ mode for different core refractive indices, (n$_s$=1.60, n$_c$=1.48, d=100 nm)
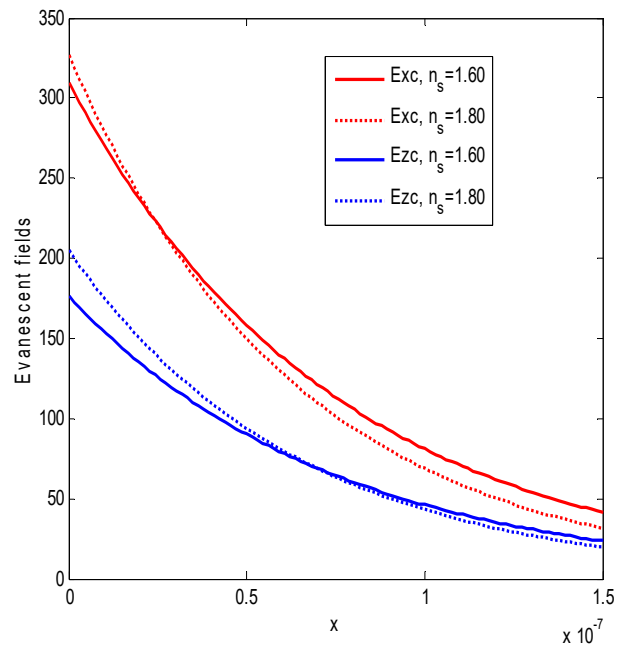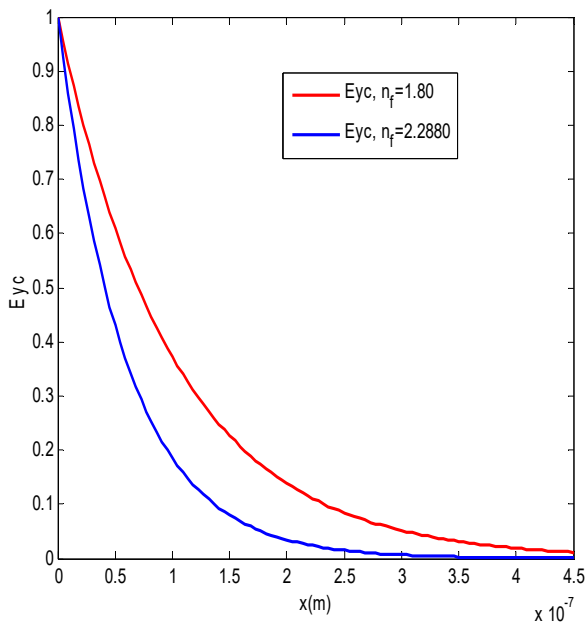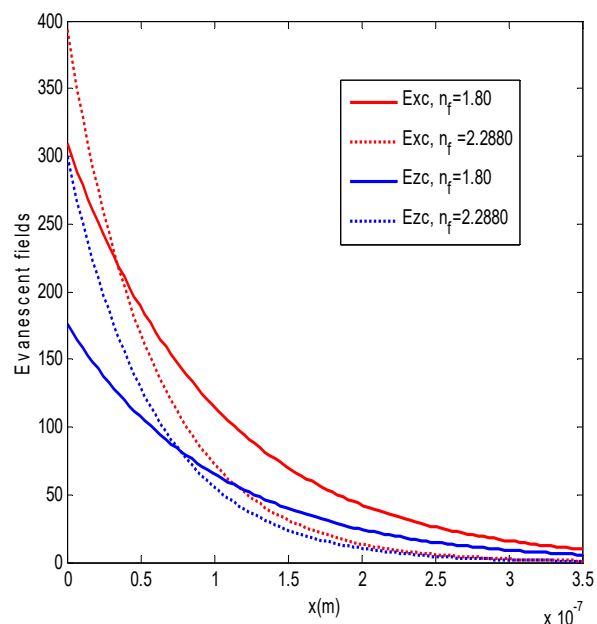

Figure 21. Evanescent field components (E$_{xc}$, E$_{zc}$) in the cover versus x of TM$_0$ mode for different core refractive indices, (n$_s$=1.60, n$_c$=1.48, d=100 nm)

CONCLUSIONS

In this work, sensitivity and evanescent field of a planar waveguide-based optical sensor prepared of birefringent materials have been investigated. The influence of source, geometrical and physical parameters of the planar waveguide on the sensitivity of sensor and evanescent field are studied. The observations in all cases revealed that, the maximal sensitivities of TM modes and their corresponding frequencies are greater than those for TE modes. Furthermore, improved sensitivity and evanescent field in the cover has been observed at in higher amplitude and wavelength of the light source. An increase in the core thickness however, reduces the sensitivity of sensor owing to the decrement of evanescent field in the cover. Although, any increment in refractive indices of cover and the core resulted in an improved sensor sensitivity. On the contrary, higher refractive index induces of substrate reduces the sensor sensitivity. The variation in physical parameters of the waveguide sensor have no or negligible influence on the evanescent fields.

ORCID IDs
Abdelhalim Bencheikh, https://orcid.org/0000-0001-7236-4821; Samah Boudour, https://orcid.org/0000-0002-4277-6945

REFERECNCES

[1] F.D. Leonardis, and V.M.N. Passaro, "Modeling and Performance of a Guided-Wave Optical Angular-Velocity Sensor Based on Raman Effect in SOI", Journal of Lightwave Technology, 25(9), 2352 (2007). https://opg.optica.org/jlt/abstract.cfm?URI=jlt-25-9-2352

[2] C.S. Huertas, O. Calvo-Lozano, A. Mitchell, and L.M. Lechuga, "Advanced Evanescent-Wave Optical Biosensors for the Detection of Nucleic Acids: An Analytic Perspective", Front. Chem. 7, 724 (2019). https://doi.org/10.3389/fchem.2019.00724

[3] T. Kovalevich, D. Belharet, L. Robert, M.S. Kim, H.P. Herzig, T. Grosjean, and M.P. Bernal, "Experimental evidence of Bloch surface waves on photonic crystals with thin-film $LiNbO_3$ as a top layer", Photonics Research, 5(6), 649 (2017). https://doi.org/10.1364/PRJ.5.000649

[4] P. Rabieia, and P. Gunter, "Optical and electro-optical properties of submicrometer lithium niobate slab waveguides prepared by crystal ion slicing and wafer bonding", Applied Physics Letters, 85, 4603 (2004). https://doi.org/10.1063/1.1819527

[5] O. Parriaux, and P. Dierauer, "Normalized expressions for the optical sensitivity of evanescent wave sensors: erratum", Optics Letters, 19(20), 1665 (1994). https://doi.org/10.1364/OL.19.001665

[6] A. Densmore, D.X. Xu, P. Waldron, S. Janz, P. Cheben, J. Lapointe, A. Delâge, B. Lamontagne, J.H. Schmid, and E. Post, "A silicon-on-insulator photonic wire based evanescent field sensor", IEEE Photonics Technology Letters, 18(23), 2520 (2006). https://doi.org/10.1109/LPT.2006.887374

[7] D. Kumar, and V. Singh, "Theoretical modeling of a nonlinear asymmetric metal-clad planar waveguide-based sensors", Optik 122(20), 1872 (2011). https://doi.org/10.1016/j.ijleo.2010.12.031

[8] A.A. Alkanoo, and S.A. Taya, "Theoretical investigation of five-layer waveguide structure including two left-handed material layers for refractometric applications", Journal of Magnetism and Magnetic Materials, 449, 395 (2018). https://doi.org/10.1016/j.jmmm.2017.10.086

[9] S.A. Taya, and S.A. Shaheen, "Binary photonic crystal for refractometric applications (TE case)", Indian Journal of Physics, 92(4), 519 (2018). https://doi.org/10.1007/s12648-017-1130-z

[10] S.A. Taya, "Ternary photonic crystal with left-handed material layer for refractometric application", Opto-Electronics Review, 26(3), 236 (2018). https://doi.org/10.1016/j.opelre.2018.05.002

[11] A. Cherouana, A. Bencheikh, and I. Bouchama, "Effect of the electric field induced birefringence on the slab waveguide evanescent-wave sensor sensitivity", Optical and Quantum Electronics, 51, 331 (2019). https://doi.org/10.1007/s11082-019-2018-2

[12] A.M. Jalaleddine, "Guided waves propagating in isotropic and uniaxial anisotropic slab waveguide", Dissertation, Ohio University U.S.A. 1982.

[13] G.J. Veldhuis, O. Parriaux, H.J.W.M. Hoekstra, and P.V. Lambeck, "Sensitivity enhancement in evanescent optical waveguide sensors", Journal of Lightwave Technology, 18(5), 677 (2000). https://doi.org/10.1109/50.842082

[14] V.M.N. Passaro, F. Dell'Olio, C. Ciminelli, M.N. Armenise, "Efficient chemical sensing by coupled slot SOI waveguides", Sensors, 9(02), 1012 (2009). https://doi.org/10.3390/s90201012

[15] G. Lifante, Integrated Photonics. Fundamentals, (John Wiley & Sons, England, 2003).

ДОСЛІДЖЕННЯ ЧУТЛИВОСТІ ТА ЕВАНЕСЦЕНТНОГО ПОЛЯ ОПТИЧНОГО СЕНСОРА НА ОСНОВІ ОДНООСНОГО АНІЗОТРОПНОГО ПЛОСКОГО ХВИЛЕВОДУ
Абдельбакі Черуана^a, Ідріс Бушама^{b,c}, Абдельхалім Бенчейх^d, Сама Будур^e, Мухаммад Саїд Ахтар^f

^a*Дослідницький відділ оптики та фотоніки – Університет Сетіфа 1, Центр розвитку передових технологій, Алжир*
^b*Факультет електроніки, технологічний факультет, Університет Мсіла, Мсіла, Алжир*
^c*Дослідницький відділ нових матеріалів (RUEM), Університет Ферхата Аббаса, Сетіф, Алжир*
^d*Факультет електромеханіки, Університет ВВА, Алжир*
^e*Науково-дослідний центр промислових технологій CRTI, Р.О. Бокс 64, Черага 16014, Алжир, Алжир*
^f*Факультет фізики, Університет освіти, Лахор, 54770, Пакистан*

Досліджено вплив геометричних і фізичних параметрів пластинчастого хвилеводу на чутливість оптичного датчика та його гасне поле. Хвилепровідною плівкою був $LiNbO_3$, і спостереження показали, що максимальна чутливість поперечних магнітних (ТМ) мод та їхні відповідні частоти вищі, ніж для поперечних електричних (ТЕ) мод. Крім того, оптимальні параметри джерела покращують максимальну чутливість і миттєве поле в обкладинці. Однак збільшення товщини серцевини знижує чутливість сенсора через зменшення спадаючого поля в покритті. Чутливість датчика спостерігали як функцію показників заломлення покриття, серцевини та підкладки. Збільшення показників заломлення покриття та серцевини безпосередньо впливає на чутливість, у той час як спостерігається зворотна залежність щодо збільшення показника заломлення підкладки. Варто зазначити, що будь-які зміни у фізичних параметрах хвилевідного датчика незначно впливають на гаснучі поля.

Ключові слова: планарний хвилевідний датчик; подвійне променезаломлення; параметри джерела; геометричні та фізичні параметри; чутливість сенсора; спадаюче поле

AN AB INITIO ANALYSIS OF STRUCTURAL, OPTICAL, ELECTRONIC, AND THERMAL PROPERTIES OF CUBIC SrSnO₃ USING WEIN2k†

Arya[a], Aditya Kumar[b], Varsha Yadav[c], Hari Pratap Bhaskar[d], Sushil Kumar[e], Satyam Kumar[e], Upendra Kumar[f],*

[a]*Department of Physics, National Institute of Science Education and Research, Jatni, Khurda-752050, Odisha, India*
[b]*Department of Physics, School of Science, IFTM University Moradabad-244102, U.P., India*
[c]*School of Applied Science, Shri Venkateshwar University, Gajraula (Amroha)-244221, U.P., India*
[d]*Department of Physics, Chaudhary Mahadeo Prasad Degree College Prayagraj -211002, U.P., India*
[e]*Department of Physics, Hansraj College, University of Delhi, New Delhi-07 India*
[f]*Advanced Functional Materials Laboratory, Department of Applied Sciences, IIIT Allahabad, Prayagraj-211015, U.P., India*
Corresponding author: upendrakumar@iiita.ac.in

This paper investigated the structural, optical, electronic and thermal characteristics of SrSnO₃ perovskites that were calculated using the density functional theory. Software called WEIN2K is used to perform the calculation. According to our calculations, the band gap energy of the SrSnO₃ is roughly 4.00 eV and it adopts a distorted cubic shape in the space group $Pm\bar{3}m$. The band structure and partial density of state reflects the major contribution of O 2p in the valence band while 5s orbital from Sn in the conduction band. The electron density plot significantly shows the contribution different clusters SrO₁₂ and SnO₆ that plays crucial role in electronic and optical properties. The creation of covalent bonds between the atoms of Sn and O as well as the ionic interaction between the atoms of Sr and O are both demonstrated by the electron density graphs and SCF calculation. The refractive index and extinction coefficient directly correlated with the real and imaginary part of complex dielectric function. Real part of dielectric function shows higher values at two major point of energy 3.54 eV and 9.78 eV associated with the absorption and optical activity of SrSnO₃. Negative part of imaginary dielectric function part suggests metallic behavior also supported by -grep lapw method. Thermoelectric and thermal conductivity properties suggest the power factor need to be improved for the device application.
Keywords: Density functional calculations; Electronic structure; Effective masses; Dielectric permittivity, Optical properties.
PACS: 71.15.Mb; 71.20.-b; 71.55.Ak; 72.20.Pa

The universal chemical formula for perovskite stannate oxides is ASnO₃ [1]. The alkaline earth stannate perovskites are one of the primary compounds in this group of minerals. Site A is occupied by alkaline earth metals including calcium (Ca), strontium (Sr), and barium (Ba), whose ionic radii vary from 100 pm to 135 pm [2]. In example, photovoltaic cells and light-emitting organic diodes have made extensive use of them to manufacture transparent electrodes for a variety of applications. Because of its outstanding dielectric and gas sensing qualities, ASnO₃ is very commonly utilised in electronics [3,4]. These perovskite compounds are used as anodes in Li-ion batteries and are made by destroying the crystal structure to produce sedentary metal oxides that are electrochemically active Sn metal. They are also promising materials for hydrogen synthesis and photocatalytic degradation [4,5].

The strontium stannate structure (SrSnO₃), which is the manuscript's main subject, is given special consideration. Sr²⁺ ions and 12 oxygen atoms occupy a dodecahedral site created by four [SnO₆] octahedrons to produce the crystalline structure of SrSnO₃ [6]. The Sn⁴⁺ cation is situated in the core of these octahedrons, which are made up of oxygen at their vertices. Due of the octahedral inclination that creates an orthorhombic structure (space group $Pbnm$) at ambient temperature, the unit cell of SrSnO₃ is a deformed cube [7]. Due to the extremely high mobility and concentration of carriers, SrSnO3 can also exist in other polymorphs ($Imma$, I4/mcm, and Pm3m) depending on the temperature increase [8].

In particular, SrSnO₃ is produced using a variety of synthesis techniques due to the scientific and technological interest in its applications. In order to clarify the effects of epitaxial tension on thin SrSnO₃ films, Gao et al. demonstrated that SrSnO₃ can be produced through a traditional solid-state reaction at high temperatures by combining an experimental investigation with a theoretical approach through DFT calculations using the LDA method [9]. Similar to this, a study conducted by Zhang et al. used DFT calculations implemented in the VASP simulation package, the revised Perdew-Burke-Ernzerhof function for solids (PBEsol) for structural relaxation, and Heyde-Scuseriae-Ernzerhof (HSE06) for the electronic structure analysis to explain the ferroelectricity induced by SrSnO₃ deformation and coupling, showing promising photovoltaic properties for use in solar cell devices [10].

Here, we carry out an ab-initio calculation for the strontium stannate structure (SrSnO₃) to show how the electrical properties are connected to various clusters, each of which has a distinct bonding environment based on the electron density distribution. Sr²⁺ ions are located in the corners of the cube in the crystal structure of SrSnO₃, while Sn ions are found with six oxygen atoms to form [SnO₆] octahedrons. The Sn⁴⁺ cation is situated in the core of these octahedrons, which are made up of oxygen at their vertices. SrSnO₃'s unit cell resembles a warped cube that produces an orthorhombic

structure (space group $Pm\overline{3}m$). Depending on the temperature range, additional $SrSnO_3$ structures exist as well (Imma, I4/mcm, and Pbnm). Furthermore, a structure-property relationship is established in this paper's detailed analysis of the structural characteristics in order to explain the electrical structure and the bandgap (E_{gap}) region.

METHODOLOGY

The full-potential linearized augmented plane waves (FPLAPW) method of the WIEN2k package is employed to examine the characteristics of SrSnO3. The exchange-correlation perspective employs the PBE sol generalised gradient approximation GGA. The modified Becke-Johnson potential proposed by Tran and Blaha (TB-mBJ) is employed for the self-consistent field (SCF) computations for the evolution of band gaps because the GGA underrates band gap values. In order to evaluate the outcomes of the predicted density functional theory (DFT). The FP-LAPW method is used to determine all energy-dependent characteristics. When spin-orbit interaction was removed, -6.0 Ry was chosen as the core cut-off energy. The cut-off vector of a plane wave is represented by K_{max}, and the value of RMT K_{max}=8 in the interstitial region. RMT is the minor muffin-tin radius. The magnitude of the most important vector in charge density is G_{max}= 16 Ry 1/2. Fourier expansion, and l_{max} = 10 for the angular momentum expansion. A fine k-mesh of 8×8×8 was chosen because thermoelectric and optical planning require a denser k-mesh for the convergence. When the total energy approaches 105 Ry, the iteration comes to an end. Boltzmann's transport theory, which establishes the parameters of thermoelectric transport as carried out by the BoltzTraP code, can be used to evaluate the thermoelectric transport tensors [11]. Using the interpolated band structure in WIEN2k, the BoltzTraP function produces the necessary derivatives to estimate the transport parameters. The direction of the k-vector determines the band index and relaxation duration, and this direction was kept constant in the BoltzTrap algorithm.

RESULTS

The parameters listed below can be used to discuss about the physicochemical properties of $SrSnO_3$ according to the results of the Wein2K DFT simulation software.

Energy-Volume optimization and crystal structure

The experimental results of SrSnO3 with a $Pm\overline{3}m$ space group, lattice parameters of a = b = c = 4.12 Å, and angles of $\alpha = \beta = \gamma = 90^o$. The Sr atom is located at coordinates (0,0,0), Sn at coordinates (0.5,0.5,0.5), and O at coordinates (0.5, 0.5, 0); (0, 0.5, 0.5); and (0.5, 0, 0.5). The energy-volume (E-V) optimised curve shown in Figure 1 indicates that the minimal amount of energy required by a construction is around 450 a.u^3. We determine more exact lattice parameters using the data below.

The cubic perovskite ($Pm\overline{3}m$) bulk structure of $SrSnO_3$ has been optimized, and its lattice parameters a = b = c = 4.08 Å, angles α = β = γ = 90º. The Sr atom is located at the coordinates (0,0,0), Sn atom (0.5,0.5,0.5) at the centre of cube, while the O atoms present at (0.5, 0.5, 0); (0, 0.5, 0.5) and (0.5, 0, 0.5), resulting in a model with 5 formula unit per structure (see Figure 2). Due to the well-known tendency of this function to overstate the strength of interatomic interactions, the value of lattice parameters obtained after optimization is smaller than that of the literature [12].
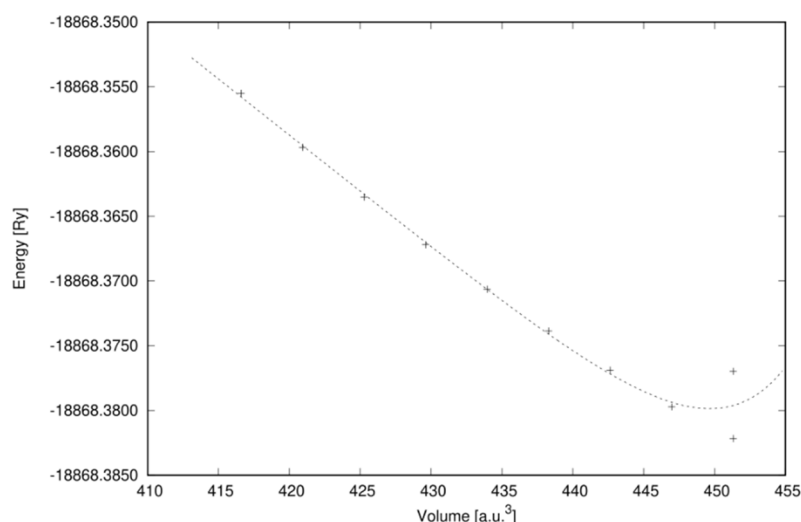
Figure 1. Energy vs. Volume curve using the volume optimization method for perovskite $SrSnO_3$
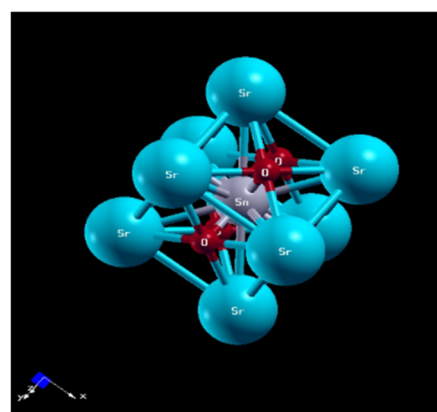
Figure 2. Crystal structure of perovskite $SrSnO_3$

Band structure and density of states (DOS)

The bonding between atoms and other desirable qualities are better understood by being familiar with the material's electrical characteristics. As illustrated in Figure 3, the band structure and density of state (DOS) projections on the

particles and atomic orbitals of strontium, tin, and oxygen were used to examine the electronic properties. The DOS figure demonstrates that the valence band and conduction band, which overlap in the plot, are primarily produced from Sn and Oxygen states. Maximum energy at which the valence band can form is 4.0 eV or less [13]. In contrast, the combination of Sr states with O upper orbitals creates the conduction band between -16.0 eV and -14.0 eV.
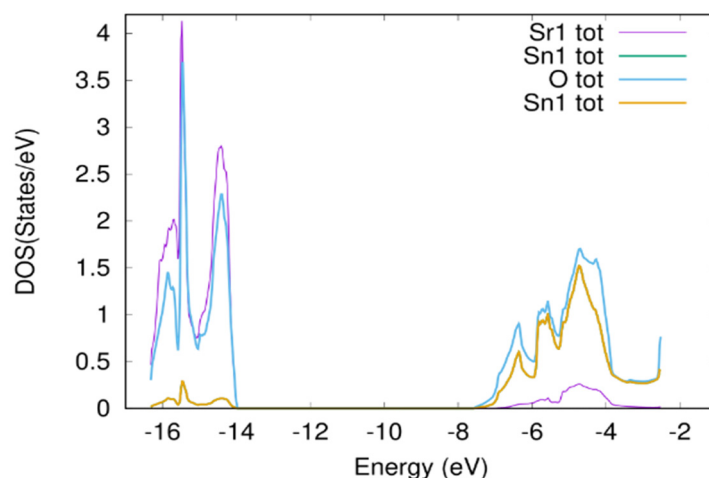
Figure 3. Total density of state (DOS) curve along with different individual atoms' DOS.

As illustrated in Figure 4, the integration of the reciprocal space for all calculations involving the SrSnO3 material used the k-points Γ (0,0,0) – X (½, 0,0) R (½, ½, ½) – M (½, ½, 0) – Γ (0,0,0). It can be observed in Figure 4 that the bandgap for SrSnO3 is an indirect transition between the k-points R-Γ with a value equal to 4.00 eV. The valence band (VB) zone is found between -17.91 and 0 eV, while the conduction band (CB) region is found between 4.18 and 29.84 eV, according to analysis of the DOS projection (Figure 4). Figure 4 shows the DOS projection for the atomic orbitals of Sr, Sn, and O atoms, showing that the three oxygen atoms have equivalent contributions and present the major contribution along with the VB through the 2s and 2p (x, y, z) orbitals combined with a minor extent of the Sr atomic orbitals 4p (x, y, z) on the other hand, the Sn atoms contribute more significantly to CB with the 5s, 5p (x, y, z), and 5d (xz, yz, and xy) orbitals [13-15].
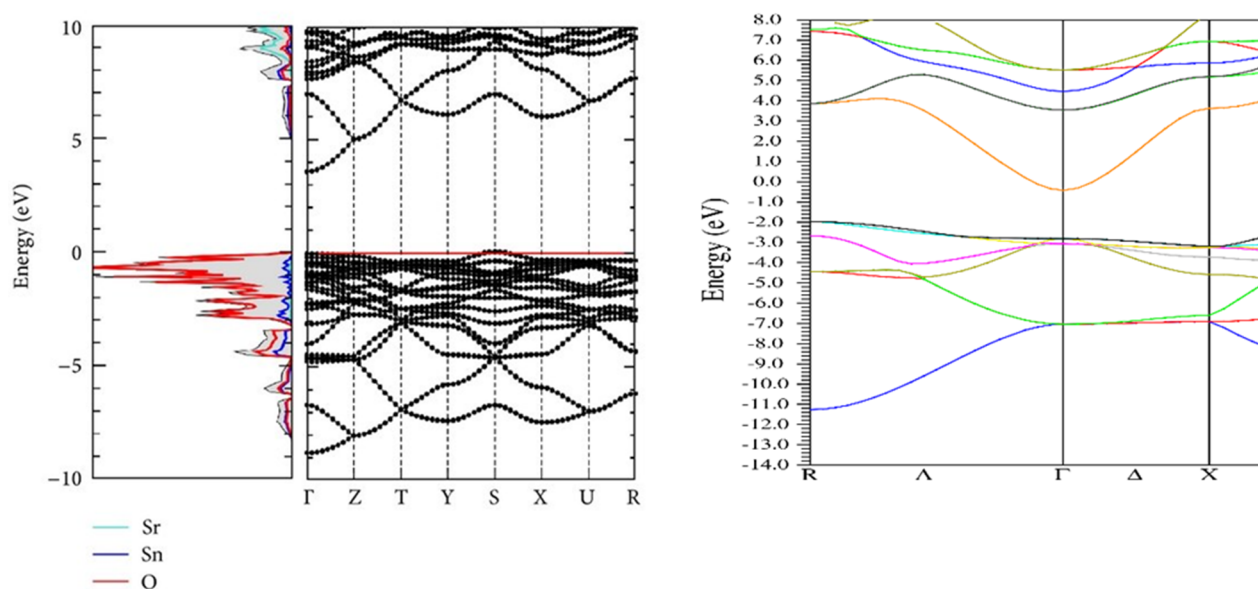
Figure 4. Band structure and partial density of state (PDOS) for cubic SrSnO₃ perovskite oxide.

Electron density around different atoms

On the basis of the charge density maps and 3D images, we further analyse the distribution of the electronic density along the crystalline structure. Isolines represent the same electrical density, which makes it easier to comprehend how chemical bonds are described. In order to identify and study the bonding interactions, the crystallographic plane is in the direction (1,1,0). The electronic density distribution of the O, Sn, and Sr atoms that make up the crystalline structure of SrSnO₃, which forms two different kinds of chemical bonds, is shown in Figure 5(a). Due to the O atom's lack of d orbitals, the pattern of electron density varies near different atoms [10,13]. While the O-Sr-O connection is demonstrated by an

ionic exchange, the O-Sn-O interaction is defined by a covalent interaction between these atoms. From the results of Figure 5(b), it feasible to observe that the isolines are shared by the nuclei on the yellow-hued Sn-O bond axes. The isolines are primarily focused on the nuclei of the Sr and O atoms, demonstrating the ionic nature of the Sr-O interactions.
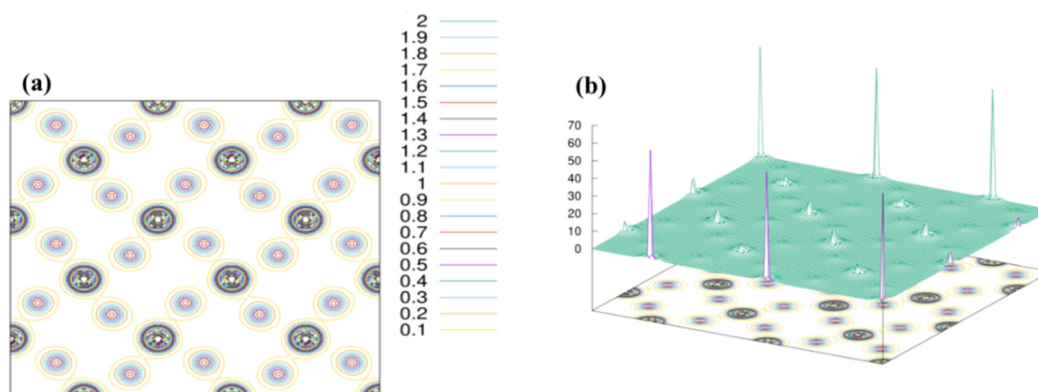
Figure 5. (a) Electron density 2D plot (b) Electron density 3D plot
(The yellow line shows the ionic interaction between oxygen and strontium).

Analysis of Total energy (ENE), Fermi energy (FER), and distribution of charge around spheres (CTO)

The overlap between these densities, which helps to produce chemical bonds in the various clusters $[SrO_{12}]$ and $[SnO_6]$, is another approach to examine the distribution of electrons around the nuclei. SCF cycle findings, as displayed in Figure 6, can be used to investigate the behaviour of the electronic density and crystalline structure.

The CTOXX (XX no. associated with each atom, O1-Sr, O2-Sn, O3-O) represents plots showing the total charge in a sphere at a time. In this framework, the positive slopes indicate that the overlap is adequate for forming the chemical bond, typically related to the covalent bonds. In contrast, the negative slope indicates that the orbitals' overlap occurs through a destructive interaction that disfavors the formation of the chemical bond and the resulting ionic bond. Based on the results related to charging overlap for Sr-O and Sn-O bonds of bulk $SrSnO_3$ and the charge density map, it was possible to describe the formation of covalent bonds between the Sn and O atoms with a value of 0.154 and ionic interaction between the Sr and O with a value of -0.006.
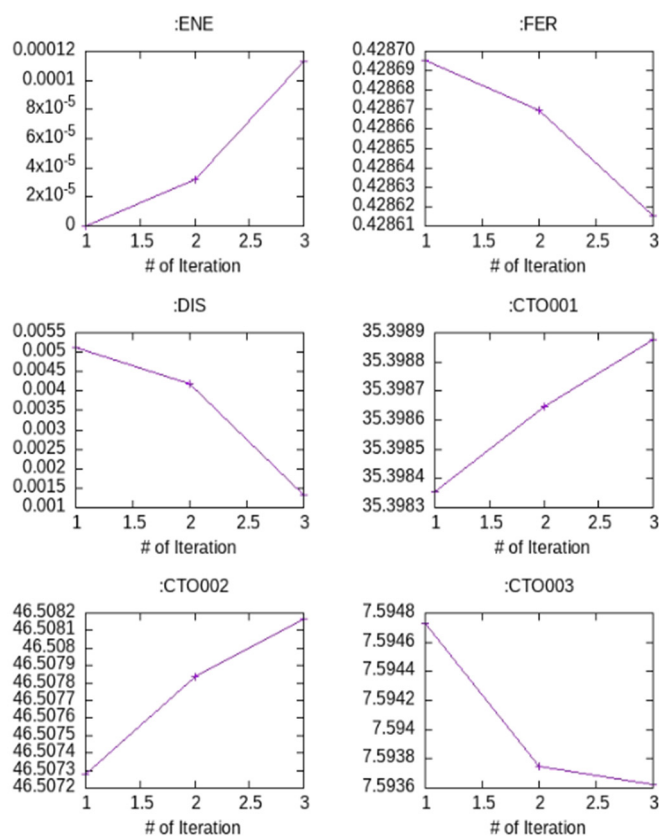
Figure 6. SCF analysis plotted vs. per number of Iteration. (ENE: total energy, FER: fermi energy, CTO01: Total charge in sphere Sr, CTO02: Total charge in sphere Sn, CTO03: Total charge in sphere O).

Optical properties

The optical structure of $SrSnO_3$ was measured precisely by applying the mBJ-potential technique on k-points with $4\times4\times4$ order as we can see that the band gap is between visible and near-ultraviolet region, due to which $SrSnO_3$ is a potential candidate for solar cells and some others optoelectronic devices. The dielectric function $\varepsilon(\omega)$ is a complex function: $\varepsilon(\omega) = \varepsilon_1(\omega) + i\varepsilon_2(\omega)$, where the real part $\varepsilon_1(\omega)$ characterizes the dispersion of the incident radiation by the medium and the imaginary one $\varepsilon_2(\omega)$ describes the absorbed energy by the medium. The plot for the real part of the dielectric function $\varepsilon_1(\omega)$ and $\varepsilon_2(\omega)$ were shown in Figures 7 (a) and (b), respectively. The value of $\varepsilon_1(0)$ was intense at 3.54 eV and 9.78 eV, respectively. After that, it decreases and finally attains zero. The values of $\varepsilon_1(\omega)$ are found negative between 24 to 28 eV for $SrSnO_3$, which is not shown here. The negative values of $\varepsilon_1(\omega)$ indicate that incident light is reflected from the material surface, which exhibits the metallic behavior of a compound [13,16]. Metallic

behavior can also be checked using the -grep lapw command associated with the software. The imaginary part of the dielectric function of optical materials is a crucial parameter in designing optoelectronic devices. The maximum absorption intensity of incident light in a particular region and the energy band gap can be measured using $\varepsilon_2(\omega)$ for the target material. The critical value of $\varepsilon_2(\omega)$ is between 4.15-6.0eV. The refractive index n(ω) and extinction coefficient k(ω) can also be calculated with the help of the following equation; $n_2 - k_2 = \varepsilon_1$ and $2n_1k_1 = \varepsilon_2$, where subscript 1 represents the real part and 2 represents the imaginary part of the refractive index and extinction coefficient, respectively. From the graphical analysis, the n(ω) and k(ω) will follow a similar trend as $\varepsilon_1(\omega)$, $\varepsilon_2(\omega)$. The relation between the static value of n (0) and $\varepsilon_1(0)$ is $2 = \varepsilon_1(0)$, which satisfies the result. Furthermore, n(ω) is a dimensionless quantity that describes energy propagation in a material. The value of n(ω) varies with a wavelength of light because of dispersion, due to which light splits into its constituent colors. The higher value of the refractive index is significant in the optical field, and the materials have in the range of one and two. In our case, the maximum value of n(ω) may be found between 7-9 eV for $SrSnO_3$ due to the higher value observed for ε_1 in this range. The middle peaks of the graph are analyzed, which disappear at higher energy, implying that at higher energy, the transparency of materials decreases, and high energy photons are absorbed due to band transition from valance to conduction.
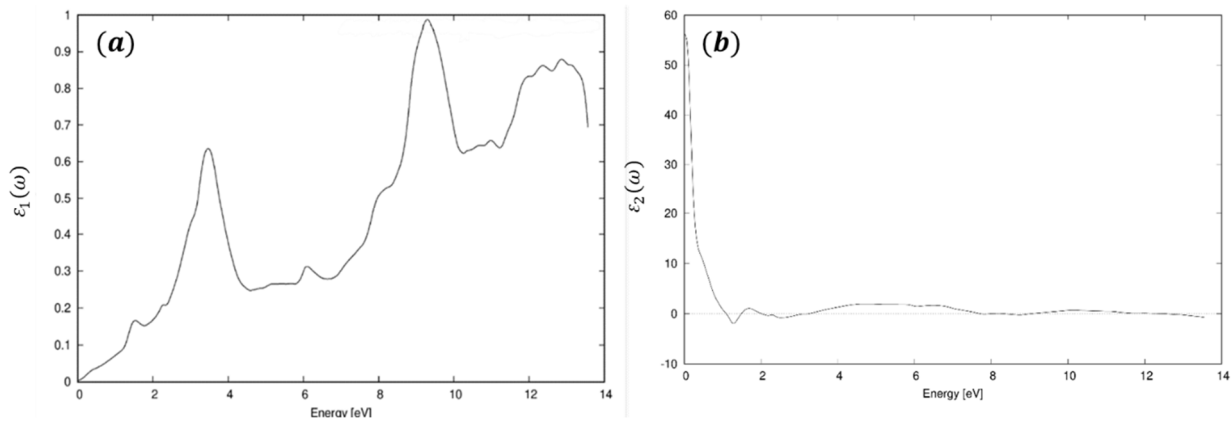
Figure 7. (a) $\varepsilon_1(\omega)$ (b) $\varepsilon_2(\omega)$ as a function of energy for cubic $SrSnO_3$

Thermoelectric properties

Thermoelectric materials have attracted huge consideration recently due to their applications ranging from clean energy to photon sensing devices. These materials are used in solid-state Peltier coolers and in generating waste heat. The variations in the essential transport properties like the Seebeck coefficient (S), electrical, thermal conductivity (k), electrical conductivity (σ), and power factor that could be represented as σS^2 as a function of temperature are valuable to explain the thermoelectric enactment of $SrSnO_3$. The power factor needs to be increased to improve the thermoelectric behavior that necessitates greater values of S and σ [16]. In contrast, the representation of electrical and thermal conductivity is essential, as shown in Figures 8(a) and (b).
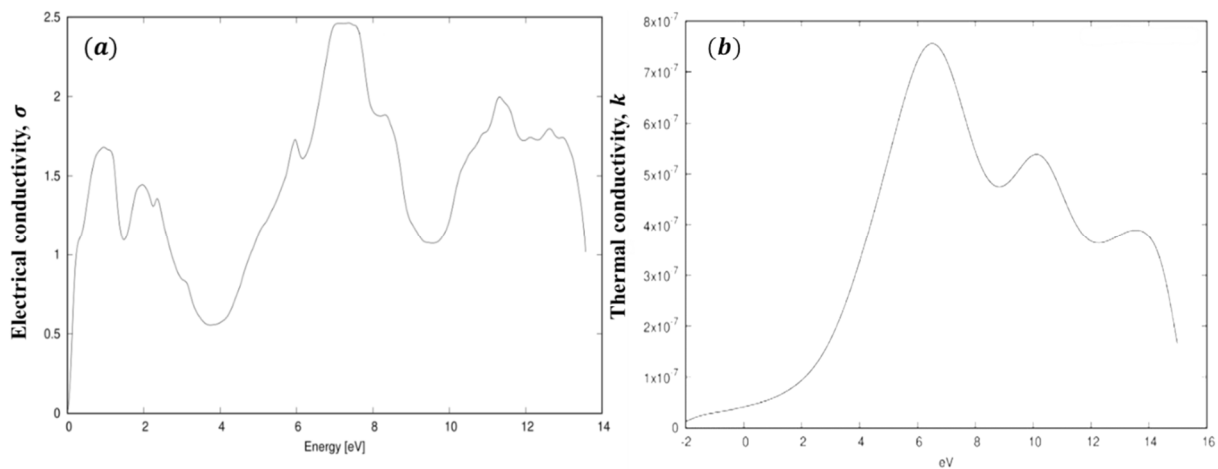
Figure 8. (a) Electrical conductivity, (b) Thermal conductivity, as a function of energy for cubic $SrSnO_3$.

The efficiency of the energy conversion devices for harvesting waste heat and converting it into usable electrical energy is overseen by a dimensionless parameter that is called a figure of merit (ZT), defined as $ZT = S^2\sigma T/k_e$, where S is the Seebeck coefficient (thermopower), σ is the electrical conductivity, T is the absolute temperature, and k_e is the thermal conductivity associated with an electron of the material, respectively [14]. The electrical conductivity increases strongly with

increasing charge carrier concentration. However, the thermal conductivity is noticeably anisotropic. The power factor can be calculated from the present values of electrical conductivity and thermal conductivity with the Seebeck coefficient reported in the literature for $SrSnO_3$; PF= $S^2\sigma$ and the figure of merit can be calculated by the formula ZT=$\sigma TS^2/k_e$ [12]. We find that $SrSnO_3$ can attain an efficiency of 0.07, expanding the calculated electrical and thermal conductivity values.

CONCLUSION

The analysis of SrSnO3 based on DFT theory provides us with a perspective to understand, interpret, and analyze the structural and electronic properties of the compound at the atomic level. The lattice parameter, bond structure, and other parameters on some level agree with the other work done on the same material. It was possible to observe that, in general, the valence band is occupied by electronic states originating from O and Sr atoms, while Sn atoms occupy the conduction band. The band gap was calculated as 4.00 eV, an indirect electron transfer process. Moreover, the SCF analysis confirms the covalent and ionic bond interaction. Therefore, the theoretical results using the Wein2K, B3LYP functional combined with the basis set for Sr, Sn, and O provided promising results in calculating structural and electronic properties. Data also provided insight that SrSnO3 can be an excellent alternative material for future transparent conductive devices.

ORCID IDs
Arya, https://orcid.org/0000-0002-8444-7461; **Aditya Kumar**, https://orcid.org/0000-0003-2823-774X
Varsha Yadav, https://orcid.org/0000-0003-1990-5910; **Hari Prasad Bhaskar**, https://orcid.org/0000-0002-1890-8936
Sushil Kumar, https://orcid.org/0000-0001-7415-9450; **Satyam Kumar**, https://orcid.org/0000-0001-7101-9559
Upendra Kumar, https://orcid.org/0000-0001-9200-0048

REFERENCES
[1] M. Glerup, K.S. Knight, and F.W. Poulsen, "High temperature structural phase transitions in $SrSnO_3$ perovskite", Mater. Res. Bull. **40**, 507 (2005). https://doi.org/10.1016/j.materresbull.2004.11.004

[2] R.D. Shannon, "Revised effective ionic radii and systematic studies of interatomic distances in halides and chalcogenides", Acta Crystallogr. Sect. A. **32**, 751 (1976). https://doi.org/10.1107/S0567739476001551

[3] A. Vegas, M. Vallet-Regí, J.M. González-Calbet, and M.A. Alario-Franco, "The ASnO3 (A=Ca,Sr) perovskites", Acta Crystallogr. Sect. B. **42**, 167 (1986). https://doi.org/10.1107/S0108768186098403

[4] Y. Liu, Y. Zhou, D. Jia, J. Zhao, B. Wang, Y. Cui, Q. Li, and B. Liu, "Composition dependent intrinsic defect structures in ASnO3 (A = Ca, Sr, Ba)", J. Mater. Sci. Technol. **42**, 212 (2020). https://doi.org/10.1016/j.jmst.2019.10.015

[5] Y.A. Zulueta, R. Mut, S. Kaya, J.A. Dawson, and M.T. Nguyen, "Strontium Stannate as an Alternative Anode Material for Li-Ion Batteries", J. Phys. Chem. C. **125**, 14947 (2021). https://doi.org/10.1021/acs.jpcc.1c02652

[6] A. Kumar, B. Khan, V. Yadav, A. Dixit, U. Kumar, and M.K. Singh, "Rietveld refinement, optical, dielectric and ac conductivity studies of Ba-doped $SrSnO_3$", J. Mater. Sci. Mater. Electron. **31**, 16838 (2020). https://doi.org/10.1007/s10854-020-04240-7

[7] E. Cortés-Adasme, R. Castillo, S. Conejeros, M. Vega, and J. Llanos, "Behavior of Eu ions in $SrSnO_3$: Optical properties, XPS experiments and DFT calculations", J. Alloys Compd. **771**, 162 (2019). https://doi.org/10.1016/j.jallcom.2018.08.239

[8] A.L. Goodwin, S.A.T. Redfern, M.T. Dove, D.A. Keen, and M.G. Tucker, "Ferroelectric nanoscale domains and the 905 K phase transition in $SrSnO_3$: A neutron total-scattering study", Phys. Rev. B, **76**, 174114 (2007). https://doi.org/10.1103/PhysRevB.76.174114

[9] Q. Gao, K. Li, L. Zhao, K. Zhang, H. Li, J. Zhang, and Q. Liu, "Wide-range band-gap tuning and high electrical conductivity in La-and Pb-doped $SrSnO_3$ epitaxial films", ACS Appl. Mater. Interfaces, **11**, 25605 (2019). https://doi.org/10.1021/acsami.9b07819

[10] M.M. de Moura Bezerra, M.C. Oliveira, W.D. Mesquita, A.B. da Silva Junior, E. Longo, and M.F. do Carmo Gurgel, "An Ab Initio Analysis of Structural and Electronic Properties of Cubic $SrSnO_3$", Orbital Electron. J. Chem. 227 (2021). http://dx.doi.org/10.17807/orbital.v13i3.1603

[11] A.A. Adewale, A. Chik, R.M. Zaki, F.C. Pa, Y.C. Keat, and N.H. Jamil, "Thermoelectric transport properties of $SrTiO_3$ doped with Pm", Solid State Phenom. Trans. Tech. Publ, **280**, 3 (2018). https://doi.org/10.4028/www.scientific.net/SSP.280.3

[12] L. Salik, A. Bouhemadou, K. Boudiaf, F.S. Saoud, S. Bin-Omran, R. Khenata, Y. Al-Douri, and A.H. Reshak, "Structural, elastic, electronic, magnetic, optical, and thermoelectric properties of the diamond-like quaternary semiconductor $CuMn_2InSe_4$", J. Supercond. Nov. Magn. **33**, 1091 (2020). https://doi.org/10.1007/s10948-019-05331-1

[13] E. Moreira, J.M. Henriques, D.L. Azevedo, E.W.S. Caetano, V.N. Freire, and E.L. Albuquerque, "Structural, optoelectronic, infrared and Raman spectra of orthorhombic $SrSnO_3$ from DFT calculations", J. Solid State Chem. **184**, 921 (2011). https://doi.org/10.1016/j.jssc.2011.02.009

[14] V.V. Bannikov, I.R. Shein, V.L. Kozhevnikov, and A.L. Ivanovskii, "Magnetism without magnetic ions in non-magnetic perovskites $SrTiO_3$, $SrZrO_3$ and $SrSnO_3$", J. Magn. Magn. Mater. **320**, 936 (2008). https://doi.org/10.1016/j.jmmm.2007.09.012

[15] S. Li-Wei, D. Yi-Feng, Y. Xian-Qing, and Q. Li-Xia, "Structural, electronic and elastic properties of cubic perovskites $SrSnO_3$ and $SrZrO_3$ under hydrostatic pressure effect", Chinese Phys. Lett. **27**, 96201 (2010). https://doi.org/10.1088/0256-307X/27/9/096201

[16] H. Shaili, E. Mehdi Salmani, M. Beraich, R. Essajai, W. Battal, M. Ouafi, A. Elhat, *et al*, "Enhanced properties of the chemically prepared Gd-doped $SrSnO_3$ thin films: experimental and DFT study", Opt. Mater. (Amst). **107**, 110136 (2020). https://doi.org/10.1016/j.optmat.2020.110136

AB INITIO АНАЛІЗ СТРУКТУРНИХ, ОПТИЧНИХ, ЕЛЕКТРОННИХ, ТА ТЕРМІЧНИХ ВЛАСТИВОСТЕЙ КУБІЧНОГО SrSnO₃ ЗА ДОПОМОГОЮ WEIN2k

Арья[a], Адіт'я Кумар[b], Варша Ядав[c], Харі Пратап Бхаскар[d], Сушіл Кумар[e], Сатьям Кумар[e], Упендра Кумар[f]
[a]Фізичний факультет, Національний інститут наукової освіти та досліджень, Джатні, Кхурда-752050, Одіша, Індія
[b]Фізичний факультет, Наукова школа, Університет IFTM, Морадабад-244102, U.P. Індія
[c]Школа прикладних наук, Університет Шрі Венкатешвар, Гаджраула (Амроха)-244221, UK, Індія
[d]Фізичний факультет, Чаудхарі Махадео Прасад коледж, Праяградж -211002, U.P. Індія
[e]Фізичний факультет коледжу Хансрадж Делійського університету, Нью-Делі-07, Індія
[f]Лабораторія передових функціональних матеріалів, Департамент прикладних наук,
ІІТ Аллахабад, Праяградж-211015, U.P. Індія

У цій статті досліджено структурні, оптичні, електронні та термічні характеристики перовскітів $SrSnO_3$, які були розраховані за допомогою теорії густини функціоналу. Для виконання обчислень використовується програмне забезпечення під назвою WEIN2K. Відповідно до наших розрахунків, енергія забороненої зони $SrSnO_3$ становить приблизно 4,00 еВ, і він приймає викривлену кубічну форму в просторовій групі $Pm\overline{3}m$. Зонна структура та часткова щільність станів відображають основний внесок O 2p у валентну зону, а 5s-орбіталь від Sn у зоні провідності. Графік електронної густини суттєво показує внесок різних кластерів SrO_{12} і SnO_6, який відіграє вирішальну роль в електронних і оптичних властивостях. Створення ковалентних зв'язків між атомами Sn і O, а також іонна взаємодія між атомами Sr і O демонструються графіками електронної густини та розрахунком SCF. Показник заломлення та коефіцієнт екстинкції прямо корелюють з дійсною та уявною частинами складної діелектричної функції. Реальна частина діелектричної функції показує вищі значення в двох основних точках енергії 3,54 еВ і 9,78 еВ, пов'язаних з поглинанням і оптичною активністю $SrSnO_3$. Від'ємна частина частини уявної діелектричної функції свідчить про поведінку металу, що також підтримується методом -grep lapw. Властивості термоелектричної та теплопровідності свідчать про необхідність покращення коефіцієнта потужності для застосування пристрою.

Ключові слова: розрахунки густини функціоналу; електронна структура; ефективні маси; діелектрична проникність, оптичні властивості.

UTILISING SPECTROSCOPY AND OPTICAL MICROSCOPY TO CHARACTERIZE TITANIUM DIOXIDE THIN FILMS[†]

Hmoud Al-Dmour*

Department of Physics, Faculty of Science, Mutah University, Mutah, 61710, Jordan
*Correspondence Author: hmoud79@mutah.edu.jo

This paper presents the surface electronic structure and morphological characteristics of the nano-crystalline titanium dioxide (nc TiO_2) films derived from the two different sol-gels. Using Scanning tunneling microscopy/spectroscopy (STM/S), it was found that the particles of nc-TiO_2 produced from batch A have a surface band gap of ~3.3 eV while the particles of nc-TiO_2 produced from batch B have a surface band gap of ~2.6 eV. On other hand, the small particles have aggregated together to form larger particles ranging from ~120 nm to 150 nm in size and distributed randomly over the surface of the batch A nc-TiO_2 films. For batch B nc-TiO_2films, the small particles have formed larger particles but with their size ranging from 200 nm to 225 nm. That is ascribed to differences between sol-gels used to prepare nc-TiO_2 films. As a result of that, the electric power of batch A nc-TiO_2/P3HT solar cells is enhanced by more than 8 times in comparison with batch B solar cells.
Keywords: *Nano-crystalline titanium dioxide; Particles/Pin holes; Surface band gap; Transmittance; STS measurements*
PACS: 84.60.Jt, s, 68.60.Bs, 81.07.Pr, 68.37.Ef, 68.37.Ps, 42.25.Bs, 61.72.y

INTRODUCTION

Titanium dioxide (TiO_2) is an important inorganic compound that is widely used. It was discovered in 1791 by William Gregor [1] and attracted the attention of many researchers due to its unique physical, chemical, and electronic properties [2,3]. It is a white pigment used in plastics, paints, rubbers and paper [4]. Additionally, TiO_2 is considered to be a non-toxic material and available naturally at low cost. It is composed of 59.94 % titanium and 40.06 % oxygen. In 1972, the photocatalytic characteristics of titanium oxide were discovered by Fujishima and Hond [5]. This led to the establishment of a new area in heterogeneous photocatalysts to overcome problems such as pollution [6]. Another important application of nc-TiO_2 was reported first time in 1990 when Grtäzel used it in the fabrication of dye sensitized solar cells with high efficiency [7]. Nano crystalline Titanium dioxide (nc-TiO_2) is a well-known electron acceptor and transparent layer for applications in solar cells. To optimize electronic and photocatalystic function. It is important to study the spectroscopy and optical microscopy of titanium dioxide layer, hence investigating of surface electronic structure and morphological characteristics and optical properties are necessary [3,8]. That is attributed to producing several nanometer and micrometer size titanium dioxide structures of various geometries obtained by various methods: spray pyrolysis, colloidal suspension and a sol-gel procedure [9,10]. The films prepared by all of these methods contain either nano-crystals or micro-crystals of TiO_2. The size of nano-crystals depends on the temperature of annealing and the content of the materials used to form the TiO_2. In this work, we report the electronic , morphological and optical properties of the nc-TiO_2 films using scanning tunneling microscopy (STM) and atomic force microscopy. This technique has been used to show that the age and components of the nc-TiO_2 films affect the electronic properties of the film.

EXPERIMENTAL

Porous nc-TiO_2 films were readily prepared by spreading a TiO_2sol-gel over the substrate surface and sintering at high temperature. Two batches of TiO_2sol-gel (Ti-Nanoxide T) were purchased from Solaronix SA. According to the supplier, these batches differed from each other only in terms of age which influenced on the first batch (labeled batch A) has higher water/ethanol concentration and lower solid residue than the second batch (labeled batch B) in order to distinguish the films. Prior to use, the TiO_2sol-gel was stirred using a clean glass rod for 1 minute. To define the area of substrate to be coated with TiO_2sol-gel, we used 3M Scotch Magic tape. It had a thickness of 50μm and is easily removed from the substrate without leaving traces of adhesive material. The amount of TiO_2 sol-gel initially used depends on the substrate area to be coated. Following the procedures in the literature [9], we used around 50 μL of TiO_2 sol-gel to coat 5 cm^2 area of substrate surface. The 50 μL of TiO_2 sol-gel was deposited on the edge of the substrate using a micropipette. A cleaned glass rod was used to spread the sol-gel over the substrate area defined by the tape. Then, the film was left in air for 10 minutes to dry until its milky colour disappeared.

Digital Instruments Nanoscope 3A multimode instrument was used to operate as a Scanning Tunnelling Microscope (STM) for Scanning Tunnelling Spectroscopy (STS) measurements. It was undertaken to determine the electronic properties of the nc-TiO_2surface. This technique has been used to show that the age of the nc-TiO_2film as well as the type of material attached to the nc-TiO_2surface affects the electronic properties of the film [11]. It is conducted by applying a voltage between the tip and the surface of the sample allowing electrons to tunnel from the tip to the surface of the

semiconductor (metal) and vice versa. This generates a small current across the gap which depends on the height between the tip and sample surface, bias voltage and the properties of sample surface (see Figure 1). In STS, we are concerned with measuring the onset of electron emission from the tip into the semiconductor LUMO level in negative bias and from the semiconductor HOMO level to the tip in positive bias.

The UV-visible absorption spectra of the various materials used in the construction of the solar cells were obtained using a Hitachi Model U-2000 Double BeamUltra-Violet/Visible (UV/VIS) spectrophotometer.
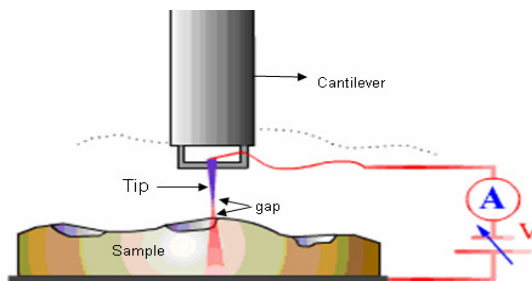
Figure 1. Schematic illustration of the scanning tunnelling spectroscopy (Image adopted from reference [12]

RESULTS AND DISCUSSION

In the present study, two nc-TiO$_2$ films were studied; one produced from batch A and one from batch B. Figure 2a gives the tunneling current as a function of voltage for the batch A film. At - 0.7 V, the current flowing is referred to as the anodic tunneling current while the current flowing at 2.6 eV referred to as the cathodic current. When the tunneling current is zero in the region that separates the cathodic and the anodic currents this corresponds to the band gap of the sample. Figure 2b shows the conduction spectrum (dI/dv) versus voltage (V) of the batch A nc-TiO$_2$ obtained by numerical differentiation of the I-V relation. This reveals an increase in conductance for positive voltage influenced by the valence band and negative voltage influenced by the conductive band of nc-TiO$_2$ film. Therefore, the surface band gap energy for the batch A nc-TiO$_2$ film is estimated to be ~3.3 eV based on conductance results and similar to report in the literature [13].

(a)   **(b)**
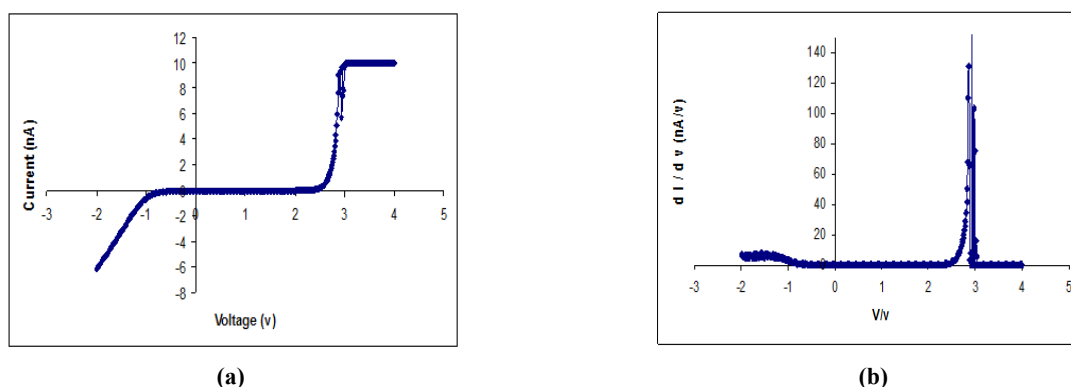
Figure 2. (a) STS I-V characteristics of batch A nc-TiO$_2$ film, (b)STS dI-dV characteristics of batch A nc-TiO$_2$ film

On other hand, Figures 3a and 3b show the corresponding tunneling current and conductance plots for nc-TiO$_2$ film produced from batch B. The onset voltage for anodic and cathodic tunneling currents were ~-0.8 V and 1.8 V respectively. For batch B nc-TiO$_2$, there is a reduction, therefore, in the surface band gap energy from ~3.3 eV to ~2.6 eV.

(a)   **(b)**

Figure 3. (a) STS I-V characteristics of batch B nc-TiO₂ film, (b)STS dI-dV characteristics of batch B nc-TiO₂ film

AFM images showed more detailed topographical information of the two samples, making it possible to observe the difference between them in term of pin holes, average diameter, and shape of nc-TiO$_2$particles. Figures 4a, 4b show the AFM images of nc-TiO$_2$ films produced from batch A and batch B sol gel. The two films consist of nanoparticles p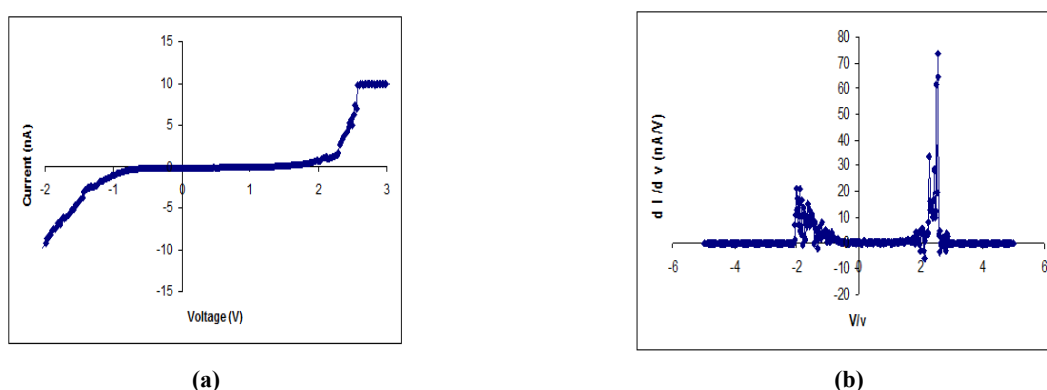artially interconnected with each other. However, there are differences between them. For batch A nc-TiO$_2$ films, the small particles have aggregated together to form larger particles ranging from ~120 nm to 150 nm in size and distributed randomly over the surface of the nc-TiO$_2$ film. For batch B nc-TiO$_2$films, the small particles have also formed larger particles but with their size ranging from 200 nm to 225 nm, the particles are distributed uniformly over the sample area.

(a)   (b)
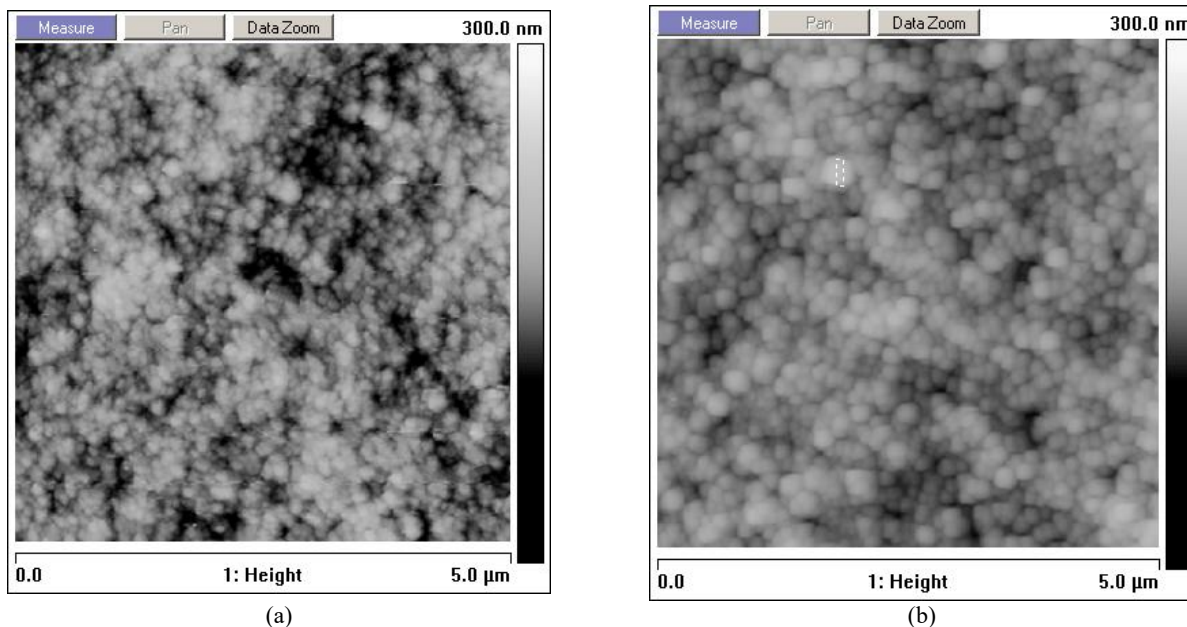
Figure 4. AFM topography of nc-TiO$_2$ film produced from (a) Batch A and (b) Batch B

Additionally, the batch A nc-TiO$_2$ films appear to have a large number of pin-holes in the surface compared with batch BTiO$_2$ films. This difference may be illustrated by extracting a profile of the particles across the film. Figure 5 shows a profile for particles and pin-holes in the batch A nc-TiO$_2$ film. It reveals several gaps between the nano-particles with the depth of the gap ranging from 80nm to100 nm.

Figure 6 shows a different profile for the batch B nc-TiO$_2$ film. The number of pin-holes was less than in batch B nc-TiO$_2$ films produced from. It also shows the existence of gaps between nano particles which range in depth from 10 nm to 30 nm and so much smaller than in the batch A nc-TiO$_2$ film.
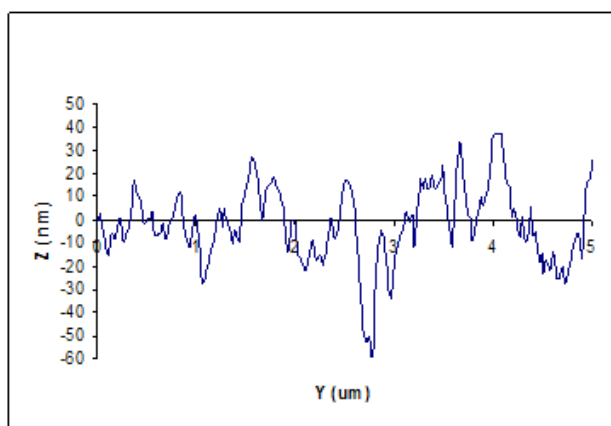
Figure 5. A profile of particles and pin-holes on surface of nc-TiO$_2$ film produced from batch A
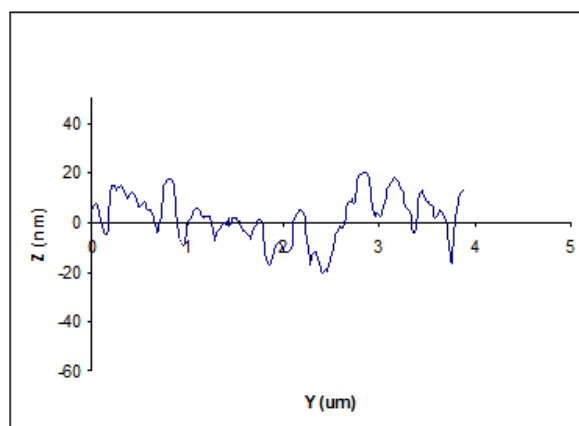
Figure 6. A profile of particles and pin-holes on surface of nc-TiO$_2$ film produced from batch B

Optical transmittance spectra of nc-TiO$_2$ films produced from batches A and B is shown in Figure 7. The light ransmission of the two nc-TiO$_2$ films was high for wavelength ranging from 720 nm to 500 nm. Below 350 nm, transmission was very poor in keeping with the optical band gap of the films [14]. Thus, nc-TiO$_2$ film is an attractive material to be used in solar cell fabrication since it allows visible light to pass through it with relatively little absorption. The slight difference of transmittance between the two samples is probably related to differences in thickness and degree of light scattering from the different morphologies.

The properties of the interface between polymer hole conductors and nc-TiO$_2$ play an important role in converting the light to photo current in metal oxide solar cell. Our measurements were made in air, the oxygen component of which is known to dope P3HT [15] and scavenging electron from the surface of the nc-TiO$_2$ layer leading to the production Ti4+ upon exposure to air [8]. From STS measurements, the surface potential energy of batch B nc-TiO$_2$ film is ~2.6 eV while batch A nc-TiO$_2$ film has surface potential energy gap energy of 3.3 eV similar to in the literature [13].

Figure 7. Transmittance spectra of the TiO$_2$ films from batches A and B

The lower value for batch B film corresponds to values obtained in sample kept in air for long period. The reduction is attributed to the formation of surface defects in nc-TiO$_2$ film. In the present case, samples were prepared on the day of the STS measurements so that the difference in the band gap probably indicates differences in the storage conditions of the nc-TiO$_2$ particles and its components. That may affect on alignment of the fermi levels in the P3HT and nc-TiO$_2$ and creation of a space-charge region (depletion region) at the interface between nc-TiO$_2$ and P3HT (see Figure 8). At the interface, the charge separation occurs in P3HT/nc-TiO$_2$ solar cell.

The latter results were confirmed by studying the electrical power-voltage (P-V) characteristics of typical solar cells fabricated from two different batches of nominally identical nc-TiO$_2$ sol-gel material. Figure 9 shows that the batch A nc-TiO$_2$/P3HT solar cells produces a high maximum electric power of 0.08 mW/cm^2 as compared to 0.01 mW/cm^2 for the Batch B nc-TiO$_2$/P3HT solar cells. Additionally, the range of operation of solar cells 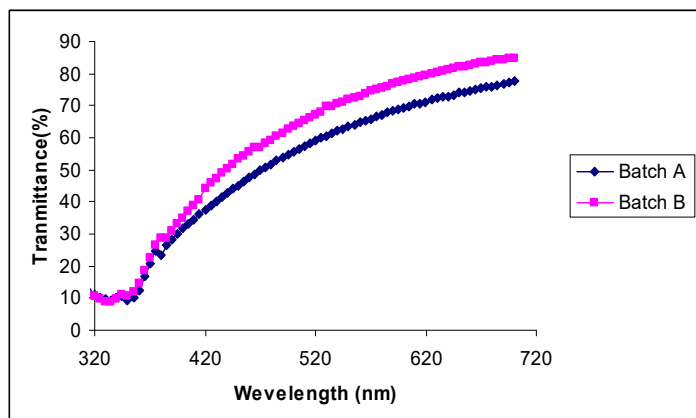starts from zero voltage to open circuit voltage, which was small in batch A nc-TiO$_2$/P3HT solar cells. That indicates to the difference in interfacial layers, which affect the generation of photo-current in the solar cells.
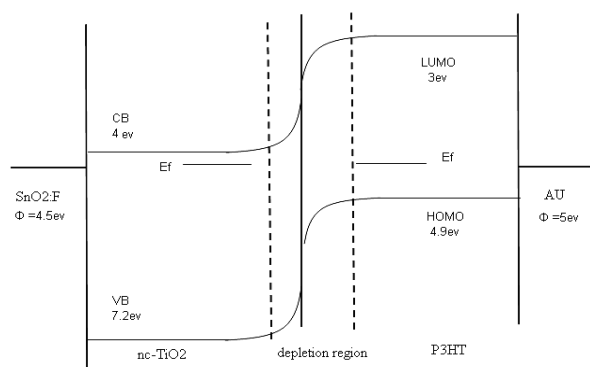
Figure 8. Schematic energy level diagram of a SnO2: Fn/nc-TiO$_2$/P3HT/Au solar cells
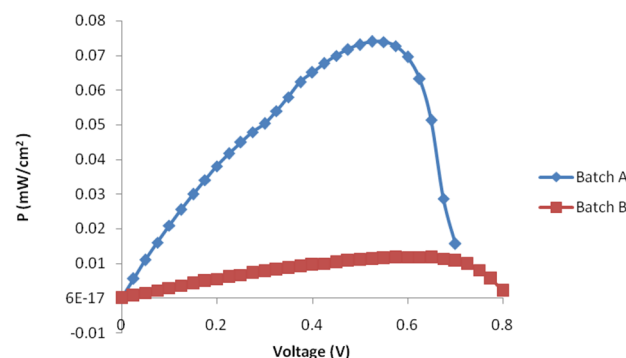
Figure 9. Electrical power versus voltage characteristics of batch A and batch B nc-TiO$_2$ solar cells

These results agree with previous works that the control of electrical surface potential and morphology of nc-TiO$_2$ could be used to enhance the performance of solar cells based on the nc-TiO$_2$ [9, 16, 17]. In this work, the more pine holes, randomly shape, small size of grain and surface electric potential of 3.3 eV in batch A TiO$_2$ solar cell led to increase its electrical power more than 8 times. It was ascribed to better adhesion of hole transport layer (P3HT) on the surface of the nc-TiO$_2$accompaniedby P3HT's atoms easily penetrating through small pine holes distributed on the top of the nc-TiO$_2$'s surface. Additionally, the reduction of electrical surface potential of batch B nc-TiO$_2$ from 3.3 to 2.6 eV and the formation of surface defects in nc-TiO$_2$ film decrease the efficiency charge separation and electrical power of batch B TiO$_2$ solar cells.

CONCLUSION

We have studied the surface electronic structure and morphological characteristics of the nc-TiO$_2$ films produced from two different batches. The result shows differences in surface band gap and morphological characteristics of nc-TiO$_2$ films. The batch A solar cells show best performance with high electric power of 0.08 mW/cm^2 while it is 0.01mW/cm^2 for batch B solar cells. That is attributed to the small particles ranging from ~120 nm to 150 nm, large number of pinholes in the surface and surface electric potential of 3.3 eV of batch A nc-TiO$_2$ films.

ORCID IDs
Hmoud Al Dmour, https://orcid.org/0000-0001-5680-5703

REFERENCES
[1] C. Leyens, and M. Peters, *Titanium and Titanium Alloys: Fundamental and Application*, (Wiley, VCH, 2003).

[2] M. Kralova, M. Vesely, and P. Dzik, "Physical and chemical properties of titanium dioxide printed layers", Catal. **161**(1), 97 (2011). https://doi.org/10.1016/j.cattod.2010.11.019

[3] H. Al-Dmour, RH. Alzard, H. Alblooshi, K. Alhosani, S. AlMadhoob, and N. Saleh, "Enhanced Energy Conversion of Z907-Based Solar Cells by Cucurbituril Macrocycles", Font.Chem. **561**, 1 (2019). https://doi.org/10.3389/fchem.2019.00561

[4] Y. Liang, and H. Ding, "Mineral-TiO_2 composites:Preparation and application in papermaking, paints and plastics", J. Alloys Compd. **844**, 156139 (2020). https://doi.org/10.1016/j.jallcom.2020.156139

[5] A. Fujishima, and K. Honda, "Electrochemical Photolysis of Water at a Semiconductor Electrode", Nature, **238**, 37(1972). https://doi.org/10.1038/238037a0

[6] K. Gopinath, N. Madhav, A. Krishnan, R. Malolan, and G. Rangarajan, "Present applications of titanium dioxide for the photocatalytic removal of pollutants from water: A review", J. Environ. Manage. **270**, 110906 (2020) https://doi.org/10.1016/j.jenvman.2020.110906

[7] B. O'Regan, and M. Grätzel, Nature, **353**, 373 (1991). https://doi.org/10.1038/353737a0

[8] I. Hao, J, Yan, S. Guan, L, Cheng, Q. Zhao, Z. Zhu, Y. Wang, Y. Lu, and J. Liu, "Oxygen vacancies in TiO_2/SnO coatings prepared by ball milling followed by calcination and their influence on the photocatalytic activity", Appl. Surf. Sci**. 466**, 490(2019). https://doi.org/10.1016/j.apsusc.2018.10.071

[9] H. Al Dmour, D.M. Taylor, and J.A. Cambridge, "Effect of nanocrystalline-TiO_2 morphology on the performance of polymer heterojunction solar cells", J. Phys. D, **40**(17), 5034 (2007). https://doi.org/10.1088/0022-3727/40/17/004

[10] F. Petronella, A. Pagliarulo, A. Truppi, M. Lettieri, M. Masieri, A. Calia, and R. Comparelli, "TiO_2 Nanocrystal Based Coatings for the Protection of Architectural Stone: The Effect of Solvents in the Spray-Coating Application for a Self-Cleaning Surfaces", Coating. **8**(10), 356 (2018). https://doi.org/10.3390/coatings8100356

[11] A. Thomas, and K. Syres, "Adsorption of organic molecules on rutile TiO_2 and anatase TiO_2 single crystal surfaces", Chem. Soc. Rev. **41**, 4207 (2012). https://doi.org/10.1039/c2cs35057b

[12] NT-MDT Spectrum Instruments, Proezd 4922, 4/3 Zelenograd, Moscow 124460, Russia, http://www.ntmdt.com

[13] C. Dette, O. Pérez, C. Kley, P. Punke, E. Patrick, P. Jacobson, F. Giustino, *et al*, "TiO_2 Anatase with a Bandgap in the Visible Region", Nano Lett. **14**(11), 6533 (2014). https://doi.org/10.1021/nl503131s

[14] A.A. Abd El-Moula, M. Raaif, and F.M. El-Hossary, "Optical Properties of Nanocrystalline/Amorphous TiO_2 Thin Film Deposited by rf Plasma Magnetron Sputtering", Acta Phys. Pol. A, **137**, 1068 (2020). https://doi.org/10.12693/APhysPolA.137.1068

[15] H. Al Dmour, and D.M. Taylor, "Revisiting the origin of open circuit voltage in nanocrystalline-TiO 2/polymer heterojunction solar cells", Appl. Phys. Lett.**94**, 223309 (2009). https://doi.org/10.1063/1.3153122

[16] M. Wu, J. Wu, C. Yen, H. Lo, F. Lin, and F. Su, "Correlation between nanoscale surface potential and power conversion efficiency of P3HT/TiO_2 nanorod bulk heterojunction photovoltaic devices", Nanoscale, **2**(28), 1448 (2010). https://doi.org/10.1039/b9nr00385a

[17] H. Al Dmour, "A Capacitance response of solar cells based on amorphous Titanium dioxide (A-TiO_2) semiconducting heterojunctions", AIMS Mater. Sci. **8**(2), 261 (2021). https://doi.org/10.3934/matersci.2021017

[18] W.J.E. Beek, M.M. Wienke, M. Kemerink, X. Yang, and R.A.J. Janssen, "Hybrid Zinc Oxide Conjugated Polymer Bulk Heterojunction Solar Cells", J. Phys. Chem. B, **109**, 9505 (2005). https://doi.org/10.1021/jp050745x

ВИКОРИСТАННЯ СПЕКТРОСКОПІЇ ТА ОПТИЧНОЇ МІКРОСКОПІЇ ДЛЯ ХАРАКТЕРИСТИКИ ТОНКІХ ПЛІВОК ДІОКСИДУ ТИТАНУ
Хмуд Аль-Дмур

Департамент фізики, факультет природничих наук, Університет Мута, Мута, 61710, Йорданія

У цій статті представлено електронну структуру поверхні та морфологічні характеристики плівок нанокристалічного діоксиду титану (nc-TiO_2), отриманих із двох різних золь-гелів. За допомогою скануючої тунельної мікроскопії/спектроскопії (STM/S) було виявлено, що частинки nc-TiO_2, отримані з партії A, мають ширину забороненої зони на поверхні ~3,3 еВ, тоді як частинки nc-TiO_2, отримані з партії B, мають ширину забороненої зони на поверхні. ~2,6 еВ. З іншого боку, дрібні частинки агрегували разом, щоб утворити більші частинки розміром від ~120 нм до 150 нм і розподілені випадковим чином по поверхні плівок партії A nc-TiO_2. Для плівок партії B nc-TiO_2 дрібні частинки утворили більші частинки, але їхній розмір коливається від 200 нм до 225 нм. Це пояснюється відмінностями між золь-гелями, що використовуються для отримання плівок nc-TiO_2. В результаті цього електрична потужність сонячних елементів Batch A nc-TiO_2/P3HT збільшена більш ніж у 8 разів у порівнянні з сонячними елементами Bach B.

Ключові слова: нанокристалічний діоксид титану; частинки/шпильки; поверхнева заборонена зона; пропускна здатність; вимірювання STS

ENHANCEMENT OF STRUCTURAL AND OPTICAL PROPERTIES OF CMC/PAA BLEND BY ADDITION OF ZIRCONIUM CARBIDE NANOPARTICLES FOR OPTICS AND PHOTONICS APPLICATIONS†

Majeed Ali Habeeb*, Zainab Sabry Jaber

University of Babylon, College of Education for Pure Sciences, Department of Physics, Iraq
Corresponding Author: pure.majeed.ali@uobabylon.edu.iq

Nanocomposites of (CMC-PAA-ZrC) made with different nano zirconium carbide percentages by casting method (0, 1.5, 3, 4.5, and 6 wt%). The results showed that FTIR spectra shift in peak position and change in shape and intensity, compared with pure (CMC-PAA) blend. Microscopic photographs show a clear difference in the samples when increasing proportions of zirconium carbide nanoparticles, when the concentration of zirconium carbide NP reached 6% wt, the nanoparticles make up a continuous network inside (CMC-PAA) blend. Structural and optical characteristics have investigated the findings showed that the absorption of (CMC-PAA-ZrC) nanocomposites increases with increasing of ZrC NPs, while transmission decrease. The absorption coefficient, extinction coefficient, refractive index, real and imaginary parts of dielectric and optical conductivity are increasing with rises concentration of ZrC. Also optical energy gap decreased from 4.9 eV to 4.05 eV and from 4.5 eV to 3.65 eV for allowed and forbidden indirect transition respectively with increasing ZrC NPs. The results indicate that the (CMC-PAA-ZrC) nanostructures can be considered as promising materials for optoelectronics applications.

Keywords: *Nanocomposites, structural Properties, Zirconium Carbide NPs, Optical Properties*
PACS: 78.20.Ci,78.20Ek,68.35.bm,81.05.-t

1. INTRODUCTION

In order to change mechanical, electrical, optical and thermal properties, to meet the required characteristics, new polymers, blends, combinations and advanced materials must be made. This development is parallel to comprehensive studies aimed at clarifying the relationship between the modified materials and the structure and the property [1]. New polymer films must be optically, electrically and thermally characterized in order to manufacture them, optical films, multipliers, full reflectors, narrow pass band filters, etc. may be used as transparent films [2]. The CMC is a major industrial polymer with numerous uses, detergents, textiles, paper, foods, medical products and well-boiled oil, including flocculation, drag reduction. CMC is a cellulose derivative that results from the reaction of sodium and chloroacetic acid. A number of cellulose molecules that have been introduced to promote water solubility have been contained in sodium carboxymethyl groups (CH_2COONa). Three factors depend on the diverse properties of CMC the molecular weight of the polymer, the average carboxyl content of the hydroglucose unit, and the distribution of carboxyl substitutes along the polymer chain [3,4]. Poly acrylic acid (PAA) has been gaining considerable interest due to its tremendous application in a variety of fields, including electrochemical, mechanical, biomedical, etc. It was widely used in various optical products, such as an effective corrosion inhibitor and eco-friendly platform, a solid lithium-ion electrolyte battery, super capacitors, ion replacements. PAA coatings can, in electronic and electrochemical applications, further improve the chemical stability of metal oxide nanoparticles. Thus, PAA related compounds are increasingly developed in the PAA matrix containing various oxide nanoparticles. Installations for physiotherapy [5,6]. For advanced temperature reactor fuels, zirconium carbide (ZrC) is an oxygen-based or inert-containing possible coating medium. ZrC has demonstrated desirable properties including excellent corrosion resistance and retention capabilities for fission product, for these fuel applications. However, ZrC processing results in stable sub stoic and carbon-rich compositions with and without major microstructural inhomogeneity and textural anisotropy, as well as phase separation, leading to physical, chemical, therapeutic and mechanical variations. Zirconium carbide (ZrC) is part of a class of materials known as ultra-high temperature ceramics (UHTCs) because of their high melting points (3550°C), low densities (6.7 g/cm^3), and strong thermal conductivity. The results of high-temperature neutron irradiation remain poorly understood at present [7]. Each bulk material, however, has low fracture strength, low resistance to oxidation and sintering potential, which limits its use in harsh environments. Zirconium carbide (ZrC) has both ceramic and metallic properties, such as one of the highest very high hardness (30-35 GPa) melting point, good wear resistance [8].

2. EXPERIMENTAL PART

In this work, 30% poly acrylic acids (PAA) and 70% carboxy methylcellulose (CMC) were prepared in 90 ml of distilled water with magnetic stirrer to achieve more homogeneous solution at temperature 80 C for 30 minutes. ZrC nanoparticles were added with concentrations (0, 1.5, 3, 4.5 and 6) wt% by using casting method. Using the microwave instead of traditional heat devices, as the use of a microwave oven reduces the reaction time and leads to obtaining a

---

homogeneous solution and nanoparticles uniform in size and shape. Absorption spectra were recorded for (CMC-PAA-ZrC) nanocomposites in the wavelength range (200–800) nm, double beam spectrophotometer (UV/1800/Shimadzu) at room temperature the absorption spectrum was registered and used to obtain optical constants, absorption coefficient, extinction coefficient, refractive index and energy gap. To make additional remarks about the homogeneity in distributing zirconium carbide, the effect of the filler and the existence of impurities, a test for samples was conducted in different concentrations using an Olympus type Nikon-73346 optical microscope which has a magnifying power of (100×) and equipped with a camera used in the microscopic photography. FTIR spectra have been investigated by FTIR in the range of wave numbers (500-4000) cm^{-1} (Bruker company, German origin, type vertex-70). The following equation is calculated absorbance (A) [9]:

$$A = \frac{I_A}{I_\circ} \tag{1}$$

where: I_A is the intensity of light absorbed by material and Io is the intensity of light incident.

Transmittance (T) is computed as the following equation: [19]

$$T = \exp(-2.303\ A) \tag{2}$$

The following equation is calculated for absorption coefficient (α): [11]

$$\alpha = 2.303\ A/t \tag{3}$$

where t is the thickness of the sample

The indirect transition calculated by using relation: [12]

$$\alpha h\upsilon = B(h\upsilon - Eg)^r \tag{4}$$

where: B is fixed, hυ is photon energy, Eg is optical band gap, r = 2 is permitted indirect, and r = 3 is prohibited indirectly.

The coefficient of extinction (k) was determined using the equation below: [13]

$$K = \frac{\alpha \lambda}{4\pi} \tag{5}$$

where λ is the wavelength

Calculated refractive index (n) from equation: [14]

$$n = \sqrt{\frac{4R - k^2}{(R-1)^2} - \frac{(R+1)}{(R-1)}} \tag{6}$$

where: R is a reflection

Dielectric constant (real ε_1 and imaginary ε_2) parts are calculated by: [15]

$$\varepsilon_1 = n^2 - k^2 \tag{7}$$

$$\varepsilon_2 = 2nk \tag{8}$$

The optical conductivity (σ) is obtained by using the relation: [16]

$$\sigma = \frac{\alpha n c}{4\pi} \tag{9}$$

where: c is the velocity of light

3. RESULTS AND DISCUSSION

Figure 1 shows FTIR has been used to analyze the interactions among it interacts with the molecule because it has a dipole electric in (CMC-PAA-ZrC) nanocomposites. These interactions can include changes in the vibrational modes of the nanocomposites. The (FTIR) transmittance spectra of (CMC-PAA-ZrC) nanocomposites films with the different ratio of ZrC nanoparticles are shown in figure 1(A)–(E) are recorded at room temperature in the range (500–4000) cm^{-1}. It can be seen from the figure that the wide bands are observed at about (3566-3902) cm^{-1} due to OH groups. The band corresponding to CH2 asymmetric stretching vibration occurs at about 2360 cm^{-1}. The peaks at 1541 and 1698 cm^{-1} have been attributed to the CO, CC stretching mode. The absorbent peak at around (1338–1868) cm^{-1} belongs to CO group. The band relating to the poly acrylic acid CO group is located at 1698 cm^{-1}. In case of (CMC-PAA-ZrC) with different ZrC ratio, compared to pure (CMC-PAA) blend, FTIR spectra display variations in peak position as well as changes in form and strength. This shows the decoupling of two polymers and zirconium carbide nanoparticles between the related vibrations, the deviation towards greater or smaller wavelengths occurs as a result of compensation or the effect of solvents, as for the vertical displacement, it indicates an increase or decrease in the absorption value [17,18].

Figure 2 shows the optical microscope images of (CMC-PAA-ZrC) NCs taken at a magnification power of 10× for specimens with different concentrates of ZrC nanoparticles. When the proportion of zirconium carbide nanoparticles (shown in the images B, C, D, and E) is increased by microscopic photos, after the addition of the nanoparticulate content of ZrC a network is formed in the main phase of the (CMC-PAA) blend. This network has paths along which carriers will travel the paths that have a declining resistivity of the (CMC-PAA) blend [19].

(A)

(B)

(C)

(D)

(E)

Figure 1. FTIR spectra for (PAA-CMC-ZrC) nanocomposites. (A) (PAA-CMC) blend, (B) 1.5 wt.% ZrC nanoparticles, (C) 3 wt.% ZrC nanoparticulates,(D) 4.5 wt.% ZrC nanoparticulates, (E) 6 wt.% ZrC nanoparticulates

Figure (3) shows variation of optical absorbance with wavelength for (CMC-PAA-ZrC) nanocomposites. From this figure the absorption is increased in the ultraviolet region and decreases in visible and infrared region, since the incident photon has a high wavelength and the photon is not transmitted because there is not enough energy to communicate with

atoms. The photon-material interaction occurs and the photon absorbs as the wavelength decreases. The absorbance increases with increasing of ZrC concentration, this is due to free electrons absorbing the incident light [20,21].

Figure (4) shows the transmittance spectrum for (PAA-CMC-ZrC) nanocomposites as a function of wavelength. The transmission decreases with increase of the concentration of ZrC nanoparticles. The method is not followed by emission from the radiation because the transferred electrons in its outer orbits have occupied vacancy positions of the energy bands, absorb part of the light incident that does not exceed a material dosage which is induced by ZrC electrons on their outer orbits and transmits them to higher energy levels [22,23].

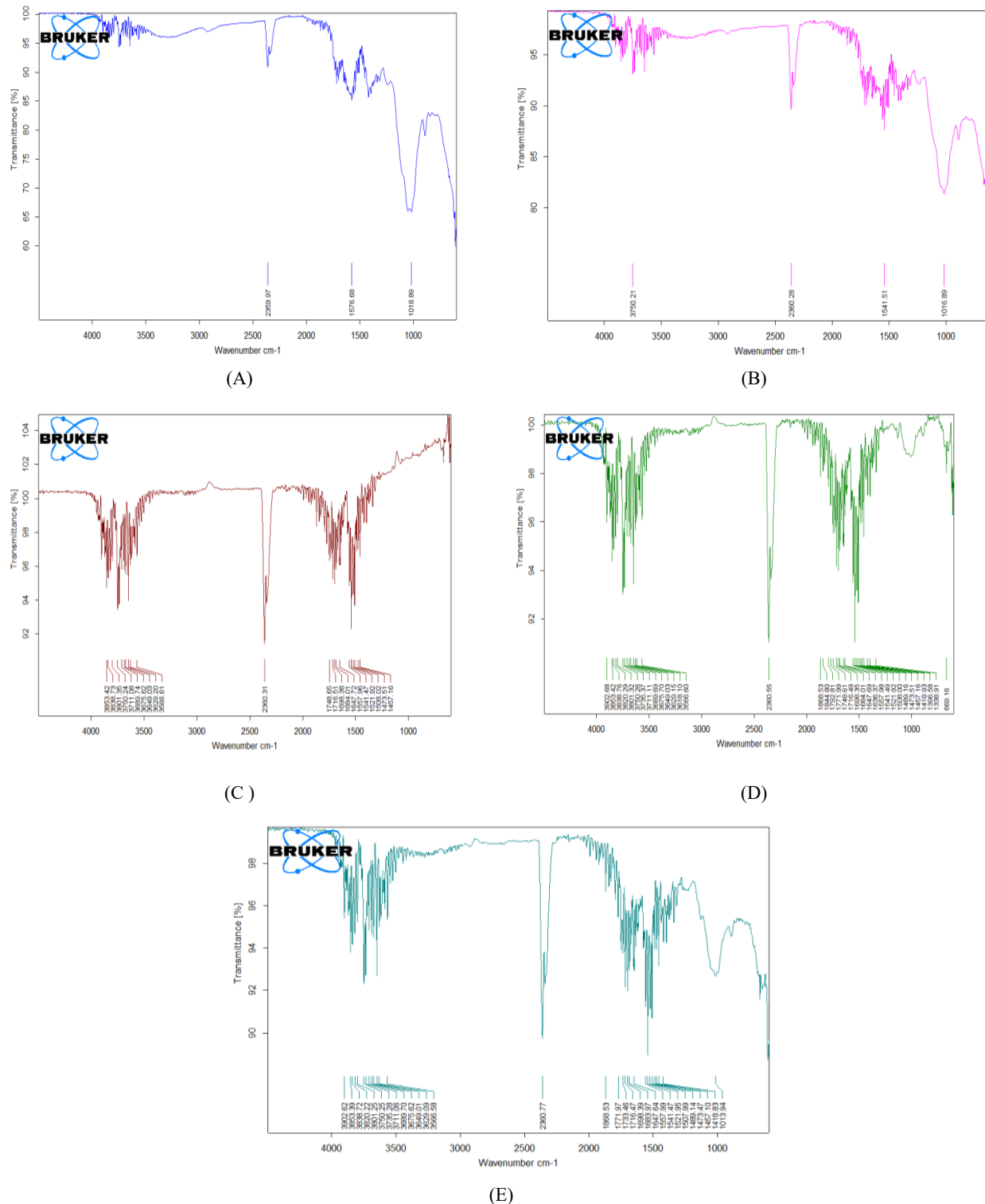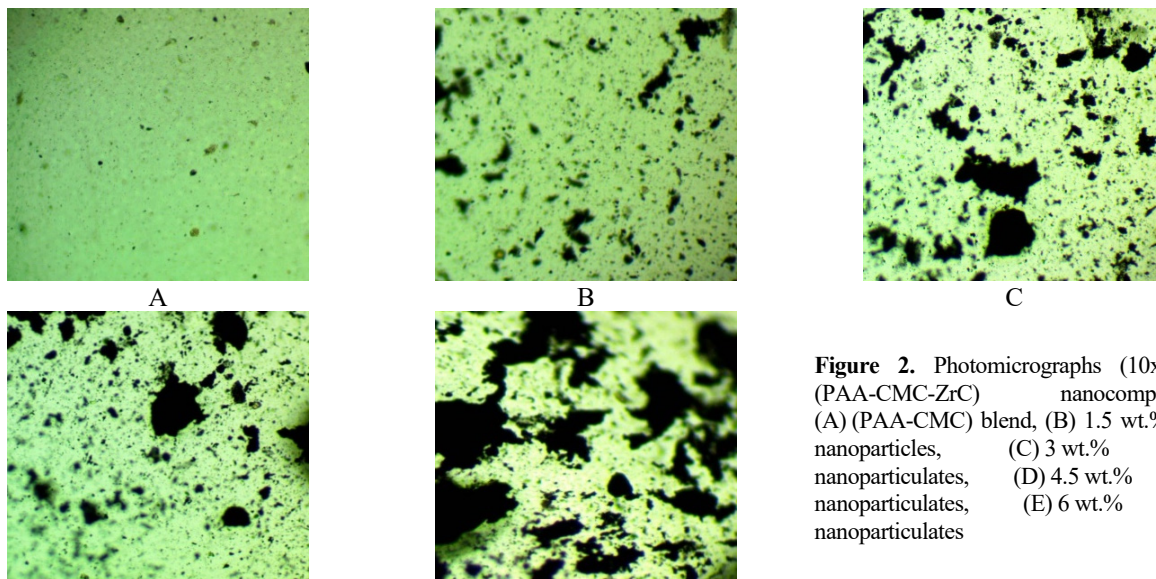**Figure 2.** Photomicrographs (10x) for (PAA-CMC-ZrC) nanocomposites: (A) (PAA-CMC) blend, (B) 1.5 wt.% ZrC nanoparticles, (C) 3 wt.% ZrC nanoparticulates, (D) 4.5 wt.% ZrC nanoparticulates, (E) 6 wt.% ZrC nanoparticulates

The relation between the absorption coefficient and wavelength of (PAA-CMC-ZrC) nanocomposites shown in Figure 5. The absorption coefficient helps to illustrate the nature of electron transfer. When the absorption coefficient values of nanocomposites (CMC-PAA-ZrC) are strong $\alpha > 10^4$ cm^{-1}, the electron is passed directly. Although the absorption factor values of nanocomposites are tiny at $\alpha < 10^4$ cm^{-1}, the electron transfer is indirectly. We can see that with the rise in the concentrations of ZrC nanoparticles, the absorption coefficient is increased, due to increased carriers of charge [24], the absorption and absorption coefficient of (CMC-PAA-ZrC) NCs are also enhanced.
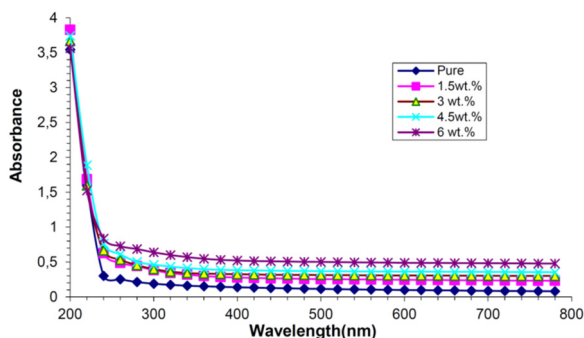
Figure 3. Absorbance spectra with photon wavelength for (PAA-CMC-ZrC) nanocomposites

Figure 4. Transmittance spectra of (CMC-PAA-ZrC) nanocomposites as a function of wavelength

Figure 5. Variation of absorption coefficient for (CMC-PAA-ZrC) NCs with photon energy

Figure 6. The relationship between $(\alpha h\nu)^{1/2}$(cm^{-1}·eV)$^{1/2}$ and photon energy of (CMC-PAA-ZrC) nanocomposites

Figure 6 demonstrates the relationship between absorption edge $(\alpha h\nu)^{1/2}$ and photons energy. This figure indicates an energy gap decreased by an increase in ZrC concentration for (CMC-PAA-ZrC) nanocomposites, this is because the material has risen in disruption, which means that the secondary excitation within the band can be made possible and the width of these levels increases with increasing concentrations of ZrC NPs, that minimize the energy gap [25,26.

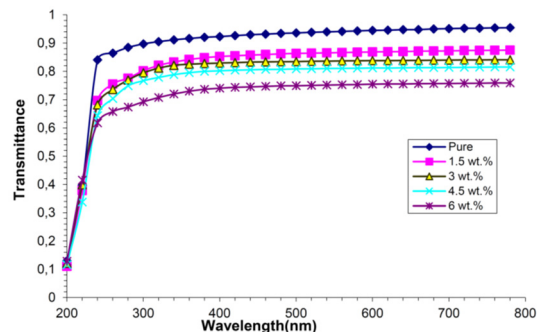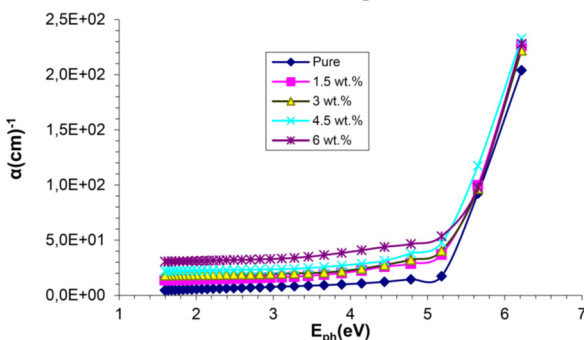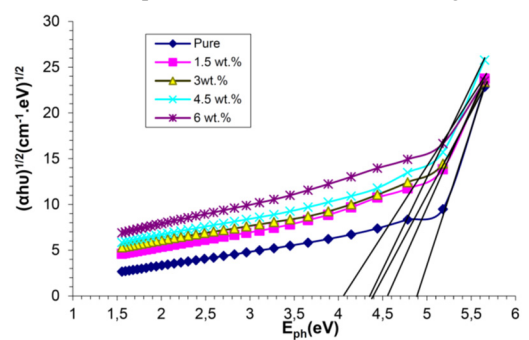The relation between $(\alpha h\nu)^{1/3}(cm^{-1}\cdot eV)^{1/3}$ and photon energy of **(CMC-PAA-ZrC)** nanocomposite is shown in Figure 7. This figure obvious that the energy gap values for prohibited indirect transition decline, this result is explained because the density of localized states increased with a rise in the concentration of ZrC nanoparticles [27]. As well as values of prohibited indirect transition are lower than the permitted indirect transition.

The change in the extinction coefficient is seen in Figure 8 as a function of wavelength. With an increase in ZrC nanoparticles we have noticed that the extinction coefficient increases. This is because the absorption value is enhanced and the ZrC nanoparticles weight percentage is increased. Variation the extinction coffiecient with wavelength of (PAA-CMC-ZrC) nanocomposites there is an effect of the geometric structure of the material on the tops extinction coefficient, when the percentage of nanomaterial increases, the proportion of geometric deformation increases in the crystal lattice [28-30].
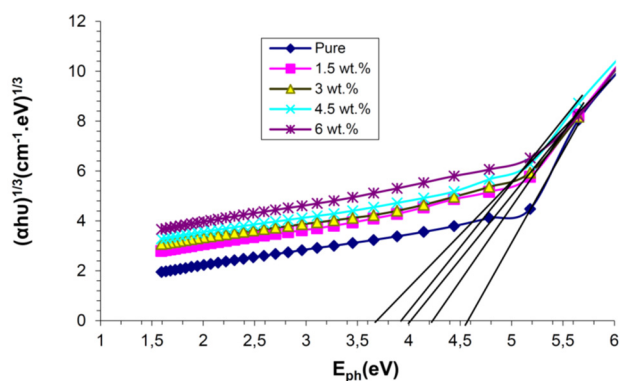
Figure 7. The relationship between $(\alpha h\nu)^{1/3}(cm^{-1}\cdot eV)^{1/3}$ and photon energy for (CMC-PAA-ZrC) NCs
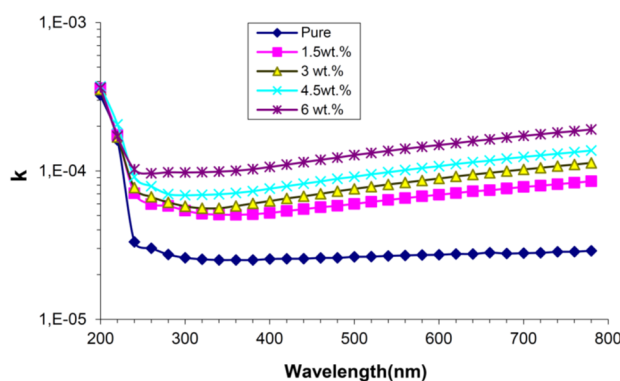
Figure 8. Variation of extinction coefficient with wavelength of (PAA-CMC-ZrC) nanocomposites

Figure 9 shows the relationship between the refractive index and wavelength for (CMC-PAA-ZrC) nanocomposites. From this figure it can be seen by increases the concentration of ZrC nanoparticles the refractive index increases for all samples of (CMC-PAA-ZrC) nanocomposites. The ultraviolet region shows high refractive index values due to low transmission in this region however, due to the high transmission in this region, the visual and near IR regions notice low values [31,32].
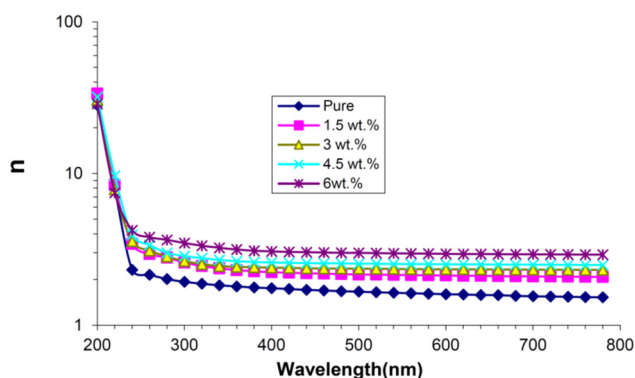
Figure 9. As a function of wavelength, refractive index for (PAA-CMC-ZrC) nanocomposites
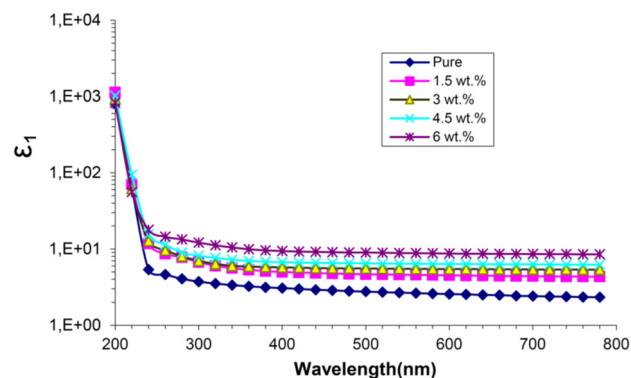
Figure 10. As a function of wavelength the actual dielectric constant for (PAA-CMC-ZrC) nanocomposites

Figure 10 indicates the difference between the actual part of the dielectric constant with wavelength. These graphs demonstrate how raising the concentration ratio of ZrC NPs enhanced real part of dielectric constant. The rise in electrical polarization in the nanocomposites is responsible for this. On the other hand variation of ε_1 is primarily, depends on the n^2 because of little k^2 values, whereas ε_2 is mainly dependent on k values, the variations in the absorption coefficient are related to [33,34], as shown in Figure 11.

The relationship between optical conductivity and wavelength for (PAA-CMC-ZrC) nanocomposites is shown in Figure 12. It is noted that with increased zirconium carbide nanoparticles, optical conductivity increases. This behavior is attributed to the formation of localized states in the energy gap; increasing the concentrations of ZrC nanoparticles

causes a rise in the density of localized levels in the energy gap, which raises the absorption coefficient and, as a result, the optical conductivity of the nancomposites [35,36].
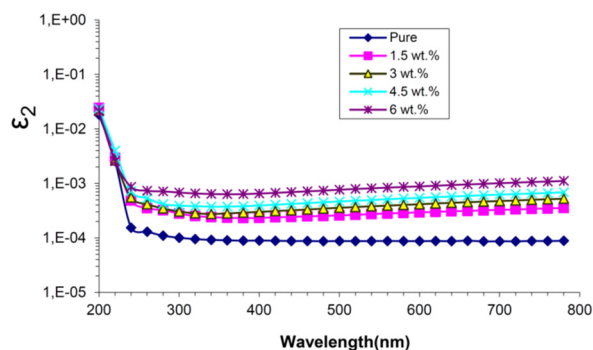
Figure 11. Change imaginary dielectric constant with wavelength for nanocomposites of (PAA-CMC-ZrC)
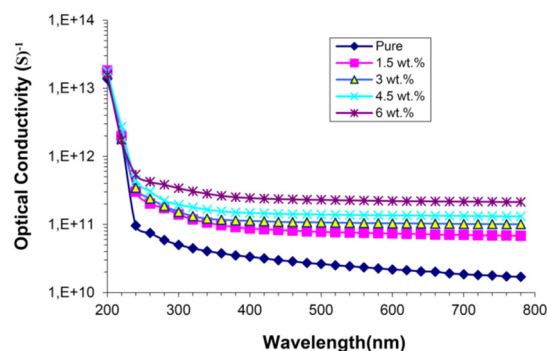
Figure 12. Optical conductivity of (PAA-CMC-ZrC) NCs as a function of wavelength

4. CONCLUSION

1 - FTIR spectrum shows both a difference in peak position, form and strength in contrast to the pure (CMC-PAA) blend. This suggests the disassociation between the vibrations in the two polymers and the zirconium carbide nanoparticles.

2 - Optical microscope appear forming a continuous network within polymers when the ratio of zirconium carbide nanoparticles reached (6 wt%).

3 - Absorbance of (CMC-PAA-ZrC) NCs increase with increasing of concentration of ZrC nanoparticles, while transmittance and energy gap of this nanocomposites decreases.

4 - The absorption coefficient, extinction coefficient, refractive index, real and imaginary part of the dielectric constants and the optical conductivity rise with an increase in the zirconium carbide weight percentage.

This finding suggests that (CMC-PAA-ZrC) nanocomposites are a good choice for use in different electronic and photonics applications.

ORCID IDs

Ⓘ**Majeed Ali Habeeb,** https://orcid.org/0000-0001-5064-2835

REFERENCES

[1] J.B. Bhaiswar, M. Salunkhe, S.P. Dongre, and B.T. Kumbhare, "Comparative study on thermal stability and optical properties of PANI/Cds and PANI/Pbs nanocomposite", IOSR Journal of Applied Physics, International Conference on Advances in Engineering and Technology, **80**, 79-82 (2014). https://www.academia.edu/download/32958244/2014_Journal_of_Applied_Physics_PP_79-82.pdf

[2] S.M. Mahdi, M.A. Habeeb, "Evaluation of the influence of SrTiO3 and CoO nanofillers on the structural and electrical polymer blend characteristics for electronics devices", Digest Journal of Nanomaterials and Biostructures, **17**(3), 941-948 (2022). https://doi.org/10.15251/DJNB.2022.173.941

[3] H.N. Obaid, M.A. Habeeb, F.L. Rashid, and A. Hashim, "Thermal energy storage by nanofluids", Journal of Engineering and Applied Sciences, **8**(5), 143-145 (2013). https://doi.org/10.36478/jeasci.2013.143.145

[4] J. Li, Z.Y. Fu, W.M. Wang, H. Wang, S.H. Lee, and K. Niihara, "Preparation of ZrC by self-propagating high-temperature synthesis", Ceram. Int. **36**(5), 1681–1686, (2010). https://doi.org/10.1016/j.ceramint.2010.03.013

[5] D. Craciun, G. Socol, G. Dorcioman, S. Niculaie, G. Bourne, J. Zhang, E. Lambers, K. Siebein, and V. Craciun, "Wear resistance of ZrC/TiN and ZrC/ZrN thin multilayers grown by pulsed laser deposition", Appl. Phys. A, **110**, 717–722, (2013). https://doi.org/10.1007/s00339-012-7224-8

[6] M.A. Habeeb, "Effect of rate of deposition on the optical parameters of GaAs films", European Journal of Scientific Research, **57**(3), 478-484, (2011).

[7] A. Gautam, and S. Ram, "Preparation and Thermomechanical Pro-perties of Ag-PVA Nanocomposite Films", Mater. Chem. Phys. **119**, 266-271 (2010). https://doi.org/10.1016/j.matchemphys.2009.08.050

[8] S.M. Mahdi, and M.A. Habeeb, "Synthesis and augmented optical characteristics of PEO–PVA–SrTiO3–NiO hybrid nanocomposites for optoelectronics and antibacterial applications", Optical and Quantum Electronics, **54**(12), 854 (2022). https://doi.org/10.1007/s11082-022-04267-6

[9] N. Hayder, M.A. Habeeb, and A. Hashim, "Structural, optical and dielectric properties of (PS-In2O3/ZnCoFe2O4) nanocomposites", Egyptian Journal of Chemistry", **63**, 577-592 (2020). https://doi.org/10.21608/ejchem.2019.14646.1887

[10] M. Caglar, S. Ilican, and Y. Caglar, "Influence of Dopant Concentration on the Optical Properties of ZnO: In Films by SolGel Method", Thin Solid Films, **517**, 5023-5028 (2009). https://doi.org/10.1016/j.tsf.2009.03.037

[11] A.H. Hadi, and M.A. Habeeb, "Effect of CdS nanoparticles on the optical properties of (PVA-PVP) blends", Journal of Mechanical Engineering Research an Developments, **44**(3), 265–274 (2021). https://jmerd.net/Paper/Vol.44,No.3(2021)/265-274.pdf

[12] Q.M. Jebur, A. Hashim, and M.A. Habeeb, "Structural, A.C electrical and optical properties of (polyvinyl alcohol-polyethylene oxide-aluminum oxide) nanocomposites for piezoelectric devices", Egyptian Journal of Chemistry, **63**, 719-734, 2020. https://dx.doi.org/10.21608/ejchem.2019.14847.1900

[13] M. Mahsan, C. Sheng, M. Isa, E. Ghapur, E. Ali, and M. Razali, "Structural and Physical Properties of PVA/TiO2 Composite", in: *Malaysia Polymer International Conference*,10 (2009).

[14] A.H. Hadi, and M.A. Habeeb, "The dielectric properties of (PVA-PVP-CdS) nanocomposites for gamma shielding applications", Journal of Physics: Conference Series, **1973**(1), 012063 (2021).

[15] M.A. Habeeb, A. Hashim, and N. Hayder, "Fabrication of (PS-Cr2O3/ZnCoFe2O4) nanocomposites and studying their dielectric and fluorescence properties for IR sensors", Egypt. J. of Chem. **63**, 709-717 (2020). https://dx.doi.org/10.21608/ejchem.2019.13333.1832

[16] K. Sivaiah, B.H. Rudramadevi, S. Buddhudu, G.B. Kumara, and Varadarajulu, "Structural, thermal and optical properties of Cu2+ and Co2+: PVP polymer films", Indian Journal of Pure and Applied Physics, **48**(9), 658-662 (2010). http://nopr.niscpr.res.in/bitstream/123456789/10157/1/IJPAP%2048%289%29%20658-662.pdf

[17] A. Hashim, M.A. Habeeb, and Q.M. Jebur, "Structural, dielectric and optical properties for (Polyvinyl alcohol-polyethylene oxide manganese oxide) nanocomposites", Egyptian Journal of Chemistry, **63**, 735-749 2020. https://dx.doi.org/10.21608/ejchem.2019.14849.1901

[18] A. Tawansi, A. El-khodary, H.M. Zidan, and S.I. Badr, "The effect of MnCl2 filler on the optical window and the physical properties of PMMA films", Polymer Testing, **21**(4), 381-387 (2002). https://doi.org/10.1016/S0142-9418(01)00100-3

[19] Q.M. Jebur, A. Hashim, and M.A. Habeeb, "Fabrication, structural and optical properties for (Polyvinyl alcohol-polyethylene oxide iron oxide) nanocomposites", Egyptian Journal of Chemistry, **63**(2), 611-623 2020. https://dx.doi.org/10.21608/ejchem.2019.10197.1669

[20] D. Qin, G. Yang, L. Zhang, X. Du, and Y. Wang, "Synthesis and Optical Characteristics, of PAM/HgS", Nanocomposites, Journal of Bull. Korean Chem. Soc. **35**(4), (2014). https://doi.org/10.5012/bkcs.2014.35.4.1077

[21] M.A. Habeeb, and W.S. Mahdi, "Characterization of (CMC-PVP-Fe2O3) nanocomposites for gamma shielding application", International Journal of Emerging Trends in Engineering Research, **7**(9), 247-255 2019. https://doi.org/10.30534/ijeter/2019/06792019

[22] N.B.V. Crasta, R. Kumar, and B.M. Praveen, "Advancement in Microstructural, Optical, and Mechanical Properties of PVA (Mowiol 10-98) Doped by ZnO Nanoparticles", Phys. Res. Int. **2014**, 742378 (2014). https://doi.org/10.1155/2014/742378

[23] M.A. Habeeb, and R.S.A. Hamza, "Synthesis of (polymer blend –MgO) nanocomposites and studying electrical properties for piezoelectric application", Indonesian Journal of Electrical Engineering and Informatics, 6(4), 428-435 (2018). https://doi.org/10.11591/ijeei.v6i1.511

[24] R. Tintu, K. Saurav, K. Sulakshna, V.P.N. Nampoori, P. Radhakrishnan, and S. Thomas, "Ge28Se60Sb12/PVA composite films for photonic applications", J. Non-Oxide Glas. **2**(4), 167–174 (2010). https://chalcogen.ro/167_Tintu.pdf

[25] M.A. Habeeb, and R.S.A. Hamza, "Novel of (biopolymer blend-MgO) nanocomposites: Fabrication and characterization for humidity sensors", Journal of Bionanoscience, **12**(3), 328-335 (2018). https://doi.org/10.1166/jbns.2018.1535

[26] J. Selvi, S. Mahalakshmi, and V. Parthasarathy, "Synthesis, structural, optical, electrical and thermal studies of polyvinyl alcohol/CdO nanocomposite films", Journal of Inorganic and Organometallic Polymers and Materials, 27, 1918-1926 (2017).

[27] M.A. Habeeb, A. Hashim, and N. Hayder, "Structural and optical properties of novel (PS-Cr2O3/ZnCoFe2O4) nanocomposites for UV and microwave shielding", Egypt. J. Chem. **63**, 697-708 (2020). https://dx.doi.org/10.21608/ejchem.2019.12439.1774

[28] S. Choudhary, "Structural, optical, dielectric and electrical properties of (PEO–PVP)–ZnO nanocomposites", J. Phys. Chem. Solids, **121**, 196–209 (2018). https://doi.org/10.1016/j.jpcs.2018.05.017

[29] N.K. Abbas, M.A. Habeeb, and A.J.K. Algidsawi, "Preparation of chloro-penta-amine Cobalt (III) chloride and study of its influence on the structural and some optical properties of polyvinyl acetate", International Journal of polymer Science, **2015**, 926789 (2015). https://doi.org/10.1155/2015/926789

[30] M. Pattabi, B.S. Amma, and K. Manzoor, J. Mater. "Optical Parameters of AgNO3 Doped Poly-Vinyl Alcohol Films", Res. Bull. **24**, 828-835 (2007).

[31] M.A. Habeeb, and W.K. Kadhim, "Study the optical properties of (PVA-PVAC-Ti) nanocomposites", Journal of Engineering and Applied Sciences, **9**(4), 109-113 (2014). https://doi.org/10.36478/jeasci.2014.109.113

[32] N.S. Waghuley, and S.A. Wadatkar, "Complex optical studiesnon conducting polyindoleas-synthesized through chemical route", Egypt. J. Basic Appl. Sci. **2**, 19 (2015).

[33] M. Ghanipour, and D. Dorranian, "Effect of Ag-Nanoparticles Doped in Polyvinyl Alcohol on the Structural and Optical Properties of PVA Films", Journal of Nanomaterials, **2013**, (2013).

[34] M.A. Habeeb, "Dielectric and optical properties of (PVAc-PEG-Ber) biocomposites", Journal of Engineering and Applied Sciences, **9**(4), 102-108 (2014). https://doi.org/10.36478/jeasci.2014.102.108

[35] V.M. Mohan, P.B. Bhargav, V. Raja, A.K. Sharma, and V.V.R.N. Rao, "Optical and Electrical Properties of Pure and Doped PEO Polymer Electrolyte Films", Soft Mater. **5**, 33–46 (2007).

[36] S. Kramadhati, and K. Thyagarajan, "Optical Propertiesof Pure and Doped (Kno3 & Mgcl2) PolyvinylAlcohol Polymer Thin Films", Int. Journal of Engineering Research and Development, **6**(8), (2013).

ПОЛІПШЕННЯ СТРУКТУРНИХ ТА ОПТИЧНИХ ВЛАСТИВОСТЕЙ СУМІШІ CMC/PAA ШЛЯХОМ ДОДАВАННЯ НАНОЧАСТИНОК КАРБІДУ ЦИРКОНІЮ ДЛЯ ОПТИКИ ТА ФОТОНІКИ

Маджід Алі Хабіб, Зейнаб Сабрі Джабер
Вавилонський університет, Коледж освіти для чистих наук, Фізичний факультет, Ірак

Нанокомпозити (CMC-PAA-ZrC), виготовлені з різним процентним вмістом нанокарбіду цирконію методом лиття (0, 1,5, 3, 4,5 і 6 мас.%). Результати показали, що спектри FTIR зміщуються в положенні піку та змінюють форму та інтенсивність порівняно з чистою сумішшю (CMC-PAA). Мікроскопічні фотографії показують чітку різницю в зразках при збільшенні частки наночастинок карбіду цирконію, коли концентрація NP карбіду цирконію досягла 6% мас., наночастинки складають безперервну мережу всередині суміші (CMC-PAA). Досліджено структурні та оптичні характеристики. Результати показали, що поглинання нанокомпозитів (CMC-PAA-ZrC) збільшується зі збільшенням кількості наночастинок ZrC, а пропускання зменшується. Коефіцієнт поглинання, коефіцієнт екстинкції, показник заломлення дійсної та уявної частини діелектричної та оптичної провідності зростають із збільшенням концентрації ZrC. Крім того, розрив оптичної енергії зменшується з 4,9 еВ до 4,05 еВ і з 4,5 еВ до 3,65 еВ для дозволеного та забороненого непрямого переходу відповідно зі збільшенням наночастинок ZrC. Результати показують, що наноструктури (CMC-PAA-ZrC) можна розглядати як перспективні матеріали для застосування в оптоелектроніці.

Ключові слова: нанокомпозити, структурні властивості, НЧ карбіду цирконію, оптичні властивості

PREPARATION AND CHARACTERIZATION OF Cu₂CrSnS₄ THIN FILMS DEPOSITED AT DIFFERENT TEMPERATURES[†]

Huda Talib[a,b], Nabeel A. Bakr[a]*, Mohammed A. Abed[b]

ᵃDepartment of Physics, College of Science, University of Diyala, Diyala, Iraq
ᵇDiyala General Directorate of Education, Diyala, Iraq
*Corresponding Author: nabeelalibakr@yahoo.com

In this study, Cu_2CrSnS_4 thin films are prepared using chemical pyrolysis technique at various deposition temperatures (200, 250, 300, 350, 400 and 450 °C) and without any annealing process. The structure characteristics of the films have been studied by X ray diffraction (XRD), micro-Raman spectroscopy, and Field Emission Scanning Electron Microscope (FESEM), while the optical characteristics are investigated by UV-Visible spectrophotometry, and the electrical properties aree described by Hall Effect test. Results of XRD for Cu_2CrSnS_4 (CCTS) films showed the tetragonal crystal structure of stannite phase with (112) preferred orientation. The results of Raman spectroscopy of the prepared CCTS thin films showed a clear peak at ~ 336 cm^{-1}. Furthermore, the morphology results and through (FESEM) images of thin films surface showed different forms and shapes with different granular size ranging from 40 to 294 nm. Optical examination of the ultraviolet-visible spectrum showed an optical energy gap of (1.69-1.59 eV) which are considered to be suitable for thin films solar cells applications. The electrical measurements through Hall Effect test showed that the films have charge carriers of (p-type). From results analysis, the optimized temperature of the prepared (CCTS) samples was 350 ºC.
Keywords: Cu_2CrSnS_4, Spray pyrolysis, Deposition temperature, XRD analysis, UV-Visible Spectroscopy, Hall Effect.
PACS: 88.40.jn; 73.61.−r; 81.15.Rs; 61.82.Fk; 78.20.−e

Due to the high values of absorption coefficient with suitable energy gap, the chalcogenides based on Cu showed promised future as effective materials for various applications. [1]. Cu_2CrSnS_4 (CCTS) material is interesting thanks to its positive characteristics for different optoelectronic applications [2, 3]. There are different techniques which can be used to deposit thin films of these types of materials such as chemical and physical methods. The spray pyrolysis method has many benefits such as that it is a cost-effective technique which does not need expensive and complicated parts and it is safe and friendly technique [4]. Many reports on the preparation of quaternary chalcogenide films were carried out by this method. Khodair et al. succeeded in preparing CZTS thin films [5]. Abed et al. deposited Cu_2FeSnS_4 films on soda-lime slides at different temperatures by the same technique [6]. The goal of this study is the investigation of preparation temperature impact on the structure and the optical, as well as the electronic characteristics of CCTS thin films prepared using spray pyrolysis method and to get good quality and homogeneous samples which are desirable as solar cell absorber layer.

EXPERIMENTAL PROCEDURE

The solution used to deposit the Cu_2CrSnS_4 (CCTS) films deposition has been prepared by dissolving 0.01 M of copper acetate monohydrate $(Cu(CH_3.COO)_2.H_2O)$ (Thomas Baker), 0.005 M of chromium chloride hexahydrate $(CrCl_3.6H_2O)$ (Central Drug House), 0.005 M of tin chloride $(SnCl_2.2H_2O)$ (Thomas Baker), and 0.004 M of thiocarbamide $(SC(NH_2)_2)$ (BDH Chemicals Ltd.) in 0.1 l of distilled water. The concentration of thiocarbamide used is doubled to overcome the evaporation process. The detailed procedure is reported elsewhere [7].

RESULTS AND DISCUSSION

The XRD patterns of the deposited CCTS films at different substrate temperatures (200-450°C) and thickness of 300 nm are displayed in Figure 1. The patterns have clear peaks at 28.42°, 47.26° and 56.12° attributed to 112, 220 and 312 planes respectively which belong to the stannite tetragonal phase of CCTS material [8]. From the figure, it can be seen that there are no other peaks belonging to ternary and binary materials [9,10]. The standard card (00-031-0462) of the compound copper iron zinc tin sulfide $(Cu_4FeZnSnS_8)$ was adopted for matching the present XRD patterns due to the lack of entries in the database of the International Center for Diffraction Data (ICDD) for the quaternary compound (Cu_2CrSnS_4) which we are investigating in this study, as the replacement of Zn in the quaternary compound (Cu_2ZnSnS_4) with near transition elements (e.g., Cr, Ni, Mn, Fe, Co, Fe, Mn) presents defects which are similar to (Cu_2ZnSnS_4) because their ionic radii vary slightly and thus no significant change in the crystal structure [11,12]. Table (1) depicts the XRD results of the (112) plane.

The inter-planar distance (d) was estimated by using Bragg formula [13]:

$$m\lambda = 2dsin\theta, \qquad (1)$$

where m is the diffraction order, ѳ is the angle of Bragg, and λ is the x-ray wavelength.
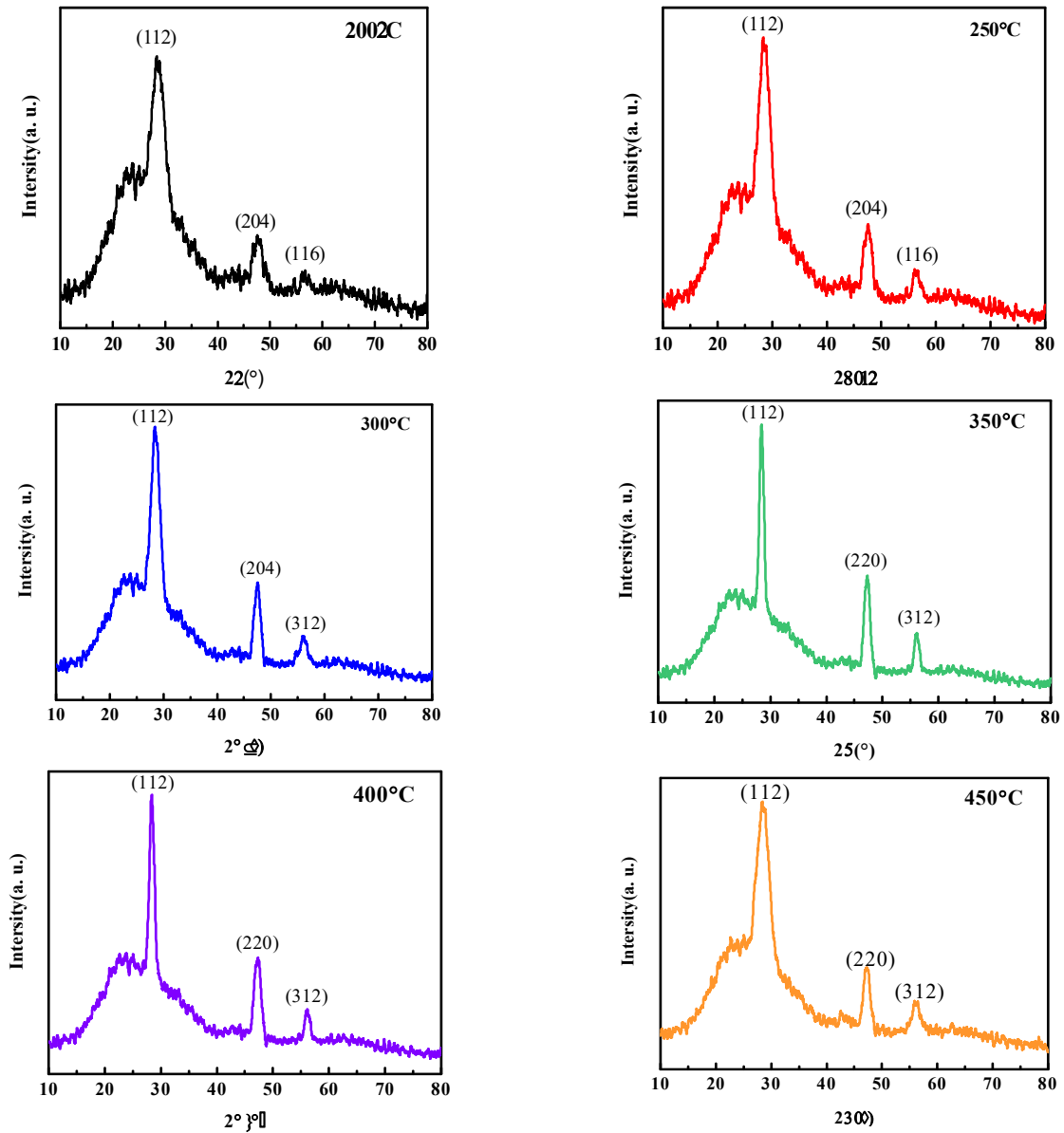
Figure 1. XRD patterns of CCTS samples at various temperatures.

Table 1. XRD results of CCTS films deposited at various temperatures

Deposition Temperature (°C)	2Θ (°)	Inter-planar distance (Å)	Crystallite size (nm)	Texture coefficient
200	28.52	3.127	2.712	0.55
250	28.5	3.129	3.061	3.48
300	28.44	3.135	4.123	0.64
350	28.42	3.137	8.518	0.51
400	28.38	3.142	8.102	0.54
450	28.42	3.137	3.093	0.58

The lattice parameters are calculated through the well-known formula [8]:

$$\frac{1}{d^2} = \frac{h^2+k^2}{a^2} + \frac{\ell^2}{c^2}, \tag{2}$$

where (*h, k, l*) represent indices of Miller; and the tetragonal unit cell parameters are represented by a and c.

The estimated values of a and c are a = 5.445 Å and c = 10.755 Å very near to the ideal ones a = 5.449 Å and c = 10.75 Å. The crystallite size (D) is estimated using the specifications of the peak corresponding to the (112) plane by Scherrer's equation [14]:

$$D = \frac{K\lambda}{\beta \cos\theta}, \tag{3}$$

where k = 0.9 and β is (FWHM) in radians.

The estimated values of (D) are shown in Table 1 which shows that when the temperature increases, the values of (D) increase up to 350 °C and then start to decrease.

This is owing to the high evaporation of the sprayed drops once this temperature has been reached, that is larger than that required to produce maximal pyrolysis and crystallization of the films, due to the high thermal energy. Thus, the crystallization mechanism is not complete [15]. Texture coefficient (Tc) is evaluated by the equation below [14]:

$$T_C = \frac{I_{(h\kappa\ell)}/I_{\circ(h\kappa\ell)}}{N^{-1}\sum_N I_{(h\kappa\ell)}/I_{\circ(h\kappa\ell)}} \quad , \tag{4}$$

where N stands for the number of peaks visible in XRD patterns, $I_{(hkl)}$ is the experimental relative intensity and $I_{\circ(h\kappa\ell)}$ is the ideal intensity.

T$_c$ values for the prevailing direction of growth are listed in Table 1. T$_c$ less than 1 values indicate that all films are polycrystalline. X-ray diffraction could be used to classify the materials phase, but it was difficult to distinguish between them because of how similar their compositions are. So, Raman spectroscopy at room temperature was performed and its results are plotted Figure 2 and Table 2 where the measured spectrum is plotted in black color, the green color represents the peaks resulting from the analysis of the measured spectra, and the sum of these peaks appears in red color representing the calculated spectrum, which is highly consistent with the measured black color.
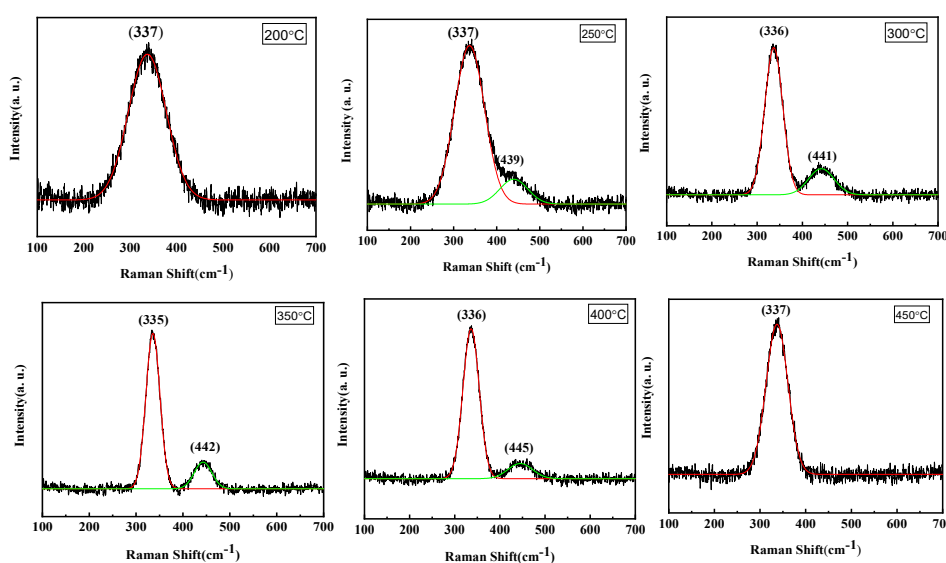
Figure 2. Micro-Raman shift of CCTS samples at various temperatures

Table 2. Result of micro-Raman spectra analysis of CCTS prepared in the current study

Temperature (°C)	Center of peak (cm^{-1})	Width of peak (cm^{-1})	Intensity (arb. u.)
200	337	81.574	4.989
250	337	69.424	6.007
	439	65.323	0.942
300	336	39.829	7.054
	441	56.592	1.252
350	335	29.986	7. 987
	442	37.444	1.369
400	336	36.020	7.500
	445	54.428	0.759
450	337	47.999	7.029

Due to sulfur atoms vibrations in the CCTS structure, the prominent peaks of great intensity at the positions (335, 336, and 337 cm^{-1}) could be seen. This is consistent with the findings of other published investigations [16-18]. Other observed lower intensity peaks can be observed at (439, 441, 442, 445 cm^{-1}) which are consistent with the results of Yan et al. [18]. The surface topography of the films was imaged by FESEM. Figure 3 shows the micro-images at magnification of 50 Kx of the prepared CCTS films. At temperature (200, 250°C), an irregular formation process appears with voids and cracks on the surface, and ball-like shapes begin to stick and align, with some temperature increasing, at (300°C) we notice irregular distribution of nano-paper-like shapes with cracks and hole, and this indicates the formation of a new layer that starts to appear more on the surface and the emergence of a series of small particles in some areas that start to disappear when the substrate temperature increases. At 350, 400, and 450 °C substrate temperatures, we notice

cauliflower-like shapes having polyhedral forms, irregular distribution, and uneven growth, including some cracks and voids caused by crystal flaws, as well as secondary growth on the surface. This can be explained by the development of a new layer before the growth of the prior layer is finished. The granular borders may be seen clearly [13, 19-21]. If it is noticed that the average particle size is large in the sample (CCTS), then it begins to decrease and rise as a result of the temperature difference.
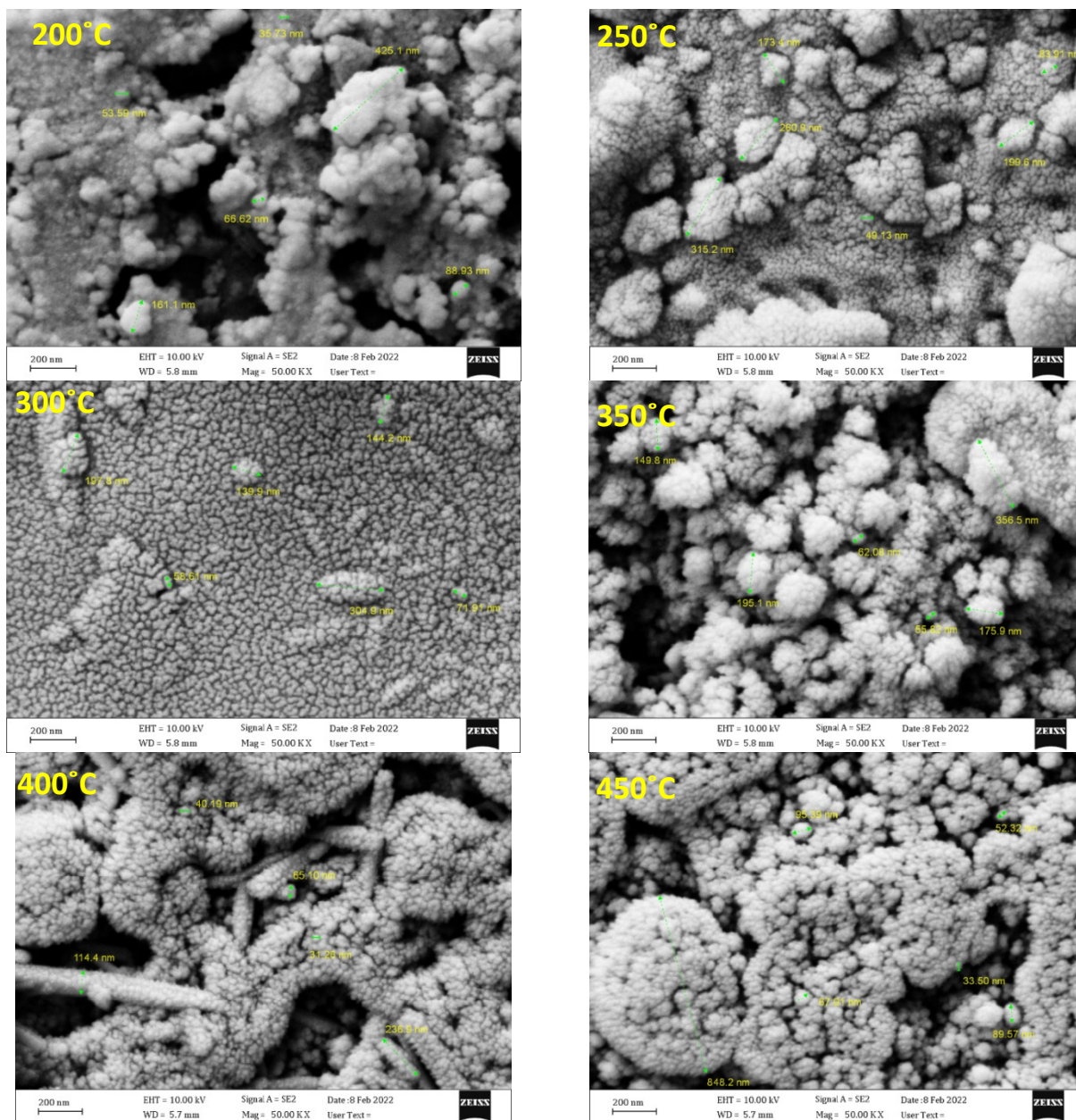
Figure 3. FESEM micro-images of CCTS samples deposited at different temperatures

The optical characteristics of the CCTS films were examined through the absorbance (A) of UV-visible spectra. The absorption coefficient (α) of any film of thickness (t) could be calculated using the following relationship [22]:

$$\alpha = 2.303 \, A/t, \tag{5}$$

The values of α were found to be greater than 10^4 cm^{-1}. Using Tauc's formula, the optical band gap, Eg, could be evaluated from the absorption spectra [23]:

$$(\alpha E) = P(E - Eg)^r, \tag{6}$$

where *P* is constant, *E* stands for photon energy, while *r* is an empirical quantity that describes the electronic transition type which is equal to ½ for direct allowed transition.

In this study, a straight line was generated by sketching a plot between $(\alpha E)^2$ and (E). The direct bandgap could then be estimated by extrapolating this straight line to $(\alpha h\upsilon)^2 = 0$, as shown in Figure 4. The estimated values of Eg were in

the range of 1.69-1.95 eV. This matches well with the findings of other reports [24, 25]. Because of the unsaturated bonds and/or micro-stress generated during the growth which leads to local states of high density, there may be a variance in the energy gap value [7].

In order to define the electrical characteristics of the CCTS films, the Hall Effect was carried out to ascertain the type, concentration, mobility, and conductivity of majority charge carriers. The results of this test are shown in Table 3, which shows positive values of R_H (p-type) consistent with the findings of earlier investigations [4].
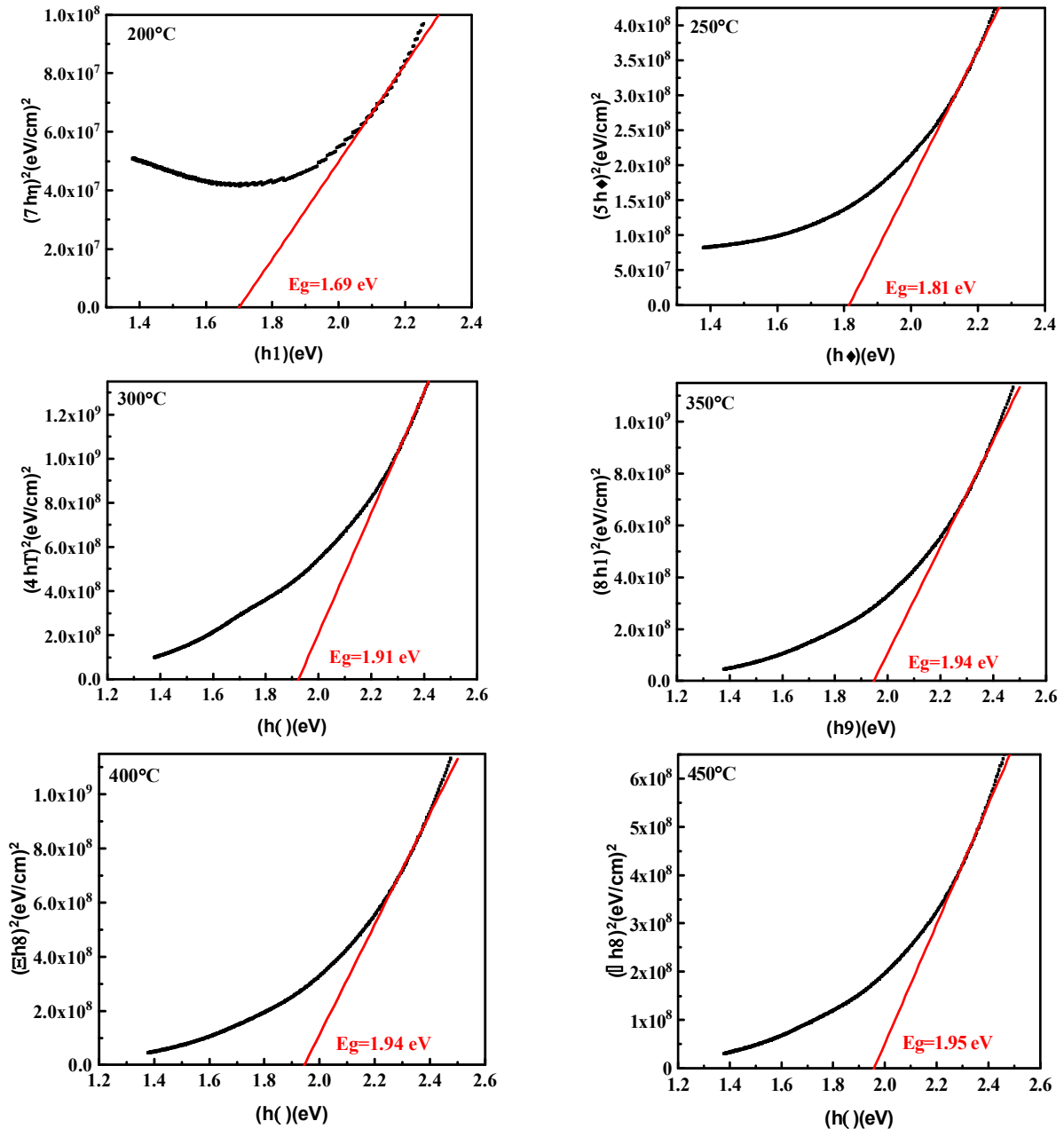
Figure 4. Energy gap of CCTS films prepared at different temperatures

Table 3. Outcomes of Hall Effect test of CCTS samples

Temperature (°C)	Hall coef. (cm³/C)	Concentration (cm⁻³) ×10¹⁷	Mobility (cm²/V.s)	Resistivity (Ω.cm)	Conductivity (Ω.cm)⁻¹
200	15.19	4.11	3.026	5.019	0.199
250	11.96	5.22	4.551	2.627	0.380
300	8.53	7.32	5.213	1.636	0.611
350	6.75	9.25	6.011	1.123	0.890
400	7.79	8.01	5.337	1.46	0.685
450	10.32	6.05	4.002	2.578	0.387

The electrical conductivity, mobility, and concentration of charge carriers have increasing trend as the deposition temperature is increased upto 350 °C, and then they began to decline, as shown in Figures 5 and 6. The results of XRD analysis support this [17].
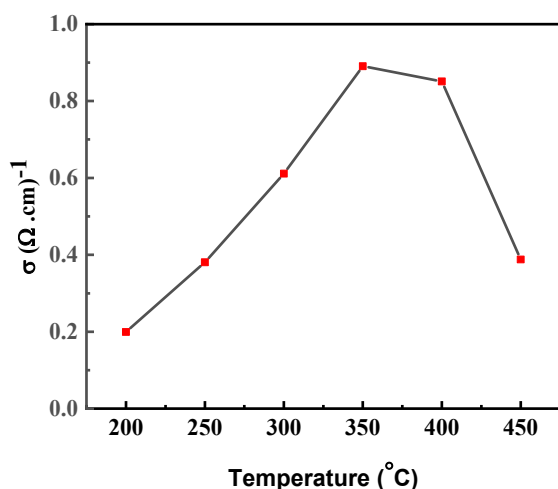
Figure 5. Hall conductivity of CCTS films at various temperatures
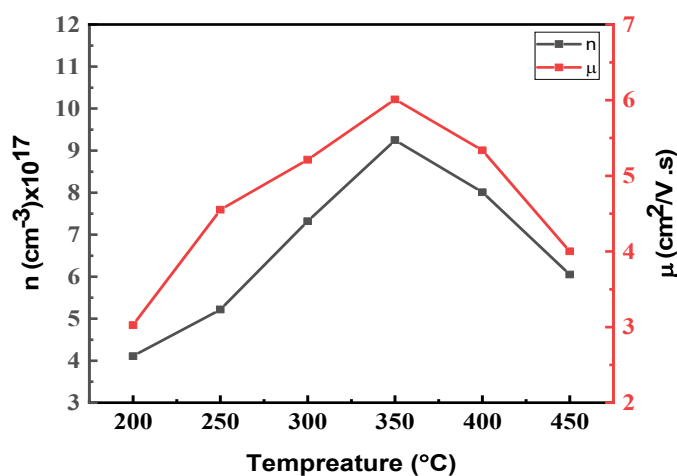
Figure 6. Charge carriers and their mobility of CCTS films at various temperatures

CONCLUSIONS

According to XRD observations, the CCTS films were found to be tetragonal polycrystalline having favorable growth direction of (112). The quaternary CCTS compound's high and distinct peaks at (335, 336, and 337 cm^{-1}) were revealed by Raman spectroscopy, supporting the XRD findings. Different grain sizes and shapes could be seen in the micro-images obtained by FESEM. Electrical measurements of the Hall Effect show that the conductivity was p-type. The band gap range (1.69-1.95 eV) as well as the coefficient of optical absorption (10^4 cm^{-1}) are extremely near to the optimal material values employed in the absorbent layer in solar cells.

ORCID IDs

Ⓓ**Huda Talib,** https://orcid.org/0000-0001-6285-9978; Ⓓ**Nabeel A. Bakr,** https://orcid.org/0000-0002-8819-5847;
Ⓓ**Mohammed A. Abed,** https://orcid.org/0000-0001-5091-0721

REFERENCES

[1] S. Vanalakar, P. Patil, and J. Kim, "Recent advances in synthesis of Cu_2FeSnS_4 materials for solar cell applications: A review", Solar Energy Materials and Solar Cells, **182**, 204-219 (2018). https://doi.org/10.1016/j.solmat.2018.03.021

[2] J. Trajic, M. Romcevic, M. Petrovic, M. Gilic, P. Balaz, A. Zorkovska, and N. Romcevic, "Optical properties of the mechanochemically synthesized Cu_2FeSnS_4 (stannite) nanocrystals: Raman study", Optical Materials, **75**, 314-318 (2018). https://doi.org/10.1016/j.optmat.2017.10.043

[3] M. Cao, C. Li, B. Zhang, J. Huang, L. Wang, and Y. Shen, "PVP assisted solvothermal synthesis of uniform Cu_2FeSnS_4 nanospheres", Journal of Alloys and Compounds, **622**, 695-702 (2015). https://doi.org/10.1016/j.jallcom.2014.10.164

[4] M. Adelifard, "Preparation and characterization of Cu_2FeSnS_4 quaternary semiconductor thin films via the spray pyrolysis technique for photovoltaic applications", Journal of Analytical and Applied Pyrolysis, **122**, 209-215 (2016). https://doi.org/10.1016/j.jaap.2016.09.022

[5] Z.T. Khodair, N.A. Bakr, A. M. Hassan, and A.A. Kamil, "Influence of Substrate temperature and thickness on structural and optical properties of CZTS nanostructures thin films", Journal of Ovonic Research, **15**, 377-385 (2019).

[6] M.A. Abed, N.A. Bakr, and S.B. Mohammed, "Synthesis and Characterization of Chemically Spayed Cu_2FeSnS_4 (CTFS) Thin Films: The Effect of Substrate Temperature", Materials Science Forum, **1039**, 434-441 (2021). https://doi.org/10.4028/www.scientific.net/MSF.1039.434

[7] M.A. Abed, N.A. Bakr, and J. Al-Zanganawee, "Structural, Optical and Electrical Properties of Cu_2NiSnS_4 Thin Films Deposited by Chemical Spray Pyrolysis Method", Chalcogenide Letters, **17**, 179-186 (2020).

[8] S.G. Nilange, N.M. Patil, and A.A. Yadav, "Growth and characterization of spray deposited quaternary Cu_2FeSnS_4 semiconductor thin films.", Physica B: Condensed Matter, **560**, 103-110 (2019). https://doi.org/10.1016/j.physb.2019.02.008

[9] M. Benchikri, O. Zaberca, R. El Ouatib, B. Durand, F. Oftinger, A. Balocchi, and J.Y. Chane-Ching, "A high temperature route to the formation of highly pure quaternary chalcogenide particles", Mater. Lett. **68**, 340–343 (2012). https://doi.org/10.1016/j.matlet.2011.10.105

[10] W. Daranfed, M.S. Aida, A. Hafdallah, and H. Lekiket, "Substrate temperature influence on ZnS thin films prepared by ultrasonic spray", Thin Solid Films, 518, 1082-1084 (2009). https://doi.org/10.1016/j.tsf.2009.03.227

[11] H. Hussein, and A. Yazdani, "Spin-coated Cu_2CrSnS_4 thin film: A potential candidate for thin film solar cells", Materials Science in Semiconductor Processing, **91**, 58-65 (2019). https://doi.org/10.1016/j.mssp.2018.11.005

[12] A. Sharma, P. Sahoo, A. Singha, S. Padhan, G. Udayabhanu, and R. Thangavel, "Efficient visible-light-driven water splitting performance of sulfidation-free, solution processed Cu_2MgSnS_4 thin films: role of post-drying temperature", Solar Energy, **203**, 284-295 (2020). https://doi.org/10.1016/j.solener.2020.04.027

[13] S. Dridi, N. Bitri, and M. Abaab, "Synthesis of quaternary Cu₂NiSnS₄ thin films as a solar energy material prepared through «spray» technique", Materials Letters, **204**, 61–64 (2017). https://doi.org/10.1016/j.matlet.2017.06.028

[14] H.J. Ahmed, A.A. Kamil, A.A. Habeeb, and N.A. Bakr, "The influence of Deposition Temperature on the Properties of Chemically Sprayed Nanostructured Cu₂CdSnS₄ Thin Films", International Research Journal of Science and Technology, **1**, 149-155 (2020). https://doi.org/10.46378/irjst.2020.010211

[15] D. Fikri, A. Yuwono, N. Sofyan, T. Arini, and L. Lalasari, "The effect of substrate heating temperature upon spray pyrolysis process on the morphological and functional properties of fluorine tin oxide conducting glass", AIP Conference Proceedings, **1826**, 1–9 (2017). https://doi.org/10.1063/1.4979219

[16] R.R. Prabhakar, N.H. Loc, M.H. Kumar, P.P. Boix, S. Juan, R.A. John, S.K. Batabyal, and L.H. Wong, "Facile water-based spray pyrolysis of earth-abundant Cu₂FeSnS₄ thin films as an efficient counter electrode in dye-sensitized solar cells", ACS applied materials & interfaces, **20**, 17661–17667 (2014). https://doi.org/10.1021/am503888v

[17] C. Dong, G.Y. Ashebir, J. Qi, J. Chen, Z. Wana, W. Chen, and M. Wang, "Solution-processed Cu₂FeSnS₄ thin films for photovoltaic application", Materials Letters, **214**, 287-289 (2018). https://doi.org/10.1016/j.matlet.2017.12.032

[18] C. Yan, C. Huang, J. Yang, F. Liu, J. Liu, Y. Lai, J. Lib, and Y. Liua, "Synthesis and characterizations of quaternary Cu₂FeSnS₄ nanocrystals", Chemical Communications, **20**, 2603-2605 (2012). https://doi.org/10.1039/C2CC16972J

[19] J. M. Pawlikowski, "Preparation and characterization of close-spaced vapour transport thin films of ZnSe for heterojunction solar cells", Thin Solid Films, **127**, 9-28 (1985). https://doi.org/10.1016/0040-6090(85)90209-3

[20] W.H. Koschel, F. Sorger, and J. Baars, "Optical phonons in I-III-VI₂ compounds", Le Journal De Physique Colloques, **36**, C3-177-C3-181 (1975). https://doi.org/10.1051/jphyscol:1975332

[21] P.S. Maldar, M.A. Gaikwad, A.A. Mane, S.S. Nikam, S.P. Desai, S.D. Giri, A. Sarkar, and A.V. Moholkar, "Fabrication of Cu₂CoSnS₄ thin films by a facile spray pyrolysis for photovoltaic application." Solar Energy, **158**, 89-99 (2017). https://doi.org/10.1016/j.solener.2017.09.036

[22] N.A. Bakr, Z.T. Khodair, and H.I. Mahdi, "Influence of Thiourea Concentration on Some Physical Properties of Chemically Sprayed Cu₂ZnSnS₄ Thin Films", International Journal of Materials Science and Applications, **5**, 261-270 (2016). https://doi.org/10.11648/j.ijmsa.20160506.15

[23] S.A. Hameed, N.A. Bakr, A.M. Hassan, and A.N. Jasim, "Structural and optical properties of Cu₂ZnSnS₄ thin films fabricated by chemical spray pyrolysis", AIP Conference Proceedings. **2213**, 10.1063-5.0000316 (2020). https://doi.org/10.1063/5.0000310

[24] A. Ghosh, A. Biswas, R. Thangavel, and G. Udayabhanu, "Photo-electrochemical properties and electronic band structure of kesterite copper chalcogenide Cu₂–II–Sn–S₄ (II = Fe, Co, Ni) thin films", RSC Advances, **6**, 96025-96034 (2016). https://doi.org/10.1039/C6RA15700A

[25] S. Lee, J. Kim, H. Woo, Y. Jo, A. Inamdar, S. Pawar, H. Kim, W. Jung, and H. Im, "Structural, morphological, compositional, and optical properties of single step electrodeposited Cu₂ZnSnS₄ (CZTS) thin films for solar cell application", Current Applied Physics, **14**, 254-258 (2014). https://doi.org/10.1016/j.cap.2013.11.028

**ОТРИМАННЯ ТА ХАРАКТЕРИСТИКА ТОНКИХ ПЛІВОК CU₂CrSnS₄,
НАНЕСЕНИХ ПРИ РІЗНИХ ТЕМПЕРАТУРАХ**
Худа Таліб[a,b], Набіл А. Бакр[a], Мохаммед А. Абед[b]
[a]Факультет фізики, Науковий коледж, Університет Діяла, Діяла, Ірак
[b]Головне управління освіти Діяла, Діяла, Ірак

У цьому дослідженні тонкі плівки Cu₂CrSnS₄ отримані за допомогою техніки хімічного піролізу при різних температурах осадження (200, 250, 300, 350, 400 і 450°С) і без будь-якого процесу відпалювання. Структурні характеристики плівок були вивчені за допомогою дифракції рентгенівських променів (XRD), мікро-Раманівської спектроскопії та польово-емісійного сканучого електронного мікроскопа (FESEM), тоді як оптичні характеристики досліджені за допомогою УФ-видимої спектрофотометрії, а також описані електричні властивості за допомогою тесту на ефект Холла. Результати XRD для плівок Cu₂CrSnS₄ (CCTS) показали тетрагональну кристалічну структуру станнітної фази з переважною орієнтацією (112). Результати раманівської спектроскопії підготовлених тонких плівок CCTS показали чіткий пік при ~ 336 см⁻¹. Крім того, результати морфології та наскрізні (FESEM) зображення поверхні тонких плівок показали різні форми та форми з різним розміром зерен у діапазоні від 40 до 294 нм. Оптичне дослідження ультрафіолетового та видимого спектру показало оптичний енергетичний проміжок (1,69-1,59 еВ), який вважається придатним для застосування в тонкоплівкових сонячних елементах. Електричні вимірювання за допомогою тесту на ефект Холла показали, що плівки мають носії заряду (p-типу). З аналізу результатів оптимізована температура підготовлених (CCTS) зразків становила 350ºС.
Ключові слова: Cu₂CrSnS₄, розпилювальний піроліз, температура осадження, рентгеноструктурний аналіз, УФ-видима спектроскопія, ефект Холла

EFFECT OF SOLVENT POLARITY ON THE ABSORPTION AND FLUORESCENCE SPECTRA OF NICOTINAMIDE: DETERMINATION OF GROUND AND EXCITED STATE DIPOLE MOMENTS†

Ataklti Abraha Gebreyohanes[a]*, Abebe Belay[b], Getachew Alemu[a]
aDepartment of Physics, Samara University, P. O. Box 132, Samara, Ethiopia
bApplied Physics Program, Adama Science and Technology University, P. O. Box 1888, Adama, Ethiopia
Correspondence Author: atklt.physics@gmail.com
Received September 12, 2022; revised October 8, 2022; accepted November 3, 2022

Nicotinamide (NIC) is an amide-form vitamin with a carboxamide group at b positions that is involved in a variety of biological activities. The drugs contain functional groups which control the type and degree of interaction with different solvents. In this research, the ground and excited state dipole moments of nicotinamide (NIC) were estimated using solvatochromic effects and computational work. A general overview of solvent effects on the electronic absorption and fluorescence spectra of NIC is presented. In both spectra, pronounced solvatochromic effects were observed, and the shift of emission peaks was larger than the corresponding absorption spectra. The experimental ground state $\left(\mu_g\right)$ and excited state $\left(\mu_e\right)$ dipole moments of NIC are estimated from solvatochromic shifts of absorption and fluorescence spectra. The differences between the excited and ground state dipole moments determined by all the methods are quite similar. The HOMO-LUMO energy band gaps were calculated and found to be 5.566 eV. The excited state dipole moment is found to be higher than those of the ground state for all of the used methods, and it is attributed to the more polar excited state of NIC. Finally, the observed spectral properties, measured values of dipole moments, and electronic structures of NIC in different solvents provide important details about charge distribution and solute-solvent interactions that may be helpful in the investigation of these molecules in biological systems.
Keywords: Solvatochromic shift method, Ground state dipole moments, Excited state dipole moments, Nicotinamide
PACS: 33

Introduction

Vitamins are very important organic chemical compounds as a vital nutrient to sustain life due to their important role in normal metabolism processes, growth, and vitality [1]. Nicotinamide (3-pyridine-carboxamide, Vitamin B3) is a water-soluble pyridine derivative and amide form vitamin with a carboxamide group at position b that is involved in many biological activities [2-9]. It helps with diabetes treatment and prevention [6], skin appearance [10–12], energy metabolism, fatty acid synthesis, growth and development, signal transduction, and genome integrity [4,5,8]. Besides, it serves as an important functional group of coenzymes for NAD+ and NADP+ [13,14], which are involved in various chemical reactions including the production of energy in all types of cells [15,16], exhibit antioxidant, anti-inflammatory, and anticarcinogenic activities [2,7], and cytoprotective effects on neural and vascular tissues [17,18]. It is also applicable to different dietary foods, nutritional ingredients, and cosmetics [3].

The absorption and emission spectra of organic molecules are usually modified in solvation processes where the photon of light causes a redistribution of charges, leading to conformational changes in the excited state. The conformational changes induced by solvents in the electronic spectra of molecules can offer information on the local electric field acting on the spectrally active molecule. Thus, the exited dipole moment of an electronically excited molecule is an important property for providing information on the electronic and geometrical structure of the molecules [19,20], in designing non-linear materials [21] and new molecules, selecting best performance in analysis of specific applications, providing information about the nature of the excited states [22–24], determining emission energy as a function of the solvent polarity [22,23], and in parametrisation in quantum chemical procedures for these states [19]. The determination of the singlet excited-state dipole moment is based on the spectral shift caused either externally by electrochromism or internally by solvatochromism. The electrooptic methods (electrochromism) [25,26] are generally considered to be very accurate, but due to their limited use and restricted to relatively very simple molecules, the solvatochromic method is more preferable. The solvatochromic method is simpler and widely accepted [27–33]. It is based on a linear correlation between absorption and fluorescence maxima in different solvent polarity functions.

Several workers have conducted extensive experimental and theoretical studies on ground state and excited-state dipole moments using different techniques in a variety of organic fluorescent compounds [19,22,34-39]. In the present work, the ground and excited state dipole moments of NIC by the solvent perturbation method [28,30] have been determined from solvatochromic shifts using experimental and computational methods. However, there are no reports available in the literature on the determination of the dipole moment value of the compound investigated. Dipole moments

were estimated using Bakhshiev's [27], Kawaski–Chamma–Viallet [28–30] and Lippert–Mataga [31,32] equations and the quantum chemical method.

METHODS AND MATERIALS
Experimental details
Nicotinamide (NIC, Fig. 1) was purchased from Sigma-Aldrich Company and used for measurement without further purification. All the solvents were of spectroscopic grade and purchased from the Sigma-Aldrich Company.

Figure 1. Chemical structure of NIC

Electronic absorption spectra of the compounds were recorded using a Perkin-Elmer Lambda 19 UV-Vis spectrophotometry with double monocromator using a 1-cm path length quartz cuvette. The absorption spectra were recorded in the wavelength regions 200-500 nm, with a spectral band width of 0.1 nm and a scanning speed of 600 nm/min. The steady-state fluorescence spectra were recorded by Fluoromax-4 spectrophotometer (Horiba). The emission spectra were recorded by exciting the sample at its longest absorption maximum. The absorption and emission measurements were performed at room temperature, keeping the concentration of the molecule very low for the fluorescence spectra measurement. The solvent polarity functions were calculated from the relative permittivity and refractive index of the solvents, and the values are shown in Table 1.

Table 1. Solvent functions $f(\varepsilon_r, n)$, $\phi(\varepsilon_r, n)$, F_{L-M}, F_{K-C-V} and F_B, used in the Bakhshiev, Kawski–Chamma–Viallet, Lippert-Mataga and Reichardt equations, respectively

Solvent	ε^a	n^a	f^b	ϕ^b	$F_{L-M}{}^c$	$F_{K-C-V}{}^d$	$F_B{}^e$
Water	80.10	1.3325	0.91375	0.2265	0.32028	0.683392	0.913758
Ethanol	24.55	1.3614	0.81293	0.2459	0.28874	0.652459	0.812933
Acetonitrile	37.50	1.3404	0.86408	0.2318	0.30682	0.663891	0.864083
Butanol	17.84	1.399	0.75370	0.2711	0.26433	0.647996	0.753704
Methanol	33	1.328	0.85573	0.2234	0.30894	0.651335	0.855732

^{a} ε = relative permittivity and n=refractive index.

^{b} Bilot-Kawski solvent functions in Eqns. (3&4)

^{c} Lippert-Mataga solvent function in Eqn. (17).

^{d} Kawski-Chamma-Viallet solvent function in Eqn. (18)

^{e} Bakhshiev solvent function in Eqn. (19).

THEORETICAL BACKGROUND
Bilot–Kawski method
Based on Onsager's reaction field theory, which assumes a spherical structure of the molecules within a cavity radius 'a' and employing the simplest quantum mechanical second order perturbation theory of absorption ($\tilde{v}_a$) and fluorescence ($\tilde{v}_f$) band shifts in various solvents of different relative permittivity (ε_r) and refractive index (n), the equations for the dipole moments were calculated [28,31,32,40-46]. According to Bilot and Kawski [28,41], the equations related to the difference and sum of wavenumbers of absorption and fluorescence are expressed as Eqns. (1 &2).

$$\tilde{v}_a - \tilde{v}_f = m_1 f(\varepsilon_r, n) + \text{constant},$$ (1)

$$\tilde{v}_a + \tilde{v}_f = -m_2 \phi(\varepsilon_r, n) + \text{constant},$$ (2)

where the solvent polarity parameters $f(\varepsilon_r, n)$, and $\phi(\varepsilon_r, n) = f(\varepsilon_r, n) + 2g(n)$ [40,43,47] are expressed as Eqns. (3 & 4), respectively.

$$f(\varepsilon_r, n) = \frac{2n^2 + 1}{n^2 + 2}\left(\frac{\varepsilon_r - 1}{\varepsilon_r + 2} - \frac{n^2 - 1}{n^2 + 2}\right),$$ (3)

$$g(n) = \frac{3}{2}\left(\frac{n^4 - 1}{(n^2 + 2)^2}\right).$$ (4)

The parameters m_1 and m_2 which can be determined from the slope of the straight line of Eqns. (1&2) are given by:

$$m_1 = \frac{2(\mu_e - \mu_g)^2}{hca^3}, \tag{5}$$

$$m_2 = \frac{2(\mu_e^2 - \mu_g^2)}{hca^3}, \tag{6}$$

where h and c are the plank's constant and the velocity of light in vacuum respectively; $a = (3M / 4\pi\delta N)^{1/3}$ with the relative molecular mass of the solute molecules (M), the density (δ) and Avogadro's number (N).

Assuming the symmetry of the solute molecule remains unchanged upon electronic transition and the dipole moment states are parallel, the values of the ground and excited dipole moments from Eqns. (5&6) can be obtained as [40,43,47],

$$\mu_g = \frac{|m_2 - m_1|}{2}\left(\frac{hca^3}{2m_1}\right)^{1/2}, \tag{7}$$

$$\mu_e = \frac{|m_2 + m_1|}{2}\left(\frac{hca^3}{2m_1}\right)^{1/2}, \tag{8}$$

$$\frac{\mu_e}{\mu_g} = \frac{|m_2 + m_1|}{|m_2 - m_1|} \qquad \text{for } m_2 > m_1. \tag{9}$$

Moreover, if the ground state and excited state dipole moments are not parallel to each other, the angle between the two dipole moments can be determined [42] as

$$\cos\theta = \frac{1}{2\mu_g\mu_e}\left[\left(\mu_g^2 + \mu_e^2\right) - \frac{m_1}{m_2}\left(\mu_e^2 - \mu_g^2\right)\right]. \tag{10}$$

Lippert–Mataga, Kawski–Chamma–Viallet and Bakhshiev methods

The electric dipole moment of a polar solute polarizes the solvent so that the solute itself experiences an electric field, the reaction field, which is proportional to the solute dipole moment in the ground and excited states. Such proportionalities for the difference and sum of absorption and fluorescence maxima maximum wavenumber have been defined by the following independent equations [30-32,48] used for the estimation of ground and excited state dipole moments:

$$\tilde{v}_a - \tilde{v}_f = m_3 F_{L-M}(\varepsilon_r, n) + \text{constant}, \tag{11}$$

$$\frac{\tilde{v}_a + \tilde{v}_f}{2} = -m_4 F_{K-C-V}(\varepsilon_r, n) + \text{constant}, \tag{12}$$

$$\tilde{v}_a - \tilde{v}_f = m_5 F_B(\varepsilon_r, n) + \text{constant}, \tag{13}$$

m_3, m_4 and m_5 are the slopes of the linear relationships corresponding to Eqns. (11-13), are given by;

$$m_3 = \frac{2(\mu_e - \mu_g)^2}{hca^3} \tag{14}$$

$$m_4 = \frac{2(\mu_e^2 - \mu_g^2)}{hca^3} \tag{15}$$

$$m_5 = \frac{2(\mu_e - \mu_g)^2}{hca^3} \tag{16}$$

F_{L-M} [31,32], F_{K-C-V} [30] and F_B [48] are solvent polarity functions corresponding to Lippert–Mataga, Kawski–Chamma–Viallet and Bakhshiev methods and are given as:

$$F_{L-M}(\varepsilon_r, n) = \left(\frac{\varepsilon_r - 1}{2\varepsilon_r + 1} - \frac{n^2 - 1}{2n^2 + 1}\right) \tag{17}$$

$$F_{K-C-V}(\varepsilon_r, n) = \frac{2n^2+1}{2(n^2+2)}\left(\frac{\varepsilon_r-1}{\varepsilon_r+2} - \frac{n^2-1}{n^2+2}\right) + \frac{3(n^4-1)}{2(n^2+2)^2} \tag{18}$$

$$F_B(\varepsilon_r, n) = \frac{2n^2+1}{n^2+2}\left(\frac{\varepsilon_r-1}{\varepsilon_r+2} - \frac{n^2-1}{n^2+2}\right) \tag{19}$$

Computational Methods

The ground state dipole moment ($\vec{\mu}_g$) of the three compounds was theoretically calculated using the Gaussian 09 program and analysed with the help of Gauss View software [49]. The calculations and ground state geometries optimization were performed at a density functional theory (DFT) level of theory by employing Becke's three parameter (local, non-local, Hartee-Fock) hybrid exchange functional (B3LYP) and the basis set 6–311G(d,p).

RESULTS AND DISCUSSION

Determination of the photophysical and photochemistry of different drug compounds is useful for various applications. The values of ground- and excited-state dipole moments of the molecules provide information about the change in electronic distribution of the excited molecule [22,23]. It elucidates the nature of the excited state of the molecules as it reflects the charge distribution in the molecule [22,23,50]. Furthermore, the experimental data on dipole moment can be used to parameterize quantum chemical procedures for these states [19]. The excited dipole moments of the fluorescent molecules have also been used to determine emission energy as a function of the solvent polarity function [22,23].

Solvent effects on UV-Vis absorption and fluorescence spectra of Nicotinamide

The absorption and fluorescence emission spectra of NIC were recorded in solvents of different solvent parameters with the corresponding solvent polarity values as in Table 1. Figs. 2&3 shows the typical absorption and fluorescence spectra of NIC obtained in different solvents. The UV-Vis absorption spectra of NIC are characterized by their maximum absorption band, which corresponds to HOMO → LUMO mainly due to $\pi \to \pi^*$ orbital transition. And, the fluorescence spectra of NIC undergoes an average of a red shift as it increasing in solvent polarity. Fig. 2 shows an exchange of order in water and acetonitrile, and in methanol and ethanol as solvent polarity increases, most possibly due to the influence of an intermolecular association and/or solute-solvent interactions.
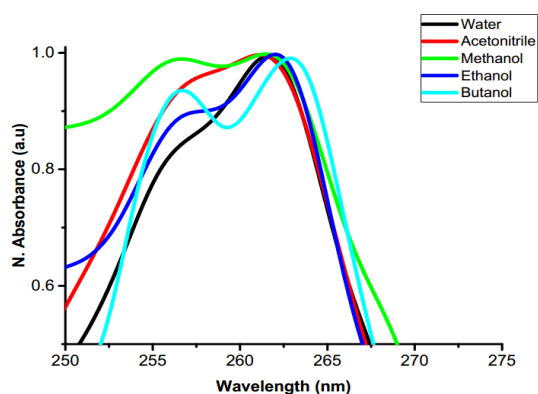
Figure 2. Absorbance spectra of NIC in different solvents
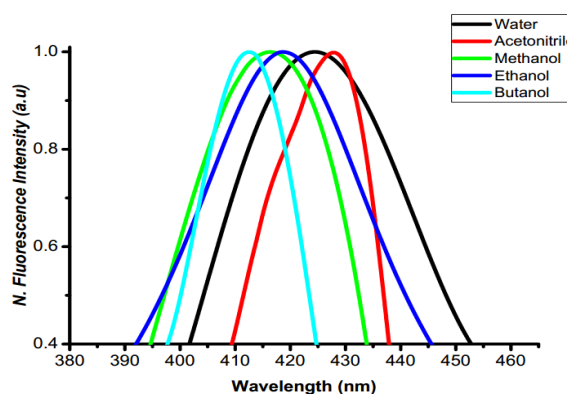
Figure 3. Florescence spectra of NIC in different solvents

As compared to the absorption spectra, a large spectral shift was observed in the emission spectra as shown in Table 2. The lesser spectral shifts in the absorption maxima compared with the fluorescence spectra of the compound implies that the ground state energy distribution may not be affected to a greater extent, possibly due to the less polar nature of the compound in the ground state rather than in the excited state.

Table 2. Difference, Sum and mean of Peak absorption and emission spectra of Nicotinamide in different polar solvents

Solvent	$\tilde{v}_a$	$\tilde{v}_f$	$\tilde{v}_a - \tilde{v}_f$	$\tilde{v}_a + \tilde{v}_f$	$(\tilde{v}_a + \tilde{v}_f)/2$
WATER	3822630	2358491	1464139	6181121	3090560
ETHANOL	3816794	2392344	1424449	6209138	3104569
ACETONITRILE	3831418	2336449	1494969	6167866	3083933
BUTANOL	3802281	2427184	1375097	6229466	3114733
METHANOL	3816794	2403846	1412948	6220640	3110320

$\tilde{v}_a$, absorption maximum in cm^{-1}; $\tilde{v}_f$, fluorescence maximum in cm^{-1}

The absorption and fluorescence emission data of NIC in solution also provided reliable information about the solvation effects in the ground and excited states. From Table 2, we observe that the magnitude of Stokes shift for the compound increased with increasing solvent polarity. The large magnitude of the Stokes shift indicates that the excited state geometry of the compound could be different from that of the ground state and that there will also be an increase in dipole moment on excitation. Furthermore, these solvatochromic data can also provide information to identify the possible orbital transition of the compounds, namely $\pi \rightarrow \pi^*$ or $n \rightarrow n^*$ etc. The data reveals that, with an increase in solvent polarity, the electronic emission peak undergoes an average of red shift, confirmed as a $\pi \rightarrow \pi^*$ transition. Generally, the pronounced emission band shifts and increase in Stokes' shift values with an increase in solvent polarity indicate there is an increase in dipole moment on excitation.

Dipole Moments Calculation
To get a further insight into the solvatochromic behaviour of nicotinamide, the spectroscopic properties were correlated with the solvent polarity functions. From the slope of the Bilot-Kawski, Lippert-Mataga, Kawski-Chamma-Viallet and Bakhshiev equations, the ground and excited dipole moments were calculated. Figs. 4&5 shows the Stokes shift and the sum of the wavenumbers versus solvent polarity function for NIC using the Bilot-Kawski equations.
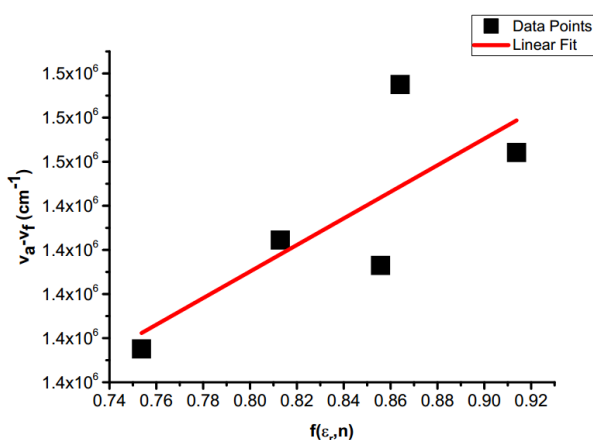
Figure 4. Plot of $\tilde{v}_a - \tilde{v}_f$ versus $f(\varepsilon_r, n)$ of NIC in different polar solvents using Bilot Kawski equation
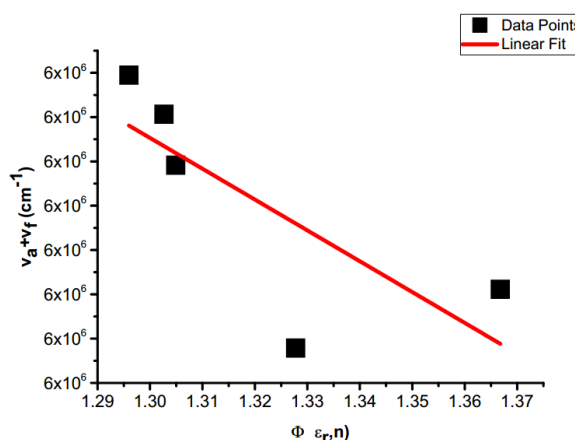
Figure 5. Plot of $\tilde{v}_a + \tilde{v}_f$ versus $\phi(\varepsilon_r, n)$ of NIC in different polar solvents using Bilot Kawski equation

Similarly, Figs. 6&7 are the plots of the Stokes shift and the mean of the wavenumbers versus the solvent polarity for Lippert-Mataga and Kawski-Chamma-Viallet equations respectively. The deviation of the data in Figs. 4, 5, 6 &7 could be from the influence of intermolecular association or solute-solvent interaction [51].
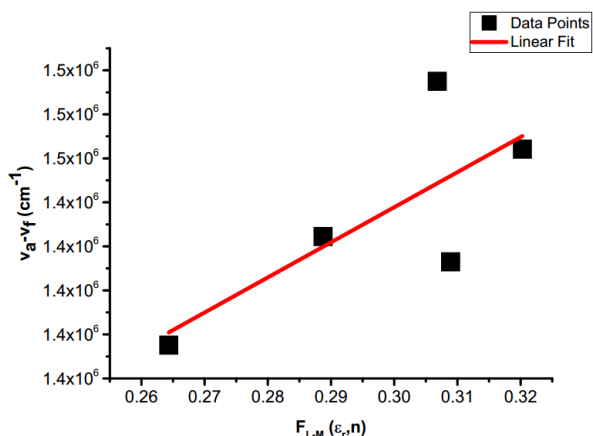
Figure 6. Plot of $\tilde{v}_a - \tilde{v}_f$ versus $F_{L-M}(\varepsilon_r, n)$ of NIC in different polar solvents using Lippert Mataga equation

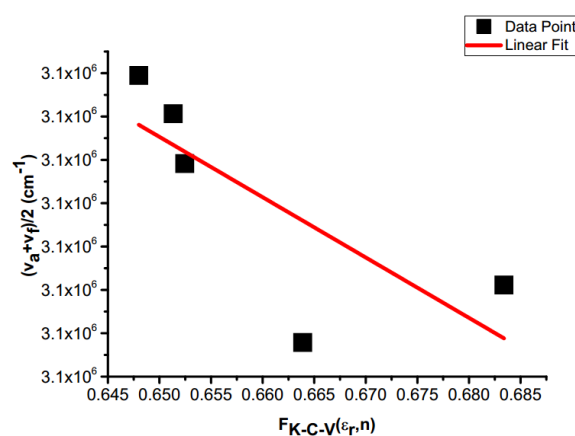**Figure 7.** Plot of $(\tilde{v}_a + \tilde{v}_f)/2$ versus $F_{K-C-V}(\varepsilon_r, n)$ of NIC in different polar solvents using Kawski-Chamma-Viallet equation

From the slopes of the graphs of Figs. 4, 5, 6 & 7, the ground and excited state dipole moments were calculated and the values are as shown in Table 3.

195

Effect of Solvent Polarity on The Absorption and Fluorescence Spectra...

EEJP. 4 (2022)

Table 3. Ground state, excited-state dipole moments in Debye (D), and Onsager cavity radius 'a' ($\overset{\circ}{A}$), calculated by experimental and theoretical methods for Nicotinamide

a^a	μ_g^b	μ_e^c	$\Delta\mu_{B-K}^d$	$\Delta\mu_{L-M}^e$	μ_{gK-C-V}^f	$\Delta\mu_{gB}^g$	μ_g^h	μ_e^{h*}	θ^i	μ_g^j	μ_e^k	μ_s^l
2.258	0.02	0.254	0.234	0.364	0.064	0.216	1.48	1.87	0°	0.315	0.316	0.096

$1D = 3.33564 \times 10^{32} C.cm$

[a] calculated Onsager cavity radius

[b] Ground state dipole moment calculated according to Bilot-Kawski, Eqn. (7)

[c] Excited state dipole moment calculated according to Bilot-Kawski, Eqn. (8).

[d] Change of excited and ground dipole moments using Eqns. (7&8)

[e] Calculated change dipole moment according to Lippert-Mataga correlation, Eqn. (14).

[f] Calculated ground dipole moment according to Kawski-Chamma-Viallet method, Eqns. (15&7).

[g] Calculated change of dipole moment according to Bakhshiev correlation, Eqn. (16).

[h] calculated ground dipole moments from Gaussian 9 using #td b3lyp/6-311++g

[h*] calculated excited dipole moments from Gaussian 9 using #opt b3lyp/6-311++g

[i] Angle between ground and excited dipole moments using Eqn. (10)

[j] The value from reference ([51])

[k] The value from reference ([51])

[l] The value from reference ([51])

The calculated values of the ground and excited state dipole moments using Eqns. (7 &8), are 0.02 and 0.254 D. Due to the different assumptions and simplifications used by each method, the ground and excited state dipole moments that are estimated by different methods are not similar [60]. The change in dipole moments ($\Delta\mu$ =0.364) obtained using Lippert–Mataga Eqn. (14) is larger than the value obtained by other methods. This is due to the fact that the Lippert–Mataga equation neglected the polarizable nature of the solute molecules [55]. It has also been reported previouslythat the change in dipole moment obtained using the Lippert–Mataga equation is larger than the values calculated by other methods [55, 23, 40, 61]. Furthermore, the ground and excited E-nicotinamide results from individual stark lobe measurements were obtained and reported [51], $\mu_g = 0.315$ and $\mu_e = 0.316 D$ using microwave spectrum. Because of the used solvents with different techniques and temperatures, the reported results by [51] are slightly larger than the results of this study using Bilot-Kawski of Eqn. (7&8). Thus, the results of the current study are better than the results previously reported by [51], because of the difference between the ground and excited state dipole moments required for solvatochromism. The results of the ground dipole moment in this study are also similar to the results obtained by [52], 0.0967 D on the surface of nicotinamide by the Helmholtz equation on the basis of surface excess values obtained from surface tension measurements and surface potential changes.

In general, the difference between the excited and ground state dipole moments ($\Delta\mu$) obtained by experimental and theoretical methods is moderately high, indicating that the excited dipole moment is greater than that in the ground state and also more polar than in the ground state.

Quantum Chemical Calculation

Figs. 8 (a-d) shows the HOMO-LUMO structures, the optimized structure with the dipole moment vector, and the total electron density with the electrostatic potential map (TED-ESP) for NIC using TD SCF-DFT-B3LYP-6-311G. It shows the spatial distribution of the electron cloud in three dimensions.

Table 3 shows the dipole moments determined in the gas phase by ab initio calculation using the Gaussian 09 software [49]. The dipole moments calculated by quantum chemical calculations in the gas phase were μ_g=1.48 D and μ_e=1.9D. The theoretical dipole moments are greater than the experimental results. This is because the dipole moments that are based on charge densities obtained from Eigen functions of the molecular orbital approximations are considerably higher than the actual experimental dipole moments [23]. Furthermore, quantum chemistry approaches often produce an exaggerated electron distribution in molecules, making them more polar than they are in reality [23]. Another reason is that experimental methods take into account solvent and environmental influences (solvent-solvent interaction), whereas ab initio calculations only provide results for a free solute molecule in vacuum [53-55].

The other calculated parameters that are very important in quantum chemistry are the HOMO-LUMO energy gaps of the compounds which reflect the chemical activity of the molecules. Both HOMO and LUMO are the main orbitals that take part in chemical stability. A molecule with large HOMO-LUMO gaps is generally stable and unreactive, while ones with small gaps are generally reactive. The HOMO-LUMO band gap for NIC is 0.169 eV. A difference in electronic distribution was also noticed on the HOMO-LUMO molecular orbital plot of NIC as shown in Fig. 8 (a). Higher electronic distribution was observed at the LUMO orbital level, and this also confirms that the excited states of the molecules have higher dipole moments. The obtained results are also similar the the results reported previously [51,52].
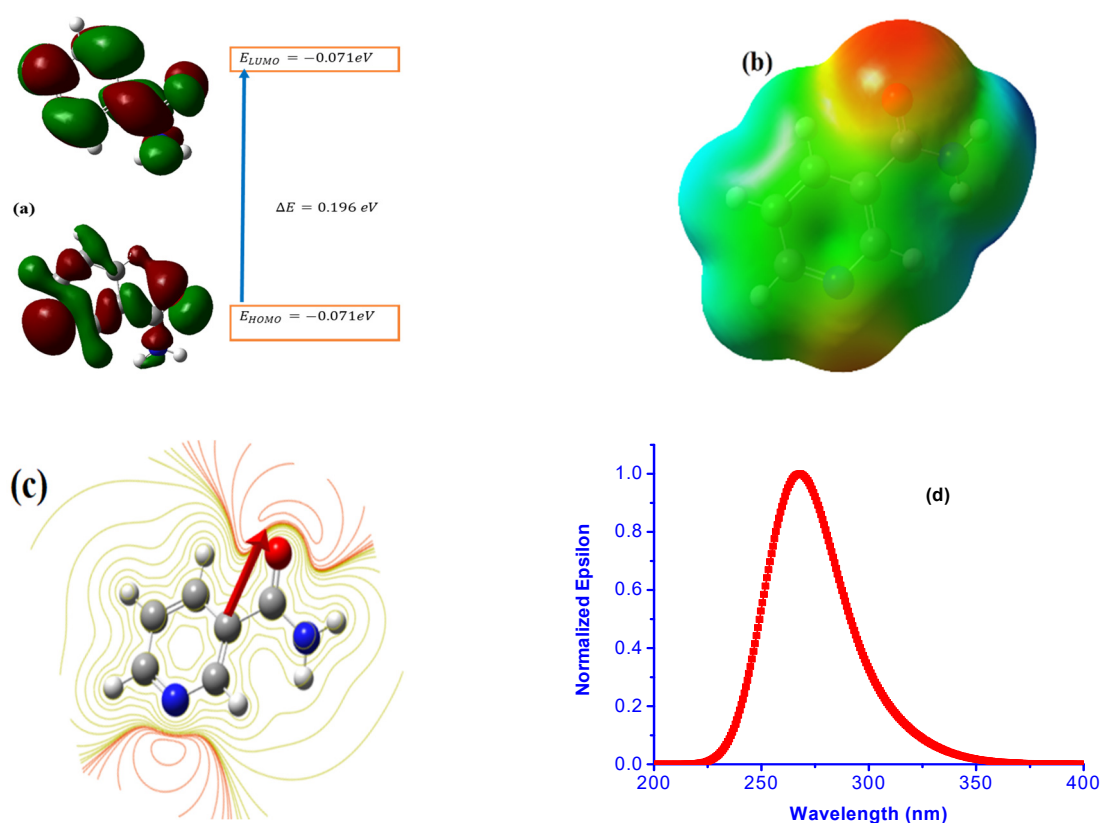
Figure 8. (a) Electron distribution of HOMO and LUMO energy levels; (b) the 3D total electron density with electrostatic potential map (TED-ESP); (c) The 2D electrostatic potential maps around the molecule of NIC and direction of its dipole; (d) Absorbance spectra of NIC with $\lambda_{max} = 268nm$ theoretically using the Density Functional Theory at B3LYP level of theory at 6-311G**

The electrostatic potential map plot of NIC, as illustrated in Figs. 8(b&c), allows the nucleophilic and electrophilic areas of the molecules to be estimated. Identifying these nucleophilic and electrophilic areas is critical for the design of nonlinear optical materials [56] and helps prediction of the site of attack in various photochemical processes [23,55]. The electrostatic potential map of NIC is represented in red and blue colours. The blue colour represents a positive phase that corresponds to a nucleophilic region and the red colour represents a negative phase that corresponds to an electrophilic region [55,57]. Oxygen creates an electron-rich region and the lowest electrostatic potential of the molecule, and nitrogen is relatively electron deficient for NIC molecules. In addition, the UV/Vis absorption spectra in Fig. 8 (d), the excitation energies, and their corresponding oscillator strengths are determined using TD-SCF-DFT-B3LYP-6-311G** since it determines these better than other methods [55,58,59]. The numerical values are shown in Table 4.

Table 4. HOMO-LUMO energy band gap, UV/Vis. absorption wavelengths and corresponding oscillator strengths determined using TDSCF-DFT-B3LYP-6-311G for Nicotinamide

Band Gap (eV)	λ_1(nm)	λ_3(nm)	λ_3(nm)	E_1(eV)	E_2(eV)	E_3(eV)	S_1	S_2	S_3
0.196	300.75	270.99	265.85	4.1225	4.5753	4.6637	0.0006	0.0042	0.0043

E_1: excited state 1 energy and corresponding wavelength, λ_1; oscillator strength, S_1. E_2: excited state 2 energy and corresponding wavelength, λ_2; oscillator strength, S_2. E_3: excited state 3 energy and corresponding wavelength, λ_3 and oscillator strength, S_3.

CONCLUSION

The ground-state and excited-state dipole moments of nicotinamide were investigated by both experimental and theoretical methods. It was observed that the excited state possessed a higher dipole moment than the ground state. This result confirms that the excited states of nicotinamide are more polarized than their ground state and therefore more sensitive to solvent effects. The differences in the ground state and the excited state dipole moments obtained from various equations are due to the different assumptions and simplifications made in the solvatochromic methods. The ground- and excited-state dipole moments obtained by quantum chemical computation (DFT) provided higher results than experimental findings because the results were computed in vacuum rather than using solvents. In addition, a difference in electronic distribution was also noticed on the HOMO-LUMO molecular orbital plots of NIC. In general, the spectral properties observed, the values of dipole moments, and electronic structures of NIC in different solvents provide important information about charge distribution and solute-solvent interactions, which may be useful in the study of these molecules in biological systems.

ORCID IDs

Ataklti Abraha, https://orcid.org/0000-0001-8407-2113

REFERENCES

[1] B. Hassan, "Vitamins (importance and toxicity", Pharmaceut Anal Acta, **3**, e125 (2012). https://doi.org/10.4172/2153-2435.1000e125

[2] J. Kamat, and T. Devasagayam, "Nicotinamide (vitamin B3) as an effective antioxidant against oxidative damage in rat brain mitochondria", Redox Report, **4**(4), 179 (1999). https://doi.org/10.1179/135100099101534882

[3] A.R. Shalita, J.G. Smith, L.C. Parish, M.S. Sofman, and D.K. Chalker, "Topical nicotinamide compared with clindamycin gel in the treatment of inelammatory acne vulgaris", International journal of dermatology, **34**(6), 434 (1995). https://doi.org/10.1111/j.1365-4362.1995.tb04449.x

[4] J.M. Denu, "Vitamin B3 and sirtuin function", Trends in biochemical sciences, **30**(9), 479 (2005). https://doi.org/10.1016/j.tibs.2005.07.004

[5] L.K. Klaidman, S.K. Mukherjee, T.P. Hutchin, and J.D. Adams, "Nicotinamide as a precursor for NAD+ prevents apoptosis in the mouse brain induced by tertiary-butylhydroperoxide", Neuroscience letters, **206**(1), 5 (1996). https://doi.org/10.1016/0304-3940(96)12446-0

[6] R.B. Elliott, C.C. Pilcher, A. Stewart, D. Fergusson, and M.A. McGregor, "The use of nicotinamide in the prevention of type 1 diabetes", Annals of the New York Academy of Sciences, 696, 333 (1993). https://doi.org/10.1111/j.1749-6632.1993.tb17169.x

[7] R.W. Pero, B. Axelsson, D. Siemann, D. Chaplin, and G. Dougherty, in: *ADP-Ribosylation Reactions: From Bacterial Pathogenesis to Cancer*, edited by R. Alvarez-Gonzalez, (Springer, Boston, MA, 1999). pp. 119-125. https://doi.org/10.1007/978-1-4419-8740-2_18

[8] E.L. Jacobson, W.M. Shieh, and A.C. Huang, in *ADP-Ribosylation Reactions: From Bacterial Pathogenesis to Cancer*, edited by R. Alvarez-Gonzalez, (Springer, Boston, MA, 1999). pp. 69-74.

[9] H. Yamamoto, and H. Okamoto, "Protection by picolinamide, a novel inhibitor of poly (ADP-ribose) synthetase, against both streptozotocin-induced depression of proinsulin synthesis and reduction of NAD content in pancreatic islets", Biochemical and biophysical research communications, **95**(1), 474 (1980). https://doi.org/10.1016/0006-291X(80)90762-7

[10] I. Muszalska, K. Kiaszewicz, D. Ksoń, and A. Sobczak, "Determination of nicotinamide (vitamin B3) in cosmetic products using differential spectrophotometry and liquid chromatography (HPLC)", Journal of Analytical Chemistry, **68**(11), 1007 (2013). https://doi.org/10.1134/S1061934813110087

[11] X. Xiao, Y. Hou, J. Du, D. Sun, G. Bai, and G. Luo, Determination of vitamins B2, B3, B6 and B7 in corn steep liquor by NIR and PLSR. Transactions of Tianjin University, **18**(5), 372 (2012). https://doi.org/10.1007/s12209-012-1932-1

[12] J.P. Maksimović, L.Z. Kolar-Anić, S.R. Anić, D.D. Ribić, and N.D. Pejić, "Quantitative determination of some water-soluble B vitamins by kinetic analytical method based on the perturbation of an oscillatory reaction", Journal of the Brazilian Chemical Society, **22**, 38 (2011). https://doi.org/10.1590/S0103-50532011000100005

[13] A. Sikora, P. Szajerski, Ł. Piotrowski, J. Zielonka, J. Adamus, A. Marcinek, and J. Gębicki, "Radical scavenging properties of nicotinamide and its metabolites", Radiation Physics and Chemistry, **77**(3), 259 (2008). https://doi.org/10.1016/j.radphyschem.2007.05.005

[14] P.A. Thibodeau, and B. Paquette, "DNA damage induced by catecholestrogens in the presence of copper (II): generation of reactive oxygen species and enhancement by NADH", Free Radical Biology and Medicine, **27**(11-12), 1367 (1999). https://doi.org/10.1016/S0891-5849(99)00183-5

[15] A.C. Chen, et al, "A phase 3 randomized trial of nicotinamide for skin-cancer chemoprevention", New England journal of medicine, **373**(17), 1618 (2015). https://doi.org/10.1056/NEJMoa1506197

[16] M. Escudero-Góngora, and P. Fernández-Peñas, "Nicotinamide: new indications in dermatology", Actas Dermo-Sifiliograficas (English Edition), **9**(107), 777 (2016). https://doi.org/10.1016/j.adengl.2016.05.024

[17] M. Kumar, S. Jaiswal, R. Singh, G. Srivastav, P. Singh, T.N. Yadav, and R.A. Yadav, "Ab initio studies of molecular structures, conformers and vibrational spectra of heterocyclic organics: I. Nicotinamide and its N-oxide", Spectrochimica Acta Part A: Molecular and Biomolecular Spectroscopy, **75**(1), 281 (2010). https://doi.org/10.1016/j.saa.2009.10.025

[18] S. Chlopick, J. Swies, A. Mogielnicki, W. Buczko, M. Bartus, M. Lomnicka, J. Adamus, and J. Gebicki, "1-Methylnicotinamide (MNA), a primary metabolite of nicotinamide, exerts anti-thrombotic activity mediated by a cyclooxygenase-2/prostacyclin pathway", British journal of pharmacology, **152**(2), 230 (2007). https://doi.org/10.1038%2Fsj.bjp.0707383

[19] U.S. Raikar, C.G. Renuka, Y.F. Nadaf, B.G. Mulimani, A.M. Karguppikar, and M.K. Soudagar, "Solvent effects on the absorption and fluorescence spectra of coumarins 6 and 7 molecules: Determination of ground and excited state dipole moment", Spectrochimica Acta Part A: Molecular and Biomolecular Spectroscopy, **65**(3-4), 673 (2006). https://doi.org/10.1016/j.saa.2005.12.028

[20] V.K. Sharma, P.D. Saharo, N. Sharma, R.C. Rastogi, S.K. Ghoshal, and D. Mohan, "Influence of solvent and substituent on excited state characterstics of laser grade coumarin dyes", Spectrochimica Acta Part A: Molecular and Biomolecular Spectroscopy, **59**(6), 1161 (2003). https://doi.org/10.1016/S1386-1425(02)00296-2

[21] D.S. Chemla, and J. Zyss, editors, *Nonlinear Optical Properties of Organic Molecules and Crystals*, (Academic Press, Orlando, 2012). Vol. 1.

[22] S. Inamdar, Y. Nadaf, and B. Mulimani, "Ground and excited state dipole moments of exalite 404 and exalite 417 UV laser dyes determined from solvatochromic shifts of absorption and fluorescence spectra", Journal of Molecular Structure: THEOCHEM, **624**(1-3), 47 (2003). https://doi.org/10.1016/S0166-1280(02)00734-0

[23] S. Manohara, V.U. Kumar, Shivakumaraiah, and L. Gerward, "Estimation of ground and excited-state dipole moments of 1,2-diazines by solvatochromic method and quantum-chemical calculation", Journal of Molecular Liquids, **181**, 97 (2013). https://doi.org/10.1016/j.molliq.2013.02.018

[24] İ. Sıdır, and Y.G. Sıdır, "Ground state and excited state dipole moments of 6, 8-diphenylimidazo [1, 2-α] pyrazine determined from solvatochromic shifts of absorption and fluorescence spectra", Spectrochimica Acta Part A: Molecular and Biomolecular Spectroscopy, **79**(5), 1220 (2011). https://doi.org/10.1016/j.saa.2011.04.046

[25] W. Liptay, "Dipole Moments and Polarizabilities in Excited Electronic States", Excited States, **1**, 129 (1974). https://doi.org/10.1016/B978-0-12-227201-1.50009-7

[26] J. Czekalla, "Elektrische Fluoreszenzpolarisation: Die Bestimmung von Dipolmomenten angeregter Moleküle aus dem Polarisationsgrad der Fluoreszenz in starken elektrischen Feldern", Zeitschrift für Elektrochemie, Berichte der Bunsengesellschaft für physikalische Chemie, **64**(10), 1221 (1960). https://doi.org/10.1002/bbpc.19600641016

[27] N. Bakhshiev, "Universal intermolecular interactions and their effect on the position of the electronic spectra of molecules in two-component solutions. VII. Theory (general case of an isotropic solution)", Optics and Spectroscopy, **16**, 446 (1964).

[28] V.L. Bilot, and A. Kawski, "Zur theorie des einflusses von Lösungsmitteln auf die elektronenspektren der moleküle", Zeitschrift für Naturforschung A, **17**(7), 621 (1962).

[29] A. Kawski, and P. Bojarski, "Comments on the determination of excited state dipole moment of molecules using the method of solvatochromism", Spectrochimica Acta Part A: Molecular and Biomolecular Spectroscopy, **82**(1), 527 (2011). https://doi.org/10.1016/j.saa.2011.05.102

[30] A. Chamma, and P. Viallet, "Determination du moment dipolaire d'une molecule dans un etat excite singulet", CR Acad. Sci. Paris Ser. C, **270**, 1901 (1970).

[31] E.V. Lippert, "Spektroskopische Bestimmung des Dipolmomentes aromatischer Verbindungen im ersten angeregten Singulettzustand", Zeitschrift für Elektrochemie, Berichte der Bunsengesellschaft für physikalische Chemie, **61**(8), 962 (1957). https://doi.org/10.1002/bbpc.19570610819

[32] N. Mataga, Y. Kaifu, and M. Koizumi, "Solvent effects upon fluorescence spectra and the dipolemoments of excited molecules", Bulletin of the Chemical Society of Japan, **29**(4), 465 (1956). https://doi.org/10.1246/bcsj.29.465

[33] C. Reichardt, "Solvatochromic dyes as solvent polarity indicators", Chemical reviews, **94**(8), 2319 (1994). https://doi.org/10.1021/cr00032a005

[34] J.-J. Aaron, M.D. Gaye, C. Párkányi, N.S. Cho, and L. von Szentpály, "Experimental and theoretical dipole moments of purines in their ground and lowest excited singlet states", Journal of Molecular Structure, **156**(1-2), 119 (1987). https://doi.org/10.1016/0022-2860(87)85046-9

[35] Y.F. Nadaf, B.G. Mulimani, M. Gopal, and S.R. Inamdar, "Ground and excited state dipole moments of some exalite UV laser dyes from solvatochromic method using solvent polarity parameters", Journal of Molecular Structure: THEOCHEM, **678**(1-3), 177 (2004). https://doi.org/10.1016/j.theochem.2004.01.049

[36] C. Párkányi, Michelle R. Stem-Beren, O. Martínez, J. Aaron, M. Bulaceanu-MacNair, and A. Arrieta, "Solvatochromic correlations and ground-and excited-state dipole moments of curcuminoid dyes", Spectrochimica Acta Part A: Molecular and Biomolecular Spectroscopy, **60**(8-9), 1805 (2004). https://doi.org/10.1016/J.SAA.2003.07.013

[37] A. Kawski, B. Kukliński, and P. Bojarski, "Thermochromic absorption, fluorescence band shifts and dipole moments of BADAN and ACRYLODAN", Zeitschrift für Naturforschung A, **57**(8), 716 (2002). https://doi.org/10.1515/zna-2002-0812

[38] J. Mannekutla, B. Mulimani, and S. Inamdar, "Solvent effect on absorption and fluorescence spectra of coumarin laser dyes: evaluation of ground and excited state dipole moments", Spectrochimica Acta Part A: Molecular and Biomolecular Spectroscopy, **69**(2), 419 (2008). https://doi.org/10.1016/j.saa.2007.04.016

[39] G. Dutt, M. Singh, and A. Sapre, "Rotational dynamics of neutral red: Do ionic and neutral solutes experience the same friction?", The Journal of chemical physics, **109**(14), 5994 (1998). https://doi.org/10.1063/1.477225

[40] A. Belay, E. Libnedenge, H.K. Kim, and Y.-H. Hwang, "Effects of solvent polarity on the absorption and fluorescence spectra of chlorogenic acid and caffeic acid compounds: determination of the dipole moments", Luminescence, **31**(1), 118 (2016). https://doi.org/10.1002/bio.2932

[41] J. Rabek, *Progress in photochemistry and photophysics*, (CRC Press, Boca Raton, USA, 1992), pp. 1-47.

[42] Y.G. Sıdır, and I. Sıdır, "Solvent effect on the absorption and fluorescence spectra of 7-acetoxy-6-(2,3-dibromopropyl)-4, 8-dimethylcoumarin: determination of ground and excited state dipole moments", Spectrochimica Acta Part A: Molecular and Biomolecular Spectroscopy, **102**, 286 (2013). https://doi.org/10.1016/j.saa.2012.10.018

[43] A. Kawski, "On the estimation of excited-state dipole moments from solvatochromic shifts of absorption and fluorescence spectra", Zeitschrift für Naturforschung A, **57**(5), 255 (2002). https://doi.org/10.1515/zna-2002-0509

[44] N. Mataga, and T. Kubota, *Molecular interactions and electronic spectra*, (Marcel Dekker, Inc., New York, 1970), pp. 504. https://doi.org/10.1016/0022-2860(71)87043-6

[45] E. Lippert, "Dipolmoment und Elektronenstruktur von angeregten Molekülen", Zeitschrift für Naturforschung A, **10**(7), 541 (1955). https://doi.org/10.1515/zna-1955-0707

[46] P. Suppan, "Excited-state dipole moments from absorption/fluorescence solvatochromic ratios", Chemical Physics Letters, **94**(3), 272 (1983). https://doi.org/10.1016/0009-2614(83)87086-9

[47] A. Kawski, "Untersuchungen zum zwischenmolekularen Energieübergang in fluoreszierenden Lösungen", Zeitschrift für Naturforschung A, **18**(8-9), 961 (1963). https://doi.org/10.1515/zna-1963-8-911

[48] N. Bakhshiev, "Universal molecular interactions and their effect on the position of the electronic spectra of molecules in two-component solutions. I. Theory (liquid solutions)", Optics and Spectroscopy, **10**, 379 (1961).

[49] Frisch, M., et al., *Gaussian 09*, version D. 01, (Gaussian Inc., Wallingford, CT, 2009).

[50] S. Sidir, and Y.G. Sidir, "Ground state and excited state dipole moments of 6, 8-diphenylimidazo [1, 2-α] pyrazine determined from solvatochromic shifts of absorption and fluorescence spectra", Spectrochim Acta A Mol Biomol Spectrosc. **79**(5), 1220 (2011). https://doi.org/10.1016/j.saa.2011.04.046

[51] B. Vogelsanger, R.D. Brown, P.D. Godfrey, and A.P. Pierlot, "The microwave spectrum of a vitamin: nicotinamide", Journal of Molecular Spectroscopy, **145**(1), 1 (1991). https://doi.org/10.1016/0022-2852(91)90345-B

[52] M. Paluch, and P. Dynarowicz, "The influence of nicotinamide on the adsorption equilibrium of aspirin at the aqueous solution-air interface", Colloid and Polymer Science, **266**(2), 180 (1988). https://doi.org/10.1007/BF01452816

[53] İ. Sıdır, and Y.G. Sıdır, "Estimation of ground and excited state dipole moments of Oil Red O by solvatochromic shift methods", Spectrochimica Acta Part A: Molecular and Biomolecular Spectroscopy, **135**, 560 (2015). https://doi.org/10.1016/j.saa.2014.07.049

[54] İ. Sıdıra, Y.G. Sıdır, H. Berber, and G. Türkoğlu, "Specific and non-specific interaction effect on the solvatochromism of some symmetric (2-hydroxybenzilydeamino) phenoxy Schiff base derivatives", Journal of Molecular Liquids, **215**, 691 (2016). https://doi.org/10.1016/j.molliq.2016.01.042

[55] K. Woldegiorges, A. Belay, A. Kebede, and T. Abebe, "Estimating the Ground and Excited State Dipole Moments of Levofloxacin and Norfloxacin Drugs Using Solvatochromic Effects and Computational Work", Journal of Spectroscopy, **2021**, 7214182 (2021). https://doi.org/10.1155/2021/7214182

[56] K.B. Akshaya, A. Varghese, P.L. Lobo, R, Kumar, and L. George, "Synthesis and photophysical properties of a novel phthalimide derivative using solvatochromic shift method for the estimation of ground and singlet excited state dipole moments", Journal of Molecular Liquids, **224**, 247 (2016). https://doi.org/10.1016/j.molliq.2016.09.115

[57] M.K. Patil, M. Kotresh, and S.R. Inamdar, "A combined solvatochromic shift and TDDFT study probing solute-solvent interactions of blue fluorescent Alexa Fluor 350 dye: Evaluation of ground and excited state dipole moments", Spectrochimica Acta Part A: Molecular and Biomolecular Spectroscopy, **215**, 142 (2019). https://doi.org/10.1016/j.saa.2019.02.022

[58] P. Krawczyk, "Time-dependent density functional theory calculations of the solvatochromism of some azo sulfonamide fluorochromes", Journal of molecular modeling, **21**(5), 118 (2015). https://doi.org/10.1007/s00894-015-2651-z

[59] A.R. Allouche, "Gabedit – A graphical user interface for computational chemistry softwares", Journal of computational chemistry, **32**(1), 174 (2011). https://doi.org/10.1002/jcc.21600

[60] B. Siddlingeshwar and S. M. Hanagodimath, "Estimation of the ground and the first excited singlet-state dipole moments of 1, 4-disubstituted anthraquinone dyes by the solvatochromic method", Spectrochimica Acta Part A: Molecular and Biomolecular Spectroscopy, **75**, 4 (2010). https://doi.org/10.1016/j.saa.2009.12.007

[61] M. Ravi, T. Soujanya, A. Samanta, and T. P. Radhakrishnan, "Excited-state dipole moments of some Coumarin dyes from a solvatochromic method using the solvent polarity parameter, ENT", Journal of the Chemical Society, Faraday Transactions, **91**, 17 (1995). https://doi.org/10.1039/FT9959102739

ВПЛИВ ПОЛЯРНОСТІ РОЗЧИННИКА НА СПЕКТРИ ПОГЛИНАННЯ ТА ФЛУОРЕСЦЕНЦІЇ НІКОТИНАМІДУ: ВИЗНАЧЕННЯ ДИПОЛЬНИХ МОМЕНТІВ ОСНОВНОГО ТА ЗБУДЖЕНОГО СТАНІВ

Атакльті Абраха Гебрейоханес[a], Абебе Белай[b], Гетачеу Алему[a]
[a]Факультет фізики університету Самара, Самара, Ефіопія
[b]Програма прикладної фізики, Науково-технологічний університет Адама, Адама, Ефіопія

У цьому дослідженні дипольні моменти основного та збудженого станів нікотинаміду (NIC) були оцінені за допомогою сольватохромних ефектів і комп'ютерних обчислень. Подано загальний огляд впливу розчинників на електронні спектри поглинання та флуоресценції NIC. В обох спектрах спостерігалися виражені сольватохромні ефекти, а зсув піків випромінювання був більшим, ніж у відповідних спектрах поглинання. Експериментальні дипольні моменти основного $\left(\mu_g \right)$ та збудженого $\left(\mu_e \right)$ станів NIC оцінюються за сольватохромними зсувами спектрів поглинання та флуоресценції. Відмінності між дипольними моментами збудженого та основного станів, визначеними всіма методами, досить схожі. Розраховані енергетичні заборонені зони HOMO-LUMO, які становлять 5,566 eВ. Виявлено, що дипольний момент збудженого стану вищий, ніж у основного стану для всіх використаних методів, і це пояснюється більш полярним збудженим станом NIC. Нарешті, спостережувані спектральні властивості, виміряні значення дипольних моментів та електронні структури NIC у різних розчинниках надають важливі відомості про розподіл заряду та взаємодію між розчиненою речовиною та розчинником, що може бути корисним у дослідженні цих молекул у біологічних системах.

Ключові слова: метод сольватохромного зсуву, дипольні моменти основного стану, дипольні моменти збудженого стану, нікотинамід

RELATIVISTIC SYMMETRIES OF BOSONIC PARTICLES AND ANTIPARTICLES IN THE BACKGROUND OF THE POSITION-DEPENDENT MASS FOR THE IMPROVED DEFORMED HULTHÉN PLUS DEFORMED TYPE-HYPERBOLIC POTENTIAL IN 3D-EQM SYMMETRIES[†]

Abdelmadjid Maireche

Department of Physics, M'sila University, PMC Laboratory, M'sila University, Algeria
E-mail: abdelmadjid.maireche@univ-msila.dz
Received October 10, 2022; revised, November 12, 2022; accepted November 16, 2022

The bound state solutions of the deformed Klien-Gordon equation have been determined in the three-dimensional extended relativistic quantum mechanics 3D-ERQM symmetries using position-dependent mass (PDM) with unequal scalar and vector potential for the improved Hulthén plus improved deformed type-hyperbolic potential (PDM-SVID(H-TP)) models. PDM with unequal scalar and vector potential for the Hulthén plus deformed type-hyperbolic potential (PDM-(SVH-DTP)) models, as well as a combination of radial terms, which are coupled with the coupling $\mathbf{L\Theta}$, which explains the interaction of the physical features of the system with the topological deformations of space-space. The new relativistic energy eigenvalues have been derived using the parametric Bopp shift method and standard perturbation theory which is sensitive to the atomic quantum numbers (j,l,s,m), mixed potential depths (V_0, S_0, V_1, S_1), the rest, and perturbed mass $\left(m_0, m_1\right)$, the screening parameter's inverse α , and noncommutativity parameters $\left(\Theta, \tau, \chi\right)$. Within the framework of 3D-ERQM symmetries, we have treated certain significant particular instances that we hope will be valuable to the specialized researcher. We have also treated the nonrelativistic limit and applied our obtained results to generate the mass spectra of heavy-light mesons (HLM) such as $c\bar{c}$ and $b\bar{b}$ under PDM-SE with improved deformed Hulthén plus improved hyperbolic potential (PDM-ID(H-TP)) models. When the three simultaneous limits $\left(\Theta, \tau, \chi\right)$ were applied, we recovered the normal results of relativistic in the literature ($0,0,0$) for the PDM-ID(H-TP)) models.
Keywords: Klien-Gordon equation, deformed Hulthén plus deformed type-hyperbolic potential, heavy-light mesons, Noncommutative quantum mechanics and Bopp's shift method, Canonical noncommutativity
PACS: 03.65.−w;03.65.Ge;05.30.Jp

1. INTRODUCTION

One of the significant issues in quantum mechanics (QM) and noncommutative quantum mechanics (NCQM) or extended quantum mechanics (EQM) is the investigation of solutions to the nonrelativistic Schrödinger equation (SE) or relativistic Klien-Gordon (KG), Dirac and Duffin-Kemmer-Petiau equations for a particle with spin 0, 1/2 or (1,2...) under the real physical potentials. The hyperbolic and Hulthén potentials are considered to be one of the most important interactions that have received great attention. It has been the subject of an in-depth study by many researchers within the framework of fundamental equations [1-5] whether it is a single treatment or a combination of both. In their study of the bound and scattering states of the KGE with deformed Hulthén plus deformed hyperbolical potential for arbitrary states, Ikot *et al.* used supersymmetry quantum mechanics and factorization techniques [6]. The variable mass formalism provides relevant and practical theoretical predictions of a variety of experimental properties for many-body quantum systems for this goal [7,8]. The effective mass notion has been applied to numerous important issues in the literature, including nuclei, metallic clusters, ^{3}He clusters, quantum liquids, and nuclei [9-13]. In the present work, we aim to investigate the solution of KG and SE with deformed Hulthén plus deformed-type hyperbolic potential in 3D-ERQM and 3D-ENRQM symmetries to develop the physical concepts in ref. [6]. We aspire through this work to reveal more new applications within the framework of extended postulates that include more comprehensive axioms than we know about relativistic quantum mechanics (see below). These new postulates were connected to the deformation space-space and phase-phase. The divergence problem of the standard model, gravity quantization, the problem of unifying it with the rest of the fundamental interactions, and other significant physical problems have emerged despite the brilliant successes of quantum mechanics in treating physical and chemical systems in various research fields [14-21]. It should be mentioned that before the renormalization approach was created and gained popularity, Heisenberg proposed the idea of extended noncommutativity to the coordinates as a possible treatment for eliminating the limitless number of field theories in 1930. Snyder published the first work on QFT's history in 1947 [22], and Connes introduced its geometric analysis in 1991 and 1994 [23,24] to standardize QFT. I believe that this research will contribute to further subatomic scale investigations and scientific knowledge of elementary particles. The position-dependent mass with unequal scalar and vector potential for the improved deformed Hulthén plus improved type-hyperbolic potential (PDM-SVID(H-TP)) models in the 3D-ERQM symmetries was motivated by the fact that it had not been reported in the literature for bosonic particles and antiparticles.

The following are the vector and scalar that will be used in this study $F_{ht}(r) \equiv (V_{ht}(r_{nc}), S_{ht}(r_{nc})$ and $m_{ht}(r_{nc})$ which are unified in the following form:

$$F(r_{nc}) = F_{ht}(r) - \frac{1}{2r}\frac{\partial F_{ht}(r)}{\partial r}\mathbf{L}\Theta + O(\Theta^2),\tag{1}$$

where $V_{ht}(r), S_{ht}(r)$ and $m_{ht}(r)$ are the (vector, scalar) potentials and PDM, in 3D-RQM known in the literature [6]:

$$\begin{cases} V_{ht}/S_{ht} = -\frac{V_0/S_0 e^{(-2\alpha r)}}{1-qe^{(-2\alpha r)}} + \frac{V_1/S_1\left(1+qe^{(-2\alpha r)}\right)}{1-qe^{(-2\alpha r)}} \\ m_{ht}(r_{nc}) = m_0 + \frac{m_1}{1-qe^{(-2\alpha r)}} \end{cases},\tag{2}$$

where V_0/V_1 stand for the potential wells' depths, q for deformation, and α is the screening parameter's inverse, m_0 is the integration constant (rest mass of the bosonic particles and antiparticles), m_1 is the perturbed mass, $(r_{nc}$ and $r)$ are the distances in the EQM and usual QM symmetries, respectively.

The coupling $\mathbf{L}\Theta$ is the scalar product of the usual components of the angular momentum operator $\mathbf{L}(L_x, L_y, L_z)$ and the modified noncommutativity vector $\Theta(\theta_{12}, \theta_{23}, \theta_{13})/2$ which present the noncommutativity elements parameter. In the case of G_{NC}, the noncentral generators can be suitably realized as self-adjoint differential operators (x_μ^{nc}, p_ν^{nc}) in 3D-EQM symmetries. NC canonical commutations in a variety of canonical structures satisfying a deformed algebra of the form (we have used the natural units $\hbar = c = 1$) [25-30]:

$$\begin{cases} \left[x_\mu^{nc*}, p_\nu^{nc}\right] = i\hbar_{eff}\delta_{\mu\nu} \\ \left[x_\mu^{nc*}, x_\nu^{nc}\right] = i\varepsilon_{\mu\nu}\theta \end{cases}.\tag{3}$$

The corresponding generalizing momentums (x_μ and p_μ) in the usual QM symmetries, respectively. Here $\delta_{\mu\nu}$ is the Kronecker symbol, $(\mu,\nu=1,2,3)$, $\theta_{\mu\nu}$ is antisymmetric real constant (3×3) matrices with the dimensionality (length)^2 parameterizing the deformation of space-space, $\varepsilon_{\mu\nu}$ is the Levi-Civita symbol ($\varepsilon_{\mu\nu} = -\varepsilon_{\nu\mu} = 1$ for $\mu \neq \nu$ and $\varepsilon_{\varepsilon\varepsilon} = 0$), and $\theta \in \mathrm{R}$ is the noncommutative parameter which measures the non-commutativity of coordinates, $\hbar_{eff} \cong \hbar$ is the effective Planck constant. In the first order of the noncommutativity parameter $\varepsilon^{\mu\nu}\theta$, the scalar product in 3D-EQM symmetries is expressed in terms $(h*g)(x)$ as follows [31-34]:

$$(h*g)(x) \approx (hg)(x) - i\varepsilon^{\mu\nu}\theta/2\partial_\mu^x h\partial_\nu^x g\big|_{x^\mu=x'}.\tag{4}$$

The outline of the paper is as follows: Sect. 2 presents an overview of the 3D-KGE under the PDM-SVID(H-TP) model. Sect. 3 is devoted to investigating the 3D-DKGE using the well-known Bopp's shift method to obtain the effective potential of the PDM-SVID(H-TP) model. Furthermore, using standard perturbation theory, we find the expectation values of some radial terms to calculate the corrected relativistic energy generated by the effect of the perturbed effective potential $W_{pert}^{ht}(r)$, and we derive the global corrected energies for *bosonic particles* and *bosonic antiparticles* whose spin quantum number has an integer value ($0,1,2...$). Sect. 4 is reserved for the study of important relativistic particular cases in 3D-ERQM symmetries. The next section is reserved for the nonrelativistic limits for PDM-SVID(H-TP) model*s* in 3D-ENRQM symmetries and we apply these results to generate mass spectra of HLM systems. Finally, we present our conclusion in Sec. 7.

2. AN OVERVIEW OF KGE UNDER THE PDM-SVD(H-TP) MODEL IN RQM SYMMETRY
The radial component $u_{nl}(r)$ of the wave function solution $\Psi_{nl}(r,\theta,\phi)$ satisfies the differential equation below [6]:

$$\left(\frac{d^2}{dr^2} + E_{nl}^2 - m_0^2 - W(r)\right)u_{nl}(r) = 0.\tag{5}$$

The effective potential $W_{eff}^{ht}(r)$ is determined from:

$$W_{eff}^{ht}(r) = \frac{\omega_1 \exp(-4\alpha r) + \omega_2 \exp(-2\alpha r) + \omega_3}{(1 - q\exp(-2\alpha r))^2}.$$ (6)

The parameters ω_1, ω_2 and ω_3 are determined in Ref. [6] as a function of $(V_0, S_0, V_1, S_1, m_0, m_1)$. The author of this Ref. used the SUSYQM and factorization methods to obtain the expression $u_{nl}(r)$ as a function of generalized Jacobi polynomial $P^{(u,v)}(x)$ in RQM symmetries. We reformulate the relativistic wave function $\Psi_{nl}(r,\theta,\phi)$ in terms of the hypergeometric polynomials $_2F_1\left(-n, n+2\sqrt{\chi_{nl}^3}+2\beta_{nl}+1; 1+2\sqrt{\chi_{nl}^3}, z\right)$ as,

$$\Psi_{nl} = N_{nl}^n Y_m^l(\theta,\phi)\frac{z^{\sqrt{\chi_{nl}^3}}}{r}(1-z)^{\beta_{nl}} {}_2F_1\left(-n, n+2\sqrt{\chi_{nl}^3}+2\beta_{nl}+1; 1+2\sqrt{\chi_{nl}^3}, z\right),$$ (7)

where z equal $q\exp(-2\alpha r)$ while N_{nl} and (χ_{nl}^1, χ_{nl}^2 and χ_{nl}^3) are given by:

$$\begin{cases} \chi_{nl}^1 = \dfrac{\omega_1}{4\alpha^2 q^2} - \dfrac{E_{nl}^2 - m_0^2}{4\alpha^2}, \chi_{nl}^2 = -\dfrac{\omega_2}{4\alpha^2 q^2} - \dfrac{E_{nl}^2 - m_0^2}{4\alpha^2} \\[3mm] \chi_{nl}^3 = \dfrac{\omega_3}{4\alpha^2 q^2} - \dfrac{E_{nl}^2 - m_0^2}{4\alpha^2}, \text{ and } \dfrac{N_{nl}\Gamma\left(n+2\sqrt{\chi_{nl}^3}+1\right)}{n!\Gamma\left(2\sqrt{\chi_{nl}^3}+1\right)}, \end{cases}$$ (8)

with β_{nl} equal $\sqrt{\dfrac{1}{4} + \chi_{nl}^1 - \chi_{nl}^2 + \chi_{nl}^3}$. We obtained the energy for bosonic particles E_{nl}^+ and bosonic antiparticles E_{nl}^-, from the square root of the equation of energy [6]:

$$E_{nl}^2 - m_0^2 = -\frac{1}{4q^2}\left(\frac{\omega_3 q^2 - \omega_1}{2\alpha\sigma} + 2\alpha(n+\sigma)\right)^2 + \omega_3,$$ (9)

where $\sigma = \frac{q}{2}\left(1 + \sqrt{1 + \frac{1}{\alpha^2 q^2}(\omega_1 + q\omega_2 - q^2\omega_3)}\right)$

3. SOLUTIONS OF PDM-SVID(H-TP) MODELS IN 3D-ERQM SYMMETRIES

By applying the new principles which we have seen in the introduction, Eqs. (3) and (4), summarized in new relationships MASCCCRs and the notion of the Weyl-Moyal star product. These data allow us to rewrite the usual radial KG equations in Eq. (5) in 3D-ERQM symmetries as follows:

$$\left(\frac{d^2}{dr^2} + E_{nl}^2 - m_0^2 - W_{eff}^{ht}(r)\right) * u_{nl}(r) = 0.$$ (10)

There are two approaches to including non-commutativity in the quantum field theory: either through the Moyal product on the space of ordinary functions or by redefining the field theory on a coordinate operator space that is inherently noncommutative [35-37]. It is known to specialists that the star product can be translated into the ordinary product known in the literature using what is called Bopp's shift method. F. Bopp was the first to consider pseudo-differential operators obtained from a symbol by the quantization rules $(x, p) \rightarrow \left(\hat{x} = x - \frac{i}{2}\partial_p, \hat{p} = x + \frac{i}{2}\partial_x\right)$ instead of ordinary correspondence $(x, p) \rightarrow \left(\hat{x} = x, \hat{p} = x + \frac{i}{2}\partial_x\right)$, respectively. This procedure is known as Bopp's shifts (BS) method, and this quantization procedure is known as Bopp quantization [38-45]. It is worth motioning that the BS method permutes us to reduce Eq. (10) in the simplest form:

$$\left(\frac{d^2}{dr^2} + E_{nl}^2 - m_0^2 - W_{eff}^{ht}(r_{nc})\right) u_{nl}(r) = 0.$$ (11)

The Taylor expansion of $W(r_{nc})$ can be expressed as in the 3D-ERQM symmetries, as [42-52]:

$$W_{eff}^{ht}(r_{nc}) = W_{eff}^{ht}(r) - \frac{\partial W_{eff}^{ht}(r)}{2r\partial r}\mathbf{L}\Theta + O(\Theta^2).$$ (12)

Substituting Eq. (12) into Eq. (11), we obtain the following, as in the Schrödinger equation:

$$\left(\frac{d^2}{dr^2} + E_{nl}^2 - m_0^2 - W_{eff}^{ht}(r) - W_{ht}^{pert}(r)\right)u_{nl}(r) = 0,$$ (13)

with

$$W_{ht}^{pert}(r) = -\frac{1}{2r}\frac{\partial W_{eff}^{ht}(r)}{\partial r}\mathbf{L}\Theta + O(\Theta^2).$$ (14)

By comparing Eqs. (5) and (11), we observe an additive potential $W_{ht}^{pert}(r)$ dependent on new radial terms, which are coupled with the coupling $\mathbf{L}\Theta$ that explains the interaction of the physical features of the system with the topological deformations of space-space:

$$W_{ht}^{pert}(r) = \left(\begin{array}{l} \dfrac{2\alpha\omega_1\exp(-4\alpha r)}{r\left(1-qe^{(-2\alpha r)}\right)^2} + \dfrac{\alpha\omega_2\exp(-2\alpha r)}{r\left(1-q\exp(-2\alpha r)\right)^2} + \dfrac{2\alpha q\omega_1\exp(-6\alpha r)}{r\left(1-q\exp(-2\alpha r)\right)^3} + \\[4mm] + \dfrac{2\alpha q\omega_2\exp(-4\alpha r)}{r\left(1-q\exp(-2\alpha r)\right)^3} + \dfrac{2\alpha q\omega_3\exp(-2\alpha r)}{r\left(1-q\exp(-2\alpha r)\right)^3} \end{array}\right)\mathbf{L}\Theta + O(\Theta^2),$$ (15)

Eq. (13) cannot be solved analytically for any state $l \neq 0$ because of the centrifugal term and the studied potential itself. The effective perturbative potential $W_{ht}^{pert}(r)$ in Eq. (15) has a strong singularity $r \to 0$, we need to use the suitable approximation of the centrifugal term proposed by Kurniawan *et al.* [46] and applied by Ikot *et al.* [47]. The radial part of the 3D-DKGE with the PDM-SVID(H-TP) model*s* contains the centrifugal term $l(l+1)/r^2$ and $l(l+1)/r^4$ since we assume $l \neq 0$. However, the PDM-SVID(H-TP) model is a kind of potential that cannot be solved exactly when the centrifugal term is taken into account unless $l = 0$ is assumed. The conventional approximation used in this paper is as follows:

$$1/r^2 \approx \alpha^2/\sinh_q^2(\alpha r) = 4\alpha^2/(1-z)^2.$$ (16)

This gives the perturbative effective potential as follows:

$$W_{ht}^{pert}(r) = \left(\frac{\beta_1 z^2}{(1-z)^3} + \frac{\beta_1 z}{(1-z)^3} + \frac{\beta_3 z^3}{(1-z)^4} + \frac{\beta_4 z^2}{(1-z)^4} + \frac{\beta_5 z}{(1-z)^4}\right)\mathbf{L}\Theta + O(\Theta^2),$$ (17)

with $\beta_1 = \dfrac{4\alpha^2\omega_1}{q^2}$, $\beta_2 = \dfrac{2\alpha^2\omega_2}{q}$, $\beta_3 = \dfrac{4\alpha^2\omega_1}{q^2}$, $\beta_4 = \dfrac{4\alpha^2\omega_2}{q}$ and $\beta_5 = 4\alpha^2\omega_3$.

The PDM-SVID(H-TP) model is extended by including new radial terms $\dfrac{z^2}{(1-z)^3}$, $\dfrac{z}{(1-z)^3}$, $\dfrac{z^3}{(1-z)^4}$, $\dfrac{z^2}{(1-z)^4}$

and $\dfrac{z}{(1-z)^4}$ to become PDM-SVID(H-TP) model*s* in 3D-ERQM symmetries. The new additive part $W_{ht}^{pert}(r)$ is also proportional to the infinitesimal coupling $\mathbf{L}\Theta$, this is logical from a physical point of view because it explains the interaction between the physical properties of the studied potential $\mathbf{L}$ and the topological properties resulting from the deformation of space-space Θ. This allows us to consider the additive effective potential as a perturbation potential compared with the main potential $W_{ht}(r)$ (parent potential operator) in the symmetries of 3D-ERQM symmetries, that is, the inequality $W_{ht}^{pert}(r) \prec\prec W_{ht}(r)$ has become achieved. That is all the physical justifications for applying the time-independent perturbation theory become satisfied. This allows us to give a complete prescription for determining the energy level of the generalized $(n,l,m)^{th}$ excited states.

3.1. The expectation values $W_{ht}^{pert}(r)$ in the 3D-ERQM symmetries

In this subsection, we want to apply perturbative theory in the first order to find the expectation values $A_{(nlm)}^{1ht}$, $A_{(nlm)}^{2ht}$, $A_{(nlm)}^{3ht}$, $A_{(nlm)}^{4ht}$ and $A_{(nlm)}^{5ht}$ for bosonic particles and bosonic antiparticles taking into account the unperturbed $\Psi_{nl}(r,\theta,\phi)$ which we have seen previously in Eq. (7):

$$
\begin{cases}
A_{(nlm)}^{1ht} = N \int_{0}^{+q} z^{2\sqrt{\chi_{nl}^{3}}+2-1}\left(1-z\right)^{2\beta_{nl}-2-1} F\,dz \\[2mm]
A_{(nlm)}^{2ht} = N \int_{0}^{+q} z^{2\sqrt{\chi_{nl}^{3}}+1-1}\left(1-z\right)^{2\beta_{nl}-2-1} F\,dz \\[2mm]
A_{(nlm)}^{3ht} = N \int_{0}^{+q} z^{2\sqrt{\chi_{nl}^{3}}+3-1}\left(1-z\right)^{2\beta_{nl}-3-1} F\,dz \\[2mm]
A_{(nlm)}^{4ht} = N \int_{0}^{+q} z^{2\sqrt{\chi_{nl}^{3}}+2-1}\left(1-z\right)^{2\beta_{nl}-3-1} F\,dz \\[2mm]
A_{(nlm)}^{5ht} = N \int_{0}^{+q} z^{2\sqrt{\chi_{nl}^{3}}+1-1}\left(1-z\right)^{2\beta_{nl}-3-1} F\,dz
\end{cases}
\tag{18}
$$

with

$$
F \equiv \left[\,{}_2F_1\left(-n, n+2\sqrt{\chi_{nl}^{3}}+2\beta_{nl}+1; 1+2\sqrt{\chi_{nl}^{3}}, z\right)\right]^2,
$$

and $N = \dfrac{N_{nl}^{n2}}{2\alpha}$.

We have used useful abbreviations $\langle A\rangle_{(nlm)}^{iht} = \langle n,l,m \| A \| n,l,m\rangle$ to avoid the extra burden of writing. Furthermore, we have introduced the change of variable $z = q\exp(-2\alpha r)$. This maps the region $0 \le r \prec \infty$ to $0 \le z \le q$ and allows us to obtain $dr = -1/2\,\dfrac{dz}{\alpha z}$. We can evaluate the above integrals either in a recurrence way through the physical values of the principal quantum number ($n=0,1,\dots$) and then generalize the result to the general $(n,l,m)^{th}$ excited state or we use the method proposed by Dong *et al.* [48] and applied by Zhang [49], to obtain the general excited state directly. We calculate the integrals in Eqs. (20) with help of the special integral formula:

$$
\int_{0}^{1} z^{\xi-1}\left(1-s\right)^{\tau-1}\left[\,{}_2F_1\left(c_1,c_2;c_3;z\right)\right]^2 dz = \frac{\Gamma(\xi)\Gamma(\tau)}{\Gamma(\xi+\tau)}\,{}_3F_2\left(c_1,c_2,\beta;c_3,\beta+\alpha;1\right),
\tag{19}
$$

here ${}_3F_2\left(c_1,c_2,\beta;c_3,\beta+\alpha;1\right)$ equal $\sum_{n=0}^{+\infty}\dfrac{(c_1)_n(c_2)_n(\tau)_n}{(c_3)_n(\tau+\xi)n!}$, the symbol $(c_1)_n$ denotes the rising factorial or Pochhammer symbol while $\Gamma(\xi)0$ denoting the usual Gamma function. For the case $q=1$ and by identifying Eqs. (18) with the integrals in Eq. (21), we obtain the following results:

$$
\begin{cases}
A_{(nlm)}^{1ht} = \dfrac{\Gamma\left(2\sqrt{\chi_{nl}^{3}}+2\right)\Gamma\left(2\beta_{nl}-2\right)}{N^{-1}\Gamma\left(B_{nl}\right)}\,{}_3F_2\left(Y_{nl},B_{nl};1\right) \\[4mm]
A_{(nlm)}^{2ht} = \dfrac{\Gamma\left(2\sqrt{\chi_{nl}^{3}}+1\right)\Gamma\left(2\beta_{nl}-2\right)}{N^{-1}\Gamma\left(B_{nl}-1\right)}\,{}_3F_2\left(Y_{nl},B_{nl}-1;1\right) \\[4mm]
A_{(nlm)}^{3ht} = \dfrac{\Gamma\left(2\sqrt{\chi_{nl}^{3}}+3\right)\Gamma\left(2\beta_{nl}-3\right)}{N^{-1}\Gamma\left(B_{nl}\right)}\,{}_3F_2\left(Y_{nl}^{'},B_{nl};1\right) \\[4mm]
A_{(nlm)}^{4ht} = \dfrac{\Gamma\left(2\sqrt{\chi_{nl}^{3}}+2\right)\Gamma\left(2\beta_{nl}-3\right)}{N^{-1}\Gamma\left(B_{nl}-1\right)}\,{}_3F_2\left(Y_{nl}^{'},B_{nl}-1;1\right) \\[4mm]
A_{(nlm)}^{5ht} = \dfrac{\Gamma\left(2\sqrt{\chi_{nl}^{3}}+1\right)\Gamma\left(2\beta_{nl}-3\right)}{N^{-1}\Gamma\left(B_{nl}-2\right)}\,{}_3F_2\left(Y_{nl}^{'},B_{nl}-2;1\right)
\end{cases}
\tag{20}
$$

with

$$B_{nl} = 2\sqrt{\chi_{nl}^3} + 2\beta_{nl},$$

$$Y_{nl} = \left(-n, n + 2\sqrt{\chi_{nl}^3} + 2\beta_{nl} + 1, X_{nl}; 1 + 2\sqrt{\chi_{nl}^3}\right),$$

$$Y'_{nl} = \left(-n, n + 2\sqrt{\chi_{nl}^3} + 2\beta_{nl} + 1 X'_{nl}; 1 + 2\sqrt{\chi_{nl}^3}\right),$$

and

$$X'_{nl} = 2\beta_{nl} - 3.$$

3.2. The corrected energy for the PDM-SVID(H-TP) models

The crucial goal of this sub-section is to identify the contribution under the PDM-SVID(H-TP) models, in 3D-ERQM symmetries, arising from deformation space-space using the method we have successfully applied in the past and are always working to develop. We can confirm that the PDM-SVD(H-TP) models are in place, which we provided through a summary of the *bosonic particles* and *bosonic antiparticles* in Eq. (9), produce a significant contribution to relativistic energy known in the literature under deformation KG theory, whereas the new contribution is generated from the topological properties under space-space deformation. The influence of the perturbed spin-orbit effective potential $W_{ht}^{pert}(r)$ corresponding to the *bosonic particles* and *bosonic antiparticles* with spin-s produces the first contribution.

We obtain the perturbed spin-orbit effective potential by replacing the coupling of the angular momentum operator $\mathbf{L}$ and the NC vector Θ with the new equivalent coupling $\mathbf{L}\Theta \rightarrow \Theta\mathbf{LS}$ $\left(\Theta = \sqrt{\Theta_{12}^2 + \Theta_{23}^2 + \Theta_{13}^2}\right)$. This degree of freedom results from the arbitrary nature of the infinitesimal NC vector Θ. We have oriented the spin-s of the *bosonic particles* and *bosonic antiparticles* to become parallels to the vector Θ which interacted with the PDM-SVID(H-TP) model*s*. Additionally, we use the following transformation which is well known in QM symmetries:

$$\Theta\mathbf{LS} \rightarrow (\Theta/2)\mathbf{G}^2,$$

with

$$\mathbf{G}^2 = \mathbf{J}^2 - \mathbf{L}^2 - \mathbf{S}^2.$$

It is well known in QM symmetries, that the operators ($\hat{\mathbf{H}}_{nc}^{ht}$, $\mathbf{J}^2$, $\mathbf{L}^2$, $\mathbf{S}^2$ and $\mathbf{J}_z$) form a complete set of conserved physics quantities, and the eigenvalues $2F(j,l,s)$ of the operator $\mathbf{G}^2$ are equal to the values $j(j+1) - l(l+1) - s(s+1)$, $|l-s| \leq j \leq |l+s|$ in 3D-ERQM symmetry. As a direct consequence, the square partially corrected energies ΔE_{ht}^{so2} due to the perturbed effective potential $W_{ht}^{pert}(r)$ produced for the $(n,l,m)^{th}$ excited state, as follows:

$$\Delta E_{ht}^{so2} = \Theta F(j,l,s) \left\langle K \right\rangle_{(nlm)}^{ht}. \tag{21}$$

The global expectation values $\left\langle K \right\rangle_{(nlm)}^{ht}$ for the *bosonic particles* and *bosonic antiparticles*, which were created from the effect of the PDM-SVID(H-TP) model*s*, are determined from the following expression:

$$\left\langle K \right\rangle_{(nlm)}^{ht} = \sum_{\alpha=1}^{5} \beta_\alpha A_{(nlm)}^{\alpha ht}. \tag{22}$$

The second principal physical contribution for the perturbed potential $W_{ht}^{pert}(r)$ is proven when we substitute the coupling interaction $\mathbf{L}\Theta$ with physical coupling $\tau\vec{L}\aleph$ and we chose $\aleph = \aleph_z$ for simplification with physical condition $[\Theta] = [\tau][\aleph] \equiv (\text{length})^2$, here ($\aleph$ and τ) present the intensity of the magnetic field induced by the effect of the deformation of space-space geometry and a new infinitesimal noncommutativity parameter. This choice that the magnetic field is directed according to the (Oz) axis serves to simplify quantitative calculations without affecting the nature of the physical point of view; we also need to apply the identity $\left\langle n', l', m' | L_z | n, l, m \right\rangle$ which is equal to $m\delta_{m'm}\delta_{l'l}\delta_{n'n}$ ($-|l| \leq m \leq +|l|$). All of these data allow for the discovery of the new square improved energy shift ΔE_{ht}^{mg2} due to the perturbed Zeeman effect

created by the influence of the PDM-SVID(H-TP) model*s* for the $(n,l,m)^{th}$ excited state in 3D-ERQM symmetries as follows:

$$\Delta E_{ht}^{mg\,2} = \tau \aleph \left\langle K \right\rangle_{(nlm)}^{ht} m \quad . \tag{23}$$

After we have completed the first and second stages of the self-production of energy, we are going to discover another very important case under the PDM-SVID(H-TP) model*s* in 3D-ERQM symmetries. This physical new phenomenon is produced automatically from the influence of perturbed effective potential $W_{ht}^{pert}(r)$. We consider the *bosonic particles* and *bosonic antiparticles* undergoing rotation with angular velocity Ω. The features of this subjective phenomenon are determined through the substitute of the arbitrary vector Θ with the new physical quantity $\chi\Omega$. Allowing us to replace the coupling $\mathbf{L}\Theta$ with $\chi\mathbf{L}\Omega$, χ is just an infinitesimal real proportional constant. The effective potentials $W_{pert}^{ht-rot}(z)$ which induced the rotational movements can be expressed as follows:

$$W_{pert}^{ht-rot}(r) = \chi \left\langle K \right\rangle_{(nlm)}^{ht} \mathbf{L}\Omega . \tag{24}$$

We chose a rotational velocity Ω parallel to the (Oz) axis ($\Omega = \Omega \mathbf{e}_z$) to simplify the calculations. The perturbed generated spin-orbit coupling is then transformed into new physical phenomena as follows:

$$W_{pert}^{ht-rot}(z)\mathbf{L}\Omega = \chi\Omega W_{pert}^{ht-rot}(z) L_z . \tag{25}$$

All of these data allow for the discovery of the new corrected square improved energy $\Delta E_{ht}^{rot\,2}$ due to the perturbed effective potential $W_{pert}^{ht-rot}(z)$ which is generated automatically by the influence of the PDM-SVID(H-TP) model*s* for the $(n,l,m)^{th}$ excited state in 3D-ERQM symmetries as follows:

$$\Delta E_{ht}^{rot\,2} = \chi\Omega \left\langle K \right\rangle_{(nlm)}^{ht} m . \tag{26}$$

It is worth noting that the authors of ref. [48] were studied rotating isotropic and anisotropic harmonically confined ultra-cold Fermi gases in two and 3D space at zero temperature, but in this case, the rotational term was manually added to the Hamiltonian operator, whereas, in our study, the rotation operator $W_{pert}^{ht-rot}(z)\mathbf{L}\Omega$ appears automatically due to the effect of the deformation of space-space under the PDM-SVID(H-TP) model*s*. The eigenvalues of the operations $\mathbf{G}^2$ for bosonic particles and antiparticles (negative energy) with spin $s = (1,2..)$ are equal to the following values $F(j,l,s)$. In the 3D-ERQM symmetries, the total relativistic improved energy E_{nc}^{ht} for the case of the bosonic particles and bosonic antiparticles with spin has an integer value ($0,1,2...$) and satisfies the Bose-Einstein statistics such as ($\pi^{\pm}$ and π^0) with PDM-SVID(H-TP) model*s*, corresponding to the generalized $(n,l,m)^{th}$ excited states are expressed as:

$$E_{nc}^{ht} = E_{nl}^{\pm} \pm [\left\langle K \right\rangle_{(nlm)}^{ht} (\Lambda(\aleph\Omega) m + \Theta F)]^{1/2} , \tag{27}$$

where

$$\Lambda(\aleph\Omega) \equiv \tau\aleph + \chi\Omega . $$

Here $E_{nl}^{\pm}$ are usual relativistic energies under the PDM-SVID(H-TP) model obtained from equations of energy in Eq. (9). It should be noted that the positive and negative sign denotes the improved energy of the bosonic particles which corresponds to the positive and negative energy of the bosonic antiparticles which corresponds to the negative energy. We can now generalize our obtained energies $E_{t-nc}^{ht-b/ap}$, in a unified formula, under the PDM-SVID(H-TP) model*s* that were produced with the global induced potential $W_{ht}^{pert}(r)$:

$$E_{t-nc}^{ht-b/ap} = E_{nc}^{ht} \theta\left(\left|E_{nc}^{ht}\right|\right) - E_{nc}^{ht-s} \theta\left(-\left|E_{nc}^{ht}\right|\right) , \tag{28}$$

by using the unit step function (also known as a viside step function $\theta(x)$ or simply the theta function). It is important to point out that because we have only used corrections of the first order of infinitesimal noncommutative parameters (Θ, τ, χ), perturbation theory cannot be used to find corrections of the second order $(\Theta^2, \tau^2, \chi^2)$.

4. STUDY OF IMPORTANT RELATIVISTIC PARTICULAR CASES IN 3D-ERQM SYMMETRIES

We will look at some specific examples involving the new bound state energy eigenvalues in Eq. (27) in this section. By adjusting relevant parameters of the PDM-SVID(H-TP) model*s* in the 3D-ERQM, we could derive some specific potentials useful for other physical systems for much concern the specialist reach.

(1). If we choose, $V_1 = 0$, $S_0 = S_1 = m_1 = 0$ and $\alpha \to \alpha/2$ in Eq. (1), we obtain the improved generalized Hulthén potential (GHP) and the global relativistic energy for the bosonic particles E_{nc}^{hp-p} (bosonic antiparticles E_{nc}^{hp-ap}) under the improved GHP in 3D-ERQM symmetries as:

$$
\begin{cases}
V_h(r_{nc}) = V_h(r) - \left(\dfrac{\frac{\alpha}{2} V_0 e^{(-\alpha r)}}{r\left(1 - q e^{(-\alpha r)}\right)} + \dfrac{q \frac{\alpha}{2} V_0 e^{(-2\alpha r)}}{r\left(1 - q e^{(-\alpha r)}\right)^2} \right) \mathbf{L}\Theta \\[3mm]
E_{nc}^{hp} = E_{nl}^{hp\pm} \pm \left[\langle K \rangle_{(nlm)}^{hp} \left(\Lambda(\aleph\Omega)m + \Theta F \right) \right]^{1/2}
\end{cases}
. \tag{29}
$$

Here $V_h(r)$ presents the GHP in 3D-RQM symmetries [51], while $\langle K \rangle_{(nlm)}^{hp}(n, V_0, \alpha, m)$ is determined from the limits:

$$
\langle K \rangle_{(nlm)}^{hp}(n, V_0, \alpha, m) = \underset{(V_1 = S_0 = S_1 = m_1, \alpha) \to (0, \alpha/2)}{Lim} \langle K \rangle_{(nlm)}^{ht}.
$$

The first two parts $E_{nl}^{hp\pm}$ describe the relativistic energies of bosonic particles and bosonic antiparticles. In 3D-RQM symmetries, the rest of the terms present the topological effect of the deformation space-space (TDSS) on the thesis's main energies $E_{nl}^{hp\pm}$.

(2). If we choose, $\alpha = \dfrac{1}{R}$, $q = \exp\left(\dfrac{\theta}{R}\right)$ and $V_0 \to q V_0 = \exp\left(\dfrac{\theta}{R}\right)$ in Eq. (1), we obtain the improved Woods-Saxon potential (WSP), the global relativistic energy for the bosonic particles E_{nc}^{wp-p} (or bosonic antiparticles E_{nc}^{wp-ap}) under the improved WSP in 3D-ERQM symmetries as:

$$
\begin{cases}
V_{ws}(r_{nc}) = V_{ws}(r) + \dfrac{\dfrac{V_0}{2R} \exp\left(\dfrac{r-\theta}{R}\right)}{r\left(1 - \exp\left(\dfrac{r-\theta}{R}\right)\right)^2} \mathbf{L}\Theta \\[5mm]
E_{nc}^{wp} = E_{nl}^{wp\pm} \pm \left[\langle K \rangle_{(nlm)}^{wp} \left(\Lambda(\aleph\Omega)m + \Theta F \right) \right]^{1/2}
\end{cases}
, \tag{30}
$$

where V_0, θ and R are the potential depth, the width of the potential, and the surface thickness whose values correspond to the ionization energies, respectively, $V_{ws}(r)$ present the standard WSP [52] while the rest terms give the influences of TDSS on the standard WSP, $\langle K \rangle_{(nlm)}^{wp}$ obtained from $\langle K \rangle_{(nlm)}^{hp}$ with $(V_0, \alpha) \to (q V_0, \frac{1}{R})$. The first two parts $E_{nl}^{wp\pm}$ in RHS of Eqs. (30) describe the relativistic energy of bosonic particles and bosonic antiparticles within the framework of 3D-RQM while the rest terms are present in the TDSS on the thesis's main energies $E_{nl}^{wp\pm}$ which are obtained from making these substitutes.

5. SE WITH PDM-ID(H-TP) MODES IN 3D-ENRQM SYMMETRIES

To realize a study of the nonrelativistic limit, in 3D extended nonrelativistic QM (3D-ENRQM) symmetries, for the PDM-ID(H-TP) models, two steps must be applied. The first corresponds to the NR limit, in 3D-NRQM symmetries. This is done by applying the following simultaneous replacements, ($E_{nl} + m_0$ and $E_{nl} - m_0$) by ($2m_0$ and E_{nl}^{nr}),

respectively in addition to the setv $S_0 = S_1 = 0$. After straightforward calculation, we can obtain the NR-energy equation for PDM-D(H-TP) models as:

$$E_{nl}^{nr} = -\frac{\left(\dfrac{\omega_3^{nr} q^2 - \omega_1^{nr}}{2\alpha\sigma^{nr}} + 2\alpha\left(n + \sigma^{nr}\right)\right)^2}{8q^2\left(m_0 - V_1\right)} + V , \tag{31}$$

with σ_{nr} and V are equal $\dfrac{q}{2}\left(1 + \sqrt{1 - \dfrac{\rho^{nr}}{\alpha^2 q^2}}\right)$ and $\dfrac{2V_0 V_1 + 2m_0 m_1 + V_1^2 + m_1^2}{2\left(m_0 - V_1\right)}$, respectively, while:

$$\begin{cases} \omega_1^{nr} = 2qE_{nl}^{nr} V_0 - 2q^2 E_{nl}^{nr} V_1 - V_0^2 + q^2 V_1^2 \\ \omega_2^{nr} = -2E_{nl}^{nr} V_0 + 2qV_0 V_1 - 2qm_0 m_1 + 4l\left(l+1\right)\alpha^2 \\ \omega_3^{nr} = 2E_{nl}^{nr} V_1 + 2\left(m_0 - V_1\right)V \end{cases} , \tag{32}$$

with

$$\rho^{nr} = q^2 \omega_3^{nr} - \omega_1^{nr} - q\omega_2^{nr} .$$

Now, under the conditions of NR-limit, the new NR-expectation values $B_{(nlm)}^{1ht}$, $B_{(nlm)}^{2ht}$, $B_{(nlm)}^{3ht}$, $B_{(nlm)}^{4ht}$ and $B_{(nlm)}^{5ht}$ are obtained from the expectation values $A_{(nlm)}^{1ht}$, $A_{(nlm)}^{2ht}$, $A_{(nlm)}^{3ht}$, $A_{(nlm)}^{4ht}$ and $A_{(nlm)}^{5ht}$, by setting $S_0 = S_1 = 0$ and $k \to l$ in Eq. (20). As a direct consequence, the new NR improved energy E_{nc-nl}^{nr-ht} of the excited state $(n,l,m)^{th}$ in 3D-ENRQM symmetries under the PDM-ID(H-TP) models equals the NR-energy E_{nl}^{nr} in Eq. (31) under PDM-D(H-TP) models plus the NR corrections which are generated with the effect of deformation space-space, as:

$$E_{nc-nl}^{nr-ht} = E_{nl}^{nr} + \left[\left\langle K\right\rangle_{(nlm)}^{nr-ht}\left(\Lambda\left(\aleph,\Omega\right)m + \Theta F\right)\right]^{1/2} , \tag{33}$$

where

$$\left\langle K\right\rangle_{(nlm)}^{nr-ht} = \sum_{\alpha=1}^{5} \beta_\alpha^{nr} B_{(nlm)}^{\alpha ht} .$$

6. Spin-averaged mass spectra of HLM under PDM-ID(H-TP) modes

The quark-antiquark interaction potentials, are spherically symmetrical and provide a good description of HLM such as $c\bar{c}$ and $b\bar{b}$ under PDM-ID(H-TP) modes. This would give us a strong incentive to dedicate this section to the purpose to determine the modified spin-averaged mass spectra of HLM under the PDM-ID(H-TP) modes interaction by using the following formula:

$$+M_{nl}^{ht} = m_q + m_{\bar{q}} + E_{nl}^{nr} \Rightarrow M_{nc}^{ht} = m_q + m_{\bar{q}} + \begin{cases} \dfrac{1}{3}\sum_{\alpha=1}^{3} E_{nc}^{ht\alpha} & \text{for } spin\text{-}1 \\ E_{nc}^{ht} & \text{for } spin\text{-}0 \end{cases} . \tag{34}$$

The LHS of Eq. (34) describes spin-averaged mass spectra of *HLM* in usual QM symmetries [53-57], while the RHS is our self-generalization to this formula in 3D-ENRQM symmetries, m_q and $m_{\bar{q}}$ are the quark mass and the antiquark mass, M_{nl}^{ht} is the spin-averaged mass spectra of *HLM* under the mass-dependent SE with the vector quark-antiquark interaction in usual NRQM symmetries, E_{nl}^{nr} is the nonrelativistic energy under PDM-ID(H-TP) modes, which is determined by generalizing Eq. (33) while (E_{nc}^{ht1}, E_{nc}^{ht2} and E_{nc}^{ht3}) are the modified energies of *HLM* which have spin-1 while E_{nc}^{ht} is the modified energies of *HLM* that have spin-0. We need to replace the factor $F(j,l,s)$ with new generalized values as follows:

$$F = \begin{cases} \dfrac{l}{2} & \text{for } \left(j = l+1, s = 1\right) \\ -1 & \text{for } \left(j = l, s = 1\right) \\ -(l+1) & \text{for } \left(j = l-1, s = 1\right) \\ 0 & \text{for } \left(j = l, s = 0\right) \end{cases} . \tag{35}$$

The modified energies (E_{nc}^{ht1}, E_{nc}^{ht2}, E_{nc}^{ht3} and E_{nc}^{ht}) correspond to Eq. (35) and can be expressed by the following formula:

$$\begin{cases} E_{nc}^{ht1} = E_{nl}^{nr} + \left[\langle K \rangle_{(nlm)}^{nr-ht} \left(\Lambda\left(\aleph\Omega\right)m + \frac{\Theta l}{2} \right) \right]^{1/2} \\ E_{nl}^{ht2} = E_{nl}^{nr} + \left[\langle K \rangle_{(nlm)}^{nr-ht} \left(\Lambda\left(\aleph\Omega\right)m - \Theta \right) \right]^{1/2} \\ E_{nl}^{ht3} = E_{nl}^{nr} + \left[\langle K \rangle_{(nlm)}^{nr-ht} \left(\Lambda\left(\aleph\Omega\right)m - \Theta(l+1) \right) \right]^{1/2} \\ E_{nc}^{ht} = E_{nl}^{nr} + \left[\langle K \rangle_{(nlm)}^{nr-ht} \Lambda\left(\aleph\Omega\right)m \right]^{1/2} \end{cases} \qquad (36)$$

By substituting Eqs. (36) and (35) into Eq. (34), the new mass spectrum of the HLM systems in 3D-ENRQM symmetries under the PDM-ID(H-TP) models for any arbitrary radial and angular momentum quantum numbers becomes:

$$M_{nc}^{ht} = M_{nl}^{ht} + \begin{cases} \left\langle E_{nc}^{ht} \right\rangle_{np} & \text{For spin} -1 \\ \left(\langle K \rangle_{(nlm)}^{nr-ht} \right)^{1/2} \left[\left(\tau\aleph + \chi\Omega \right)m \right]^{1/2} & \text{For spin} -0 \end{cases}, \qquad (37)$$

with $\left\langle E_{nc}^{ht} \right\rangle_{np}$ mean physically the value of the nonpolarized energy which takes into account different all spin values:

$$\left\langle E_{nc}^{ht} \right\rangle_{np} = \frac{\left(\langle K \rangle_{(nlm)}^{nr-ht} \right)^{1/2}}{3} h\left(\Theta, \tau, \chi, m, l \right), \qquad (38)$$

and $h\left(\Theta, \tau, \chi, m, l \right)$ is given by:

$$h\left(\Theta, \tau, \chi, m, l \right) = \left[\left[\left(\left(\tau\aleph + \chi\Omega \right)m + \Theta l/2 \right) \right]^{1/2} + \left[\left(\left(\tau\aleph + \chi\Omega \right)m - \Theta \right) \right]^{1/2} + \left[\left(\left(\tau\aleph + \chi\Omega \right)m - \Theta(l+1) \right) \right]^{1/2} \right]. \quad (39)$$

It is important to notice that the new function $h\left(\Theta, \tau, \chi, m, l \right)$ describe the topological defect de deformation space-space because it disappears in the absence of the non-commutativity parameters (Θ, τ, χ). The LHS of Eq. (37) is the spin-averaged mass spectra M_{nl}^{ht} of *HLM* under the PDM-D(H-TP) modes in 3D-NRQM symmetries and the RHS is produced with the effect of deformation space-space which is sensitive to the atomic quantum numbers (n, l, j, s, m) and potential depths (V_0, S_0, V_1, S_1).

7. CONCLUSIONS

This paper presents an approximate analytical solution of the 3D-ERQM and 3D-ENRQM symmetries with PDM-SVID(H-TP) and PDM-ID(H-TP) models using the parametric Bopp shift method and standard perturbation theory. Under the deformed features of space-space, we found new bound-state energies that appear sensitive to quantum numbers (n, j, l, s, m), the mixed potential depths (V_0, S_0, V_1, S_1), the rest and perturbed mass (m_0, m_1), the screening parameter's inverse α, and the noncommutativity parameter (Θ, τ, χ). Moreover, the nonrelativistic limit of the studied potential in 3D-ENRQM symmetries has been investigated. The modified spin-averaged mass spectra of *HLM* in both 3D-NRQM (commutative space CS) and 3D-ENRQM symmetries were determined by applying our results of the new nonrelativistic energies that represent the binding energy between the quark and antiquark. We have treated certain significant particular instances that we hope will be valuable to the specialized researcher such as the improved GHP and the improved WSP in the context of 3D-ERQM symmetries. It is shown that the PDM-SVID(H-TP) model in a 3D-ERQM has a behavior similar to the dynamics of bosonic particles and bosonic antiparticles under the PDM with PDM-SVD(H-TP) in a 3D-RQM symmetry (CS) influenced by the effect of constant magnetic field and a self-rotational which can be similar to the behavior of coupling to spin-orbit. As a result, the dynamics of PDM-SVID(H-TP) models in a 3D-ERQM symmetry under the DKGE are similar to the dynamics of a particle in a 3D-RQM symmetry under the Duffin-Kemmer equation which describes bosonic particles with spin-1.

ORCID IDs
Ⓞ**Abdelmadjid Maireche,** https://orcid.org/0000-0002-8743-9926

REFERENCES

[1] C.A. Onate, A.N. Ikot, M.C. Onyeaju, and M. E. Udoh, "Bound state solutions of D-dimensional Kleine-Gordon equation with hyperbolic potential", Karbala International Journal of Modern Science, **3**(1), 1 (2017). https://doi.org/10.1016/j.kijoms.2016.12.001

[2] U. S. Okorie, A. N. Ikot, C.O. Edet, I.O. Akpan, R. Sever, and R. Rampho, "Solutions of the Klein Gordon equation with generalized hyperbolic potential in D-dimensions", Journal of Physics Communications, **3**, 095015 (2019). https://doi.org/10.1088/2399-6528/ab42c6

[3] H. Hassanabadi, S. Zarrinkamar, and H. Rahimov, "Approximate Solution of D-Dimensional Klein—Gordon Equation with Hulthén-Type Potential via SUSYQM", Commu. Theor. Phys. **56**(3), 423 (2011). https://doi.org/10.1088/0253-6102/56/3/05

[4] U.P., bogo, O.E., Ubi, C.O., Edet, and A. N., Ikot, "Effect of the deformation parameter on the nonrelativistic energy spectra of the q-deformed Hulthen-quadratic exponential-type potential", Eclética Química, **46**(4), 60 (2021). https://doi.org/10.26850/1678-4618eqj.v46.4. 2021.p60-73

[5] I.B. Okon, O. Popoola, C.N. Isonguyo, and A.D. Antia, "Solutions of Schrödinger and Klein-Gordon Equations with Hulthen Plus Inversely Quadratic Exponential Mie-Type Potential", Physical Science International Journal, **19**(2), 1 (2018). https://doi.org/10.9734/PSIJ/2018/43610

[6] A.N. Ikot, H.P. Obong, T.M. Abbey, and S. Zare, "Bound and Scattering State of Position Dependent Mass Klein–Gordon Equation with Hulthen Plus Deformed-Type Hyperbolic Potential", Few-Body Systems, **57**(9), 807 (2016). https://doi.org/10.1007/s00601-016-1111-3

[7] L. Canderle, and A. Plastino, "De la Pe na approach for Position-dependent Masses", Sop transactions on theoretical physics, **1**(3), 99 (2014). https://doi.org /10.15764/TPHY.2014.03007

[8] A. Tas, O. Aydogdu, and M. Salti, "Dirac particles interacting with the improved Frost–Musulin potential within the effective mass formalism", Annals of Physics, **379**, 67 2017). https://doi.org/10.1016/j.aop.2017.02.010

[9] G. Bastard, *Wave Mechanics Applied to Semiconductor Heterostructures*, (Les Editions de Physique Halsted Press, France, 1988).

[10] F. Arias de Saavedra, J. Boronat, A. Polls, and A. Fabrocini, "Effective mass of one 4He atom in liquid 3He", Phys. Rev. B, **50**(6) 4248 (1994). https://doi.org/10.1103/PhysRevB.50.4248

[11] M. Barranco, M. Pi, S.M. Gatica, E.S. Hernández, and J. Navarro, "Structure and energetics of mixed 4He-3He drops", Phys. Rev. B, **56**(14), 8997 (1997). https://doi.org/10.1103/PhysRevB.56.8997

[12] P. Ring, and P. Schuck, *The Nuclear Many-Body Problem*", (Springer-Verlag, New York, 1980), pp. 211.

[13] L. Dekar, L. Chetouani, and T.F. Hammann, "An exactly soluble Schrödinger equation with smooth position-dependent mass", J. Math. Phys., **39** (5), 2551 (1998). https://doi.org/10.1063/1.532407

[14] E. Witten, Non-commutative geometry and string field theory", Nucl. Phys. B, **268**, 253 (1986). https://doi.org/10.1016/0550-3213(86)90155-0

[15] S. Doplicher, K., Fredenhagen, and J.E., Spacetime quantization induced by classical gravity, Roberts, Phys. Lett. B, **331**(1-2), 39 (1994). https://doi.org/10.1016/0370-2693(94)90940-7

[16] E. Witten, "Reflections on the Fate of Spacetime, Phys. Today, **49**(4), 24 (1996). https://doi.org/10.1063/1.881493

[17] A. Kempf, G. Mangano, and R.B. Mann, "Hilbert space representation of the minimal length uncertainty relation", Physical Review D, **52**(2), 1108 (1995). https://doi.org/10.1103/physrevd.52.1108

[18] R.J. Adler, and D.I. Santiago, On gravity and the uncertainty principal", Modern Physics Letters A, **14**(20), 1371 (1999). https://doi.org/10.1142/s0217732399001462

[19] T., Kanazawa, G., Lambiase, G., Vilasi, and A. Yoshioka, Noncommutative Schwarzschild geometry and generalized uncertainty principle", Eur. Phys. J. C, **79**, 95 (2019). https://doi.org/10.1140/epjc/s10052-019-6610-1

[20] F., Scardigli, Generalized uncertainty principle in quantum gravity from micro-black hole gedanken experiment", Phys. Lett. B, **452**(1-2), 39 (1999). https://doi.org/10.1016/S0370-2693(99)00167-7

[21] A. Maireche, "A New Approach to the Approximate Analytic Solution of the Three-Dimensional Schrödinger Equation for Hydrogenic and Neutral Atoms in the Generalized Hellmann Potential Model", Ukr. J. Phys. **65**(11), 987 (2020). https://doi.org/10.15407/ujpe65.11.987

[22] H.S., Snyder, "Quantiz'ed Syace-Time", Phys. Rev. **71**, 38 (1947). https://doi.org/10.1103/PhysRev.71.38

[23] A., Connes, and J., Lott, "Particle models and noncommutative geometry. Nuclear Physics B - Proceedings Supplements, **18**(2), 29 (1991). https://doi.org/10.1016/0920-5632(91)90120-4

[24] A. Connes, *Noncommutative Geometry*, (Academic Press, 1994).

[25] N. Seiberg, E. Witten, N. Seiberg, and E. Witten, String theory and noncommutative geometry. Journal of High Energy Physics, **1999**(09), 032 (1999). https://doi.org/10.1088/1126-6708/1999/09/032

[26] A. Maireche, "A theoretical study of the modified equal scalar and vector Manning-Rosen potential within the deformed Klein-Gordon and Schrödinger in relativistic noncommutative quantum mechanics and nonrelativisc noncommutative quantum mechanics symmetries", Rev. Mex. Fis. **67**(5), 50702 (2021). https://doi.org/10.31349/revmexfis.67.050702

[27] A., Maireche, "Bound-state solutions of the modified Klien-Gordon and Shrodinger for arbitrary noncommutative quantum mechanics", J. Phys. Stud. **25**(1), 1002 (2021). https://doi.org/10.30970/jps.25.1002

[28] S. Aghababaei, and G. Rezaei, "Energy level splitting of a 2D hydrogen atom with Rashba coupling in non-commutative space", Commun. Theor. Phys. **72,** 125101 (2020). https://doi.org/10.1088/1572-9494/abb7cc

[29] J.F.G. Santos, "Heat flow and noncommutative quantum mechanics in phase-space", Journal of Mathematical Physics, **61**(12), 122101 (2020). https://doi.org/10.1063/5.001007

[30] H. Benzair, M. Merad, T. Boudjedaa, and A. Makhlouf, "Relativistic Oscillators in a Noncommutative Space: a Path Integral Approach", Zeitschrift Für Naturforschung A, **67**(1-2), 77 (2012). https://doi.org/10.5560/ZNA.2011-0060

[31] B. Mirza, and M. Mohadesi, "The Klein-Gordon and the Dirac Oscillators in a Noncommutative Space", Commun. Theor. Phys. (Beijing, China), **42**, 664 (2004). https://doi.org/10.1088/0253-6102/42/5/664

[32] H. Motavalli, and A.R. Akbarieh, "Klien-Gordon equation for the Coulomb potential in noncommutative space", Modern Physics Letters A, **25**(29), 2523 (2010). https://doi.org/10.1142/S0217732310033529

[33] M.R. Douglas, and N.A. Nekrasov, "Noncommutative field theory", Reviews of Modern Physics, **73**(4), 977 (2001). https://doi.org/10.1103/RevModPhys.73.977

[34] M. Chaichian, A. Demichev, and P. Prešnajder, "Quantum field theory on non-commutative space-times and the persistence of ultraviolet divergences", Nuclear Physics B, **567**(1-2), 360 (2000). https://doi.org/10.1016/S0550-3213(99)00664-1

[35] L. Mezincescu, "Star Operation in Quantum Mechanics", (2000). https://arxiv.org/abs/hep-th/0007046

[36] L. Gouba, "A comparative review of four formulations of noncommutative quantum mechanics", Int. J. Mod. Phys. A, **31**(19), 1630025 (2016). https://doi.org/10.1142/s0217751x16300258

[37] F. Bopp, "La mécanique quantique est-elle une mécanique statistique particulière", Ann. Inst. Henri Poincaré, **15**(2), 81 (1956). http://www.numdam.org/item/AIHP_1956__15_2_81_0.pdf

[38] A. Maireche, "The investigation of approximate solutions of Deformed Klein-Fock-Gordon and Schrödinger Equations under Modified Equal Scalar and Vector Manning-Rosen and Yukawa Potentials by using the Improved Approximation of the Centrifugal term and Bopp's shift Method in NCQM Symmetries", Lat. Am. J. Phys. Educ. **15**(2), 2310 (2021). https://dialnet.unirioja.es/descarga/articulo/8128006.pdf

[39] A. Maireche, "A Theoretical Model of Deformed Klein-Gordon Equation with Generalized Modified Screened Coulomb Plus Inversely Quadratic Yukawa Potential in RNCQM Symmetries", Few-Body Syst. **62**, 12 (2021). https://doi.org/10.1007/s00601-021-01596-2

[40] A. Maireche, "Modified unequal mixture scalar vector Hulthén-Yukawa potentials model as a quark-antiquark interaction and neutral atoms via relativistic treatment using the improved approximation of the centrifugal term and Bopp's shift method", Few-Body Syst. **61**, 30 (2020). https://doi.org/10.1007/s00601-020-01559-z

[41] A. Maireche, "The Klein-Gordon equation with modified Coulomb plus inverse-square potential in the noncommutative three-dimensional space", Mod. Phys. Lett. A, **35**(5), 052050015 (2020). https://doi.org/10.1142/s0217732320500157

[42] A. Maireche, "Heavy quarkonium systems for the deformed unequal scalar and vector Coulomb-Hulthén potential within the deformed effective mass Klein-Gordon equation using the improved approximation of the centrifugal term and Bopp's shift method in RNCQM symmetries", Int. J. Geo. Met. Mod. Phys. **18**(13), 2150214 (2021). https://doi.org/10.1142/S0219887821502145

[43] A. Maireche, "A new theoretical study of the deformed unequal scalar and vector Hellmann plus modified Kratzer potentials within the deformed Klein-Gordon equation in RNCQM symmetries", Mod. Phys. Lett. A, **36**(33), 2150232 (2021). https://doi.org/10.1142/S0217732321502321

[44] A. Maireche, "On the interaction of an improved Schiöberg potential within the Yukawa tensor interaction under the background of deformed Dirac and Schrödinger equations", Indian J Phys, **96**(10), (2022). https://doi.org/10.1007/s12648-022-02433-w

[45] A. Maireche, "Approximate Arbitrary (k,l) states solutions of deformed Dirac and Schrodinger equations with new generalized Schioberg and Manning-Rosen Potentials within the generalized tensor Interactions in 3D-EQM Symmetries", Int. J. Geo. Met. Mod. Phys. (2022). https://doi.org/10.1142/S0219887823500287

[46] A. Kurniawan, A. Suparmi, and C. Cari, "Approximate analytical solution of the Dirac equation withq-deformed hyperbolic Pöschl–Teller potential and trigonometric Scarf II non-central potential", Chinese Physics B, **24**(3), 030302 (2015). https://doi.org/10.1088/1674-1056/24/3/030302

[47] A.N. Ikot, H.P. Obong, T.M. Abbey, S. Zare, M. Ghafourian, and H. Hassanabadi, "Bound and Scattering State of Position Dependent Mass Klein–Gordon Equation with Hulthen Plus Deformed-Type Hyperbolic Potential", Few-Body Syst. **57**, 807 (2016). https://doi.org/10.1007/s00601-016-1111-3

[48] S.H. Dong, W.C. Qiang, G.H. Sun, and V.B. Bezerra, "Analytical approximations to the l-wave solutions of the Schrödinger equation with the Eckart potential", J. Phys. A: Math. Theor. **40**(34), 10535 (2007). https://doi.org/10.1088/1751-8113/40/34/010

[49] Y. Zhang, "Approximate analytical solutions of the Klein-Gordon equation with scalar and vector Eckart potentials", Phys. Scr. **78**(1), 015006-1 (2008). https://doi.org/10.1088/0031-8949/78/01/015006

[50] K. Bencheikh, S. Medjedel, and G. Vignale, "Current reversals in rapidly rotating ultracold Fermi gases", Phys. Lett. A, **89**(6), 063620-1-(2014). https://doi.org/10.1103/physreva.89.063620

[51] W. Gao-Feng, C. Wen-Li, W. Hong-Ying, and L. Yuan-Yuan, "The scattering states of the generalized Hulthén potential with an improved new approximate scheme for the centrifugal term", Chinese Physics B, **18**(9), 3663 (2009). https://doi.org/10.1088/1674-1056/18/9/010

[52] R.D. Woods, and D.S. Saxon, "Diffuse Surface Optical Model for Nucleon-Nuclei Scattering", Physical Review, **95**(2), 577 (1954). https://doi.org/10.1103/physrev.95.577

[53] M. Abu-Shady, T.A. Abdel-Karim, and S.Y. Ezz-Alarab, "Masses and thermodynamic properties of heavy mesons in the non-relativistic quark model using the Nikiforov–Uvarov method", J. Egypt Math. Soc. **27**, 14 (2019). https://doi.org/10.1186/s42787-019-0014-0

[54] R. Rani, S.B. Bhardwaj, and F. Chand, "Mass Spectra of Heavy and Light Mesons Using Asymptotic Iteration Method", Communications in Theoretical Physics, **70**(2), 179 (2018). https://doi.org/10.1088/0253-6102/70/2/179

[55] A. Maireche, "Analytical Expressions to Energy Eigenvalues of the Hydrogenic Atoms and the Heavy Light Mesons in the Framework of 3D-NCPS Symmetries Using the Generalized Bopp's Shift Method", Bulg. J. Phys. **49**(3), 239 (2022). https://doi.org/10.55318/bgjp.2022.49.3.239

[56] A. Maireche, "The investigation of approximate solutions of Deformed Schrödinger Equations for the Hydrogenic Atoms, Heavy Quarkonium Systems ($Q\overline{Q} = b\overline{b}$, $c\overline{c}$) and Diatomic molecule Bound-State Problem under Improved Exponential, Generalized, Anharmonic Cornell potential Model in NCPS symmetries", Lat. Am. J. Phys. Educ. **16**(2), 2304-1 (2022). https://dialnet.unirioja.es/descarga/articulo/8602824.pdf

[57] A., Maireche, " The Relativistic and Nonrelativistic Solutions for the Modified Unequal Mixture of Scalar and Time-Like Vector Cornell Potentials in the Symmetries of Noncommutative Quantum Mechanics", Jordan Journal of Physics, **14**(1), 59 (2021). https://doi.org/10.47011/14.1.6

РЕЛЯТИВІСТСЬКІ СИМЕТРІЇ БОЗОННИХ ЧАСТИНОК І АНТИЧАСТИНОК НА ФОНІ ПОЗИЦІЙНО-ЗАЛЕЖНОЇ МАСИ ДЛЯ ВДОСКОНАЛЕНОГО ДЕФОРМОВАНОГО ХЮЛЬТЕН ПЛЮС ПОКРАЩЕНОГО ПОТЕНЦІАЛУ ГІПЕРБОЛІЧНОГО ТИПУ У СИМЕТРІЯХ 3D-EQM

Абдельмаджид Майреше

Факультет фізики, Університет Мсіла, Лабораторія РМС, Університет Мсіла, Алжир

Розв'язання зв'язаного стану деформованого рівняння Клієна-Гордона були визначені в симетріях тривимірної розширеної релятивістської квантової механіки 3D-ERQM з використанням позиційно-залежної маси (PDM) з нерівним скалярним і векторним потенціалом для вдосконаленого деформованого Hulthén плюс покращеного потенціалу гіперболічного типу (PDM-SVID(H-TP)). PDM з нерівним скалярним і векторним потенціалом для моделей Hulthén плюс гіперболічний потенціал деформованого типу (PDM-(SVH-DTP)), а також комбінація радіальних членів, які пов'язані з $\mathbf{L\Theta}$, що пояснює взаємодію фізичного особливості системи з топологічними деформаціями простір-простір. Нові релятивістські власні значення енергії були отримані за допомогою параметричного методу зсуву Боппа та стандартної теорії збурень, яка чутлива до атомних квантових чисел (j,l,s,m), змішаних потенціальних глибин (V_0, S_0, V_1, S_1), спокою та збуреної маси (m_0, m_1), параметра екранування, зворотного параметру α, і параметрів некомутативності (Θ, τ, χ). У рамках симетрій 3D-ERQM ми розглянули певні важливі окремі випадки, які, як ми сподіваємося, будуть цінними для дослідників-спеціалістів. Ми також розглянули нерелятивістську межу та застосували наші отримані результати для створення мас-спектрів важких і легких мезонів (HLM), таких як $c\bar{c}$ та $c\bar{c}$ у рамках PDM-SE з покращеними деформованими моделями Hulthén плюс покращеного гіперболічного потенціалу (PDM ID(H-TP)). Коли було застосовано три одночасні обмеження (Θ, τ, χ), ми відновили нормальні релятивістські результати в літературі ($0,0,0$) для моделей PDM ID(H-TP).

Ключові слова: рівняння Клієна-Гордона, деформований Хультен плюс деформований гіперболічний потенціал, важкі-легкі мезони, Некомутативна квантова механіка та метод зсуву Боппа, Канонічна некомутативність

DETECTION OF LYSOZYME AMYLOID FIBRILS USING TRIMETHINE CYANINE DYES: SPECTROSCOPIC AND MOLECULAR DOCKING STUDIES†

Olga Zhytniakivska[a,*], Uliana Tarabara[a], Atanas Kurutos[b,c], Kateryna Vus[a], Valeriya Trusova[a], Galyna Gorbenko[a]

aDepartment of Medical Physics and Biomedical Nanotechnologies, V.N. Karazin Kharkiv National University
4 Svobody Sq., Kharkiv, 61022, Ukraine
bInstitute of Organic Chemistry with Centre of Phytochemistry, Bulgarian Academy of Sciences,
Acad. G. Bonchev str., bl. 9, 1113, Sofia, Bulgaria
cDepartment of Pharmaceutical and Applied Organic Chemistry, Faculty of Chemistry and Pharmacy
Sofia University St. Kliment Ohridski, 1 blv. J. Bourchier, Sofia, 1164, Bulgaria
*Corresponding Author: olga.zhytniakivska@karazin.ua

Due to their unique photophysical and photochemical properties and high sensitivity to the beta-pleated motifs, cyanine dyes are increasingly used as molecular probes for the identification and characterization of amyloid fibrils *in vitro* and the visualization of amyloid inclusions *in vivo*. In the present study the spectroscopic and molecular docking techniques have been employed to evaluate the amyloid sensitivity and the mode of interaction between the trimethine cyanine dyes and the native (LzN) and fibrillar (LzF) lysozyme. It was found that the trimethine association with non-fibrilar and fibrillar forms of lysozyme is accompanied by the changes in the dye aggregation extent. The molecular docking studies indicate that: i) the trimethines form the most stable complexes with deep cleft of the native lysozyme; ii) the dye binding to non-fibrillar protein is governed by the hydrophobic interactions, π-stacking contacts between aromatic or cyclopentane ring of the cyanine and Trp in position 63 or 108 and hydrogen bonds between the OH-groups of the trimethines and acceptor atoms of Asp 101 (AK3-7) and Gln 57 (AK3-8) of LzN; iii) cyanine dyes form the energetically most favorable complexes with the groove Gly 2-Leu 4/Ser 8-Trp 10 of the lysozyme fibril core; iv) cyanines-LzF interaction is stabilised by hydrophobic contacts, π-stacking interaction and hydrogen bonds. The dyes AK3-7, AK3-5 and AK3-11 were selected as the most prospective amyloid probes.
Keywords: Trimethine cyanine dyes, lysozyme, amyloid fibrils.
PACS: 87.14.C++c, 87.16.Dg

During the last decades, cyanine dyes have found numerical applications in a variety of research areas including bioanalysis, pharmacology, medicine, optoelectronics, photoelectrochemistry, laser technologies, etc. [1-6]. Likewise, these probes appeared to be especially useful for the detection of the disease-related protein aggregates, amyloid fibrils, due to their advantages such as i) long wavelength absorption and emission maxima [7,8]; ii) dependence of the cyanine photophysical properties on the protein environment resulting from the flexibility of the polymethine chain in their structure [9, 10]; iii) significant enhancement of fluorescence emission upon binding to amyloid fibrils [11-13]; iv) the characteristic fluorescence turn-on mechanism in the presence of aggregated proteins [14,15]; v) the ability to form self-assembled supramolecular complexes [15-17], vi) rather high amyloid sensitivity and specificity of cyanines [10,13,14]. More specifically, cyanine dyes were effectively used for: i) *in vivo* fluorescence imaging of amyloid β-plaques [11,18]; ii) monitoring the fibrillation kinetics of amyloidogenic proteins [12]; iii) preventing and modulating protein fibrillization [16,19], to name only a few.

Recently, we have reported the ability of trimethine cyanine compounds to detect the insulin amyloid fibrils [15]. Briefly, based on the comprehensive analysis of the spectral characteristics of trimethines in the buffer solution and in the presence of control and fibrillar insulin we demonstrated that the dyes under study are capable of distinguishing between the non-aggregated and fibrillar insulin [15]. Moreover, the dye AK3-11 was selected as the most effective amyloid sensor among the studied cyanines due to conversion of the AK3-11 non-emissive assemblies in aqueous solution and non-fibrillized insulin to the highly fluorescent monomeric species in the presence of the fibrillar insulin [15]. Furthermore, we demonstrated that these trimethine derivatives possess the potency to interfere with the insulin aggregation [19]. However, all the above studies were performed using the insulin as a model protein. Besides we didn't evaluate the influence of protein charge and hydrophobicity on the amyloid-sensing potential of the cyanine dyes. To fill this gap, the aim of the present study to investigate the interactions between the trimethine cyanine dyes and the lysozyme amyloid fibrils using the spectroscopic and molecular docking techniques. More specifically, we concentrated our efforts on characterizing both the spectral responses and the potential binding sites of the cyanines in the presence of fibrillar and non-aggregated lysozyme.

MATERIALS AND METHODS
Materials

Egg yolk lysozyme (Lz) was purchased from Sigma, USA. The trimethine cyanine dyes (Figure 1) were synthesized at the University of Sofia, Bulgaria, as described previously [15]. All other reagents were of analytical grade and used without further purification.
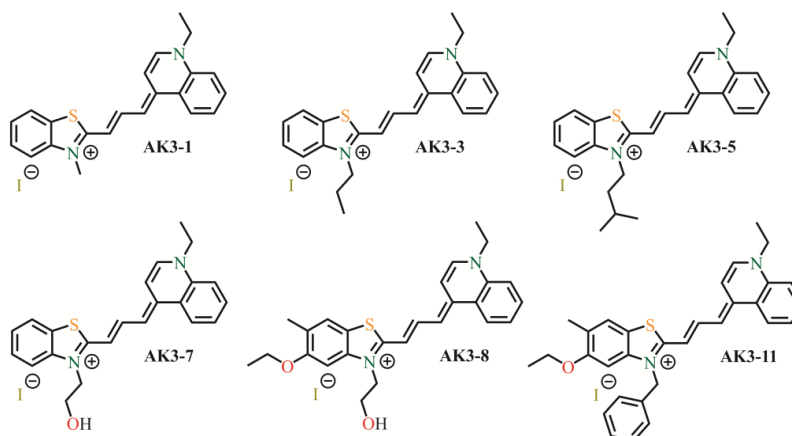
Figure 1. Structural formulas of the trimethine cyanine dyes

Preparation of working solutions

The stock solutions of the examined trimethine cyanine dyes were prepared immediately before measurements by dissolving the dyes in dimethyl sulfoxide. The concentrations of the dyes were determined spectrophotometrically, using their extinction coefficients [15]. The lysozyme stock solution (10 mg/ml) was prepared by dissolving the protein in 10 mM glycine buffer (pH 2.0). This solution was used as reference for non-aggregated protein (LzN). The amyloid fibrils of lysozyme were prepared by the protein incubation in 10 mM glycine buffer at pH 2 and 60°C for 14 days. The amyloid nature of the protein aggregates was confirmed by ThT assay and the transmission electron microscopy. Hereafter, the fibrillar lysozyme is designated as LzF.

Spectroscopic measurements

The steady-state fluorescence spectra were collected on a FL-6500 spectrofluorimeter (Perkin-Elmer Ltd., Beaconsfield, UK) at 20°C with excitation wavelength 590 nm using the 10 mm path-length quartz cells. The excitation and emission slit widths were set at 10 nm. To record the fluorescence spectra of the cyanines in the dye-protein complexes, the appropriate amounts of the stock solutions of the non-aggregated or fibrillar lysozyme were added to each dye in 5 mM sodium phosphate buffer (pH 7.4).

The absorption spectra of the dyes were acquired on Shimadzu UV-2600 Spectrophotometer (Japan) at 25°C using 10-mm path-length quartz cuvettes. To measure the absorption spectra of cyanine dyes in the aqueous phase or in the complexes with lysozyme, appropriate amounts of the stock dye solutions in DMSO were added either to 5 mM sodium phosphate buffer (pH 7.4) or directly to the working protein solutions and were incubated for one hour. The deconvolution of the dye absorption spectra was performed in the Origin 9.0 (OriginLab Corporation, Northampton, USA) using the log-normal asymmetric function (LN) [20]:

$$A = A_{max} \exp\left[-\frac{ln2}{\ln^2(\rho)} \ln^2\left(\frac{a-v}{a-v_c}\right) \right] \tag{1}$$

where A denominates the absorbance, A_{max} is the maximum absorbance, v is the wavenumber, v_c is the peak position, ρ expresses the asymmetry of the function defined as:

$$\rho = \frac{v_c - v_{min}}{v_{max} - v_c} \tag{2}$$

where v_{min} and v_{max} represent the wavenumber values at half-absorbance. The parameter a designates the limiting wavenumber:

$$a = v_c + \frac{(v_{max} - v_{min}) \cdot \rho}{\rho^2 - 1} \tag{3}$$

Molecular docking studies

To define the most energetically favorable binding sites for the examined dyes on the lysozyme amyloid fibrils, the molecular docking studies were performed using the the AutoDock (version 4.2) incorporated in the PyRx software (version 0.8) [21]. To further characterize the nature of the dye-protein interactions, the protein-ligand interaction profiler PLIP was used [22]. The dye structures were built in MarvinSketch (version 18.10.0) and optimized in Avogadro (version 1.1.0) [23,24].The crystal structures of hen egg white lysozyme (PDB ID: 3A8Z) was taken from the Protein Data Bank. The lysozyme model fibril was built from the K-peptide, GILQINSRW (residues 54–62 of the wild-type protein), using the CreateFibril tool as described previously [25].

RESULTS AND DISCUSSION

Fluorescence spectra of trimethines in the unbound state and in the presence of the native and fibrillar lysozyme are presented in Figure 2.
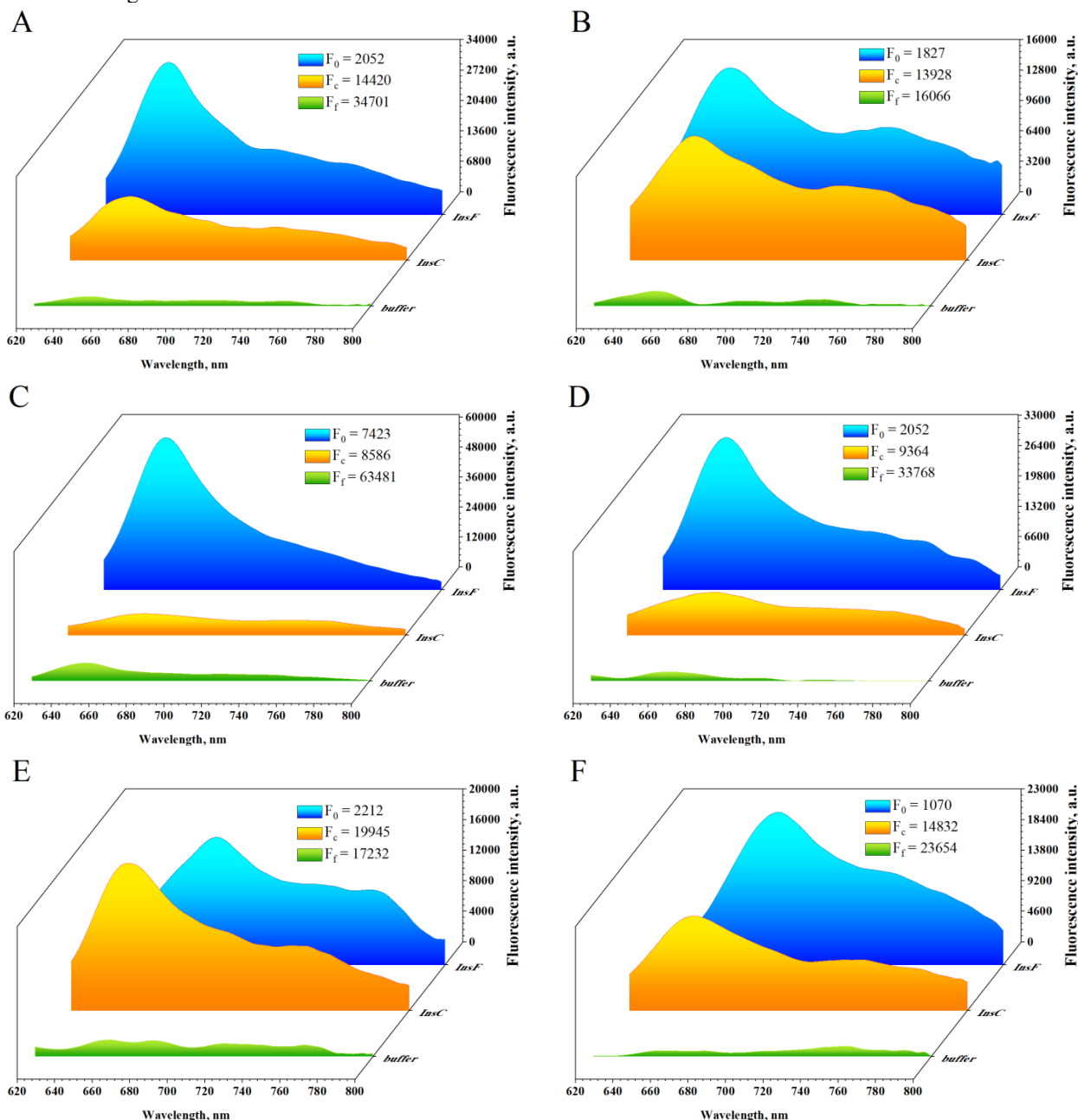

Figure 2. Fluorescence response of trimethine cyanine dyes to the non-fibrillar and fibrillar lysozyme. The dye and protein concentrations were 0.5 μM and 3.4 μM, respectively.

The photophysical properties of the examined cyanines in the buffer solution were examined previously and summarized in the Table 1. Specifically, the trimethines AK3-1, AK3-3, AK3-5 and AK3-7 exhibit a negligible fluorescence in buffer solution with the emission maxima located between 640 and 651 nm, depending on the dye chemical structure [15]. Besides, trimethines AK3-8 and AK3-11 are characterized by a negligible fluorescence intensity in buffer and do not show clear emission and excitation maxima [15]. The addition of the non-fibrillar lysozyme to the AK31, AK33, AK38 and AK3-11 in the buffer solution was accompanied by a significant enhancement of the dye fluorescence intensity along with a slight bathochromic shift (1-6 nm) of the excitation and emission maxima. In turn, the association of AK3-5 and AK3-7 with LzN was followed by a slight fluorescence increase coupled with a ~ 70-nm shift of the dye excitation maxima to the shorter wavelengths. Simultaneously, a ~ 15 nm bathochromic shift of the AK3-5 and AK3-7 emission maxima was observed in the presence of non-fibrillar lysozyme. As shown in Figure 2 and Table 1, the spectral response of the trimethine dyes (except AK3-8) to the fibrillar lysozyme lies in a strong increase of the dye fluorescence (I_f) as opposed to that in buffer (I_0) and in the presence of nonfibrillar protein (I_n), with a magnitude of

the fluorescence intensity increase depending on the dye chemical structure. The fluorescence maxima of the trimethines are shifted by approximately 9-15 nm towards longer wavelengths compared to those observed either in the non-aggregated proteins or in the buffer solution, as illustrated in Table 1.

Table 1. Spectral characteristics of the trimethine cyanine dyes in the presence of native and fibrillar lysozyme

Dye	Free dye			Control protein			Fibrillar protein			
	λ_{ex} (nm)	λ_{em} (nm)	F_0, (a.u.)	λ_{ex} (nm)	λ_{em} (nm)	F_c, (a.u.)	λ_{ex} (nm)	λ_{em} (nm)	F_f, (a.u.)	ADF
AK3-1	627	644	3470	627	653	14420	640	654	34701	5.84
AK3-3	626	646	1827	634	656	13928	637	656	16066	1.17
AK3-5	631	645	7423	559	661	8586	635	653	63481	7.39
AK3-7	628	642	2052	559	661	9364	634	654	33768	11.90
AK3-8	n.d.*	651	2212	625	650	19945	668	676	17232	-1.22
AK3-11	n.d.*	658	1070	630	656	14832	668	677	23654	8.24

λ_{ex} – maximum of the excitation spectra; λ_{em} –maximum of the emission spectra; n.d.[a] – not determined because of negligible fluorescence intensity; I_0, I_n, and I_f – fluorescence intensity of the dyes in buffer and in the presence of control and fibrillar proteins, respectively

By analogy with the insulin model protein, we determine the specificity of the examined trimethines also to the lysozyme amyloid fibrils. Therefore, we calculated the amyloid detection factor (ADF) (Table 1) characterizing the ability of a dye to selectively detect the fibrillar state over its native structure relative to the background fluorescence of the dye in buffer [15, 26]:

$$ADF = \frac{I_f - I_n}{I_0}. \tag{4}$$

It appeared that the trimethines under study (except AK3-8) are characterized by the positive ADF values in the presence of the fibrillar lysozyme, being indicative of their higher sensitivity to the fibrillar protein aggregates compared to the non-aggregated state. Although the enchanced fluorescence was observed for AK3-8 in the presence of LzF, the magnitude of fluorescence intensity increase was higher in the presence of monomeric lysozyme, as judged from the negative amyloid detection factor for this dye. In the presence of lysozyme fibrils the amyloid specificity was found to decrease in the row AK3-7 → AK3-11→ AK3-5 → AK3-1 → AK3-3→ AK3-8. It appeared that AK3-7, possessing the lowest sensitivity to the insulin amyloid fibrils [15], has demonstrated the largest ADF value in the presence of the lysozyme amyloid fibrils. The relatively high amyloid detection factors were observed in the presence of lysozyme for AK3-11 and AK3-5 dyes. Remarkably, these dyes were highly sensitive also to the insulin amyloid fibrils [15]. However, the ADF values of the trimethines were found to be significantly higher in the presence of insulin amyloid fibrils (ADF values exceeded 15 for all cyanines except AK3-7 in the presence of insulin fibrils [15]) compared to lysozyme, suggesting a sensitivity of the examined cyanines to the fibril morphology.

To interpret the observed fluorescence responses and the binding data of the cyanine dyes, in the following studies we analyzed their absorption spectra free in buffer solution as well as in the presence of control and fibrillar protein (Figure 3). For a more detailed analysis (by analogy with the data obtained for the insulin fibrils), we performed the decomposition of these absorption spectra using the log-normal asymmetric function (Eq. 1) [20].

The absorption spectra of AK3-5 and AK3-3 in buffer solution were represented as a sum of two separate bands, with a short-wavelength and long-wavelength spectral components corresponding to the dimeric and monomeric dye species, respectively. The corresponding absorption spectra of AK3-1, AK3-7, AK3-8 and AK3-11 in aqueous phase were deconvoluted into three bands representing the dye monomers, dimers and higher order aggregates (Figure 4). The deconvolution of the absorption spectra allowed us to calculate a set of parameters, viz.: i) the amplitude A_{max} (Table 2): i) the peak position ν_c, related to the environmental polarity [20] (Table 3); ii) the full width at half-maximum of the band (FWHM) (Table 4); and iii) the peak asymmetry parameter ρ (Table 5).

Table 2. The amplitude of the bands in the absorption spectra of cyanines

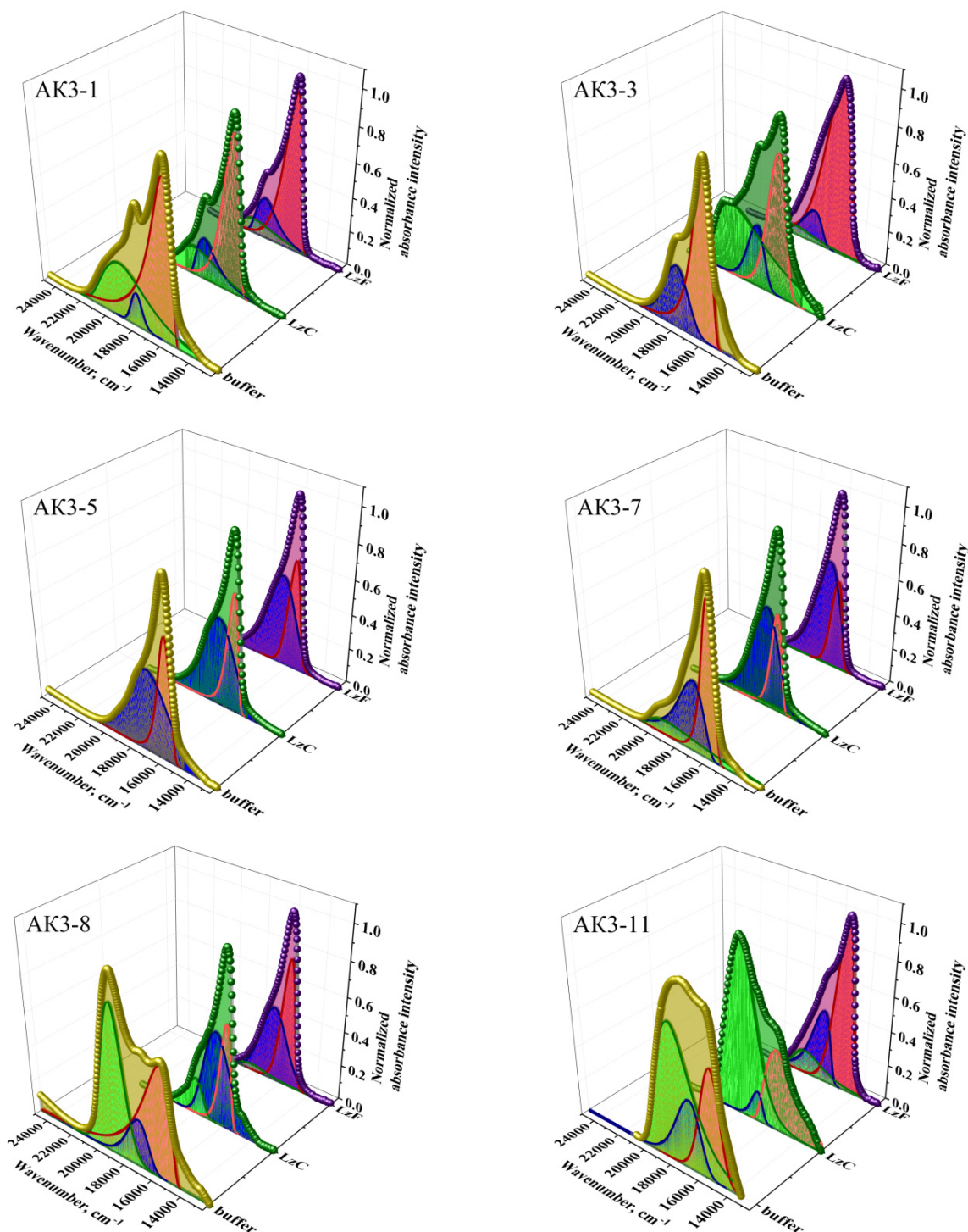|	Band	AK3-1	AK3-3	AK3-5	AK3-7	AK3-8	AK3-11
buffer	I	40000	97000	50000	84168	20739	15353
solution	II	8500	35171	33680	39000	8816	9711
	III	14000	-	-	8000	27500	18934
LzN	I	43112	22100	70503	50720	27768	14355
	II	11652	9935	52474	52102	24562	5360
	III	7895	11434	-	2224	9627	30784
LzF	I	52327	32383	74203	46437	44261	53443
	II	13891	6468	60928	54887	25834	22866
	III	4918	1757	-	39	2091	7296

Figure 3. Deconvolution of trimethines absorption spectra in buffer solution and in the presence of the non-fibrillar and fibrillar lysozyme. Band I is marked red, band II – blue, band III – green.

The incubation of AK3-1, AK3-5 та AK3-8 (Table 2) with the non-fibrillar lysozyme resulted in the following changes of the amplitude of the bands in comparison with those observed in the buffer solution: i) the rise in the amplitude of the bands I (a 1.1-fold, 1.4-fold and 1.3-fold increase) and II (a 1.4-fold, 1.6-fold and 2.8-fold increase); ii) the drop of the amplitude of the band III for AK3-1 (1.8 times) та AK3-8 (2.9 times) and the band narrowing; iii) a 3.3-fold, 1.7-fold and 1.1-fold decrease in the amplitude of the band I for AK3-3, AK3-7 and AK3-11, respectively; iv) the rise in the amplitude of the bands II (AK3-7) and band III (AK3-11). It should be noted that the absorption spectra of AK3-3 in the non-fibrillar lysozyme were deconvoluted into three separate bands, where for the short- (dimeric dye form) and long-wavelength (monomeric dyes form) bands the 3.5-fold and 4.4-fold drop of the amplitude was observed. Likewise, the incubation of AK3-3 with the non-fibrillar lysozyme resulted in the appearance of the III short-wavelength band of H-aggregates, the intensity of which even exceeded the amplitude of the band II.

Table 3. The position of the band (ν_c, cm^{-1}) in the buffer solution and in the presence of non-fibrillar and fibrillar lysozyme

Dye	Band	buffer solution	LzN	LzF
AK3-1	I	16007	16024	15924
	II	18100	18056	17943
	III	19300	18780	18764
AK3-3	I	15900	15608	15516
	II	17900	17025	17115
	III	-	18858	18434
AK3-5	I	15900	15858	15778
	II	17200	16930	16692
AK3-7	I	15900	15888	15854
	II	17000	16636	16494
	III	19000	18921	19000
AK3-8	I	15700	15871	15681
	II	17300	16622	16717
	III	19100	18041	18302
AK3-11	I	15550	15691	15100
	II	17000	16934	16500
	III	18300	18289	17800

Furthermore, while comparing the ν_c values (Table 3), it can be seen that monomeric lysozyme produced a hypsochromic shift of the monomer band I (AK3-3), dimer band II (all dyes except AK3-1), and the H-aggregates band III (AK3-1, AK3-7 and AK3-8). In turn, the position of the band I for AK3-8 та AK3-11 shifted to the higher wavenumbers. Moreover, the incubation of AK3-1, AK3-5 та AK3-8 with the LzN resulted in the increase of the asymmetry parameter (Table 5) and the full width at half-maximum (Table 4) of the band II (AK3-1 and AK3-7). In the meantime, the presence of the non-fibrillar lysozyme led to the decrease of the full width at half-maximum of the band I (Table 4). Taken together, we can conclude that the trimethine dyes AK3-1, AK3 5, AK3-7 and AK3-8 bind to the native lysozyme mainly in the form of monomers and dimers, while AK3-3 and AK3-11 show a tendency to aggregate in the presence of the non-fibrillar lysozyme.

The deconvolution of the absorption spectra of the trimethine dyes demonstrated that the dominating dye species in the presence of the lysozyme fibrils are the dye monomers and dimers. More specifically, the incubation of AK3-1, AK3-5, AK3-8 та AK3-11 with the fibrillar protein resulted in a 1.3, 1.8, 2.1 and 3.5-fold increase of the relative integral intensities of the band I along with 1.6, 1.5, 2.9 and 2.4-fold enhancement of the amplitude of the band II, respectively (Table 2). This effect was accompanied by the drop of the amplitude of the band III for AK3-1 (2.8 times), AK3-8 (13 times) та AK3-11 (2.6 times) (Table 2). At the same time, it can be seen that the lysozyme fibrils produced a significant attenuation in FWHM of the band I (AK3-1, AK3-5, AK3-8 та AK3-11) and band II (AK3-5, AK3-11), whereas in the case of AK3-1 and AK3-8 this parameter showed a slight increase for the bands II (AK3-1, AK3-8) and III (AK3-8) (Table 4).

Table 4 The full width at half-maximum of the band (FWHM, cm-1) in the buffer solution and in the presence of non-fibrillar and fibrillar lysozyme

Dye	Band	Buffer solution	LzC	LzF
AK3-1	I	1767	1314	1405
	II	910	1647	1747
	III	3795	3378	2931
AK3-3	I	1422	1436	2077
	II	2000	1383	1623
	III	-	4544	2183
AK3-5	I	1000	891	979
	II	3251	2696	2471
AK3-7	I	1000	862	883
	II	2159	2243	2185
	III	4803	10385	3448
AK3-8	I	2347	863	1052
	II	1750	2138	2181
	III	1832	1461	2054
AK3-11	I	1582	2256	1353
	II	2027	922	1568
	III	2935	2475	2356

This effect was accompanied by the lowered ν_c values of the bands I and II for AK3-1, AK3-5 and AK3-11 presumably arising from the reduced environmental polarity of the dye monomers and dimers associated with the fibrillar lysozyme (Table 3). On the contrary, the insulin fibrils did not exert influence on the position of the band III for AK3-1, AK3-8 and AK3-11. Remarkably, the higher amplitude increase of he band I for AK3-5 and AK3-11 indicates that the

binding of monomers is more favorable for these dyes. The complexation of AK3-3 with the fibrillar lysozyme, similar to the non-aggregated protein, led to the rise of the relative contribution of the bands III and II to the overall spectrum (Table 2). Besides, the relative integral intensities of the bands II and III were 1.5 and 6.5 times lower than those observed in the presence of the non-aggregated lysozyme. Moreover, the incubation of AK3-3 with the lysozyme fibrils resulted in a 1.5-fold increase of the monomer band. This effect was accompanied by the lowered ν_c values of the band I. Taken together, the above findings indicate that AK3-3 binds to the lysozyme amyloid fibrils presumably in the form of monomers. The incubation of AK3-7 with the fibrillar lysozyme resulted in the significant drop of the amplitude of the bands II and III in comparison with those observed in the buffer and control protein. The band III corresponding to the dye H-aggregates was almost indistinguishable. Furthermore, the enhancement of the amplitude of the band I along with the lowered ν_c values of the band I indicate that bound monomers are the dominating dye species in the presence of the lysozyme fibrils.

Table 4. The asymmetry of the function (ρ , cm^{-1})) in the buffer solution and in the presence of non-fibrillar and fibrillar lysozyme

Dye	Band	Buffer solution	LzC	LzF
	I	0.42	0.62	0.66
AK3-1	II	1.02	1.82	1.56
	III	1.53	1.48	1.73
	I	0.54	0.81	1.00
AK3-3	II	0.81	0.81	0.66
	III	-	2.00	2.30
AK3-5	I	0.67	0.66	0.88
	II	1.05	0.91	0.85
	I	0.67	0.75	0.85
AK3-7	II	0.59	1.21	1.27
	III	2.66	4.84	3.95
	I	0.45	0.72	0.84
AK3-8	II	0.75	1.20	1.03
	III	1.00	0.70	1.35
	I	0.91	1.69	0.83
AK3-11	II	0.76	0.77	0.61
	III	1.54	1.21	1.59

At the next step of the study the molecular docking technique was used to identify the trimethine-lysozyme binding sites. As represented in Figure 4, the trimethines tend to form the most stable complexes with deep cleft of the native lysozyme.
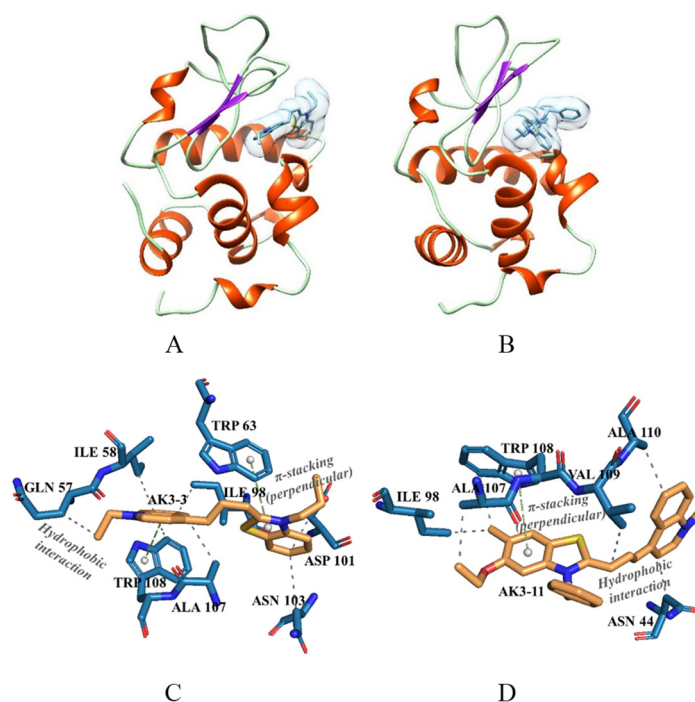

Figure 4. Most favorable modes of interactions between AK3-3 (A, C), AK3-11 (B, D) and native lysozyme obtained using the AutoDock (panels A, B) and PLIP (panels C and D). The grey dashed lines and green dashed line on the panels C and D represent the hydrophobic interactions and π-stacking contacts between the dye molecule and the lysozyme residues, respectively.

The free energy of cyanine – LzN binding was found to follow the order: AK3-11 (-8.18 kcal/mol) > AK3-1 (-7.90 kcal/mol) > AK3-3 (-7.78 kcal/mol) > AK3-7 (-7.42 kcal/mol) > AK3-5 (-7.34 kcal/mol) > AK3-8 (-7.01 kcal/mol). As judged from the PLIP analysis, the hydrophobic interactions play a significant role in the binding of cyanines to the non-aggregated lysozyme and involve Asn 44 (only AK3-11), Gln 57 (except AK3-5, AK3-11), Ile 58 (except AK3-8, AK3-11), Asn 59 (AK3-1), Trp 62 (AK3-5), Trp 63 (AK3-5, AK3-7, AK3-8), Leu 75 (AK3-5), Ile 98 (except AK3-8), Asp 101 (except AK3-7, AK3-11), Asn 103 (except AK3-8, AK3-11), Ala 107 (except AK3-7, AK3-8), Trp 108 (except AK3-7, AK3-8), Val 109 (AK3-8, AK3-11) and Ala 110 (AK3-11). Moreover, the trimethines were found to form π-stacking contacts between aromatic or cyclopentane ring of the cyanine and Trp in position 63 (in the case of AK3-1, AK3-3, AK3-5) and 108 (except AK3-7, AK3-8). The AK3-7, AK3-8 complexes with the native lysozyme are additionally stabilized by hydrogen bonds between the OH-groups of the trimethines and acceptor atoms of Asp 101 (AK3-7) and Gln 57 (AK3-8) of LzN.

Figure 5 represents the energetically most favorable cyanine complexes with the groove Gly 2-Leu 4/Ser 8-Trp 10 of the lysozyme fibril core, which are stabilised by hydrobhobic contacts with Leu 4, Trp 10 as well as π-stacking interactions between cyanine dyes and the side chains of the groove residues (Figure 5, panel B). In addition, the complexes of AK3-7 and AK3-8 with LzF are stabilized by hydrogen bonds involving Ile 3 (AK3-7, AK3-8) and Arg 9 (AK3-8). The binding energies appeared to be comparable with the native lysozyme and follow the order: AK3-11 (-7.78 kcal/mol) > AK3-3 (-7.11 kcal/mol) > AK3-1 (-6.74 kcal/mol) > AK3-5 (-6.59 kcal/mol) > AK3-7 (-6.43 kcal/mol) > AK3-8 (-6.13 kcal/mol).
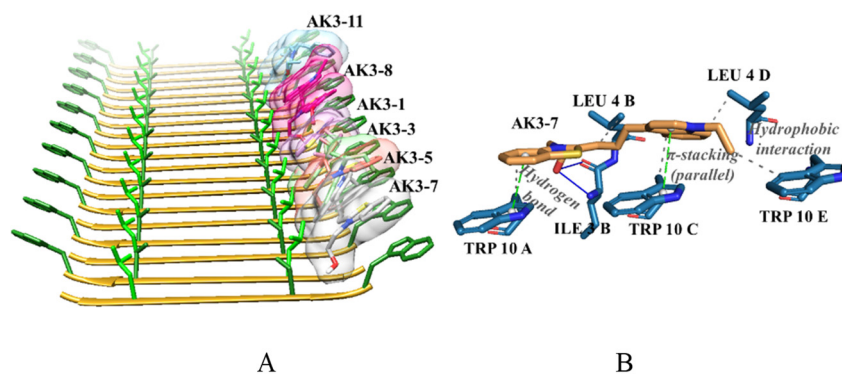

Figure 5. The complexes of trimethine dyes with the fibrillar lysozyme obtained using the AutoDock (A). Representative interactions between AK3-11 and groove Gly 2-Leu 4 / Ser 8-Trp 10 of the lysozyme fibril revealed by PLIP (B). The grey dashed lines on the panel B represent the hydrophobic interactions between the dye molecule and the groove, while the green dashed line and blue solid line display the π-stacking contacts and hydrogen bonds, respectively.

CONCLUSIONS

To summarize, in the present study the optical spectroscopy and molecular docking techniques were used to investigate the interactions between the trimethine cyanine dyes and lysozyme in the non-fibrillar and amyloid states. It was found that all cyanines under study are capable of distinguishing between the non-aggregated and fibrillar protein forms. The dyes AK3-7, AK3-5 and AK3-11 appeared to possess the highest amyloid sensitivity due to: i) significant fluorescence enhancement in the presence of LzF produced by the binding of the dye monomers to fibrillar lysozyme; ii) the lower binding affinity of the dye monomers to the nonfibrillar lysozyme in comparison with the aggregated protein. In turn, significantly lower ADF values observed for AK3-3, AK3-1 and AK3-8 were interpreted as arising from the binding of dye monomers to the nonfibrillar lysozyme. The fluorescence response of cyanines in the presence of lysozyme fibrils led us to conclude that the trimethine dyes under study are sensitive to the fibril morphology.

ORCID IDs
Olga Zhytniakivska, https://orcid.org/0000-0002-2068-5823; **Uliana Tarabara,** https://orcid.org/0000-0002-7677-0779
Atanas Kurutos, https://orcid.org/0000-0002-6847-198X; **Kateryna Vus,** https://orcid.org/0000-0003-4738-4016
Valeriya Trusova, https://orcid.org/0000-0002-7087-071X; **Galyna Gorbenko,** https://orcid.org/0000-0002-0954-5053

REFERENCES
[1]   P. Pronkin, and A. Tatikolov, Molecules, **27**(19), 6367 (2022). https://doi.org/10.3390/molecules27196367
[2]   M. Bokan, G. Gellerman, and L. Patsenker. Dyes Pigm. **171**, 107703 (2019). https://doi.org/10.1016/j.dyepig.2019.107703
[3]   M. Guo, P. Diao, Y.-J. Ren, F. Meng, H. Tian, and S.-M. Cai, Sol. Energy Mater. Sol. Cells, **88**, 33 (2005). https://doi.org/10.1016/j.solmat.2004.10.003

[4]   C. Shi, J.B. Wu, and D. Pan. J. Biomed. Opt. **21**(5), 05901 (2022). https://doi.org/10.1117/1.JBO.21.5.050901
[5]   G.D. Pelle, A.D. Lopez, and M.S. Fiol, Int. J. Mol. Sci. **22**(13), 6914, (2021). https://doi.org/10.3390/ijms22136914
[6]   O. Cavuslar, and H. Unal, RSC Advances, **5**, 22380 (2015). https://doi.org/10.1039/C5RA00236B
[7]   H.L. Yang, S.Q. Fang, Y.W. Tang, et al., Eur. J. Med. Chem. **179**, 736 (2019). http://dx.doi.org/10.1016/j.ejmech.2019.07.005
[8]   X. Mu, F. Wu, R. Wang, Z. Huang, et al., Sens Actuators B. Chemical. **338**, 29842 (2021). https://doi.org/10.1016/j.snb.2021.129842
[9]   K.D. Volkova, V.B. Kovalska, O.A. Balanda, R.J. Vermeij, V. Subramaniam, Y.L. Slominskii, and S.M. Yarmoluk, J. Biochem. Biophys. Methods, **70,** 727, (2007). https://doi.org/10.1016/j.jbbm.2007.03.008
[10] V.B. Kovalska, M.Yu. Losytskyy, O.I. Tolmachev, et al., J. Fluoresc. **22**, 1441 (2012). https://doi.org/10.1007/s10895-012-1081-x
[11] J. Yan, J. Zhu, K. Zhou, et al., Chem. Commun. **53**, 1441 (2017). https://doi.org/10.1039/C7CC05056A
[12] T. Smidlehner, H. Bonnet, S. Chierici, and I. Piantanida, Bioorg. Chem. **104,** 104196 (2020). https://doi.org/10.1016/j.bioorg.2020.104196
[13] R. Sabate, and J. Estelrich, Biopolymers, **72**(6), 455 (2003). https://doi.org/10.1002/bip.10485
[14] G.Q. Gao, A.W. Xu, RSC Adv. **3**, 21092 (2013). https://doi.org/10.1039/C3RA43259A
[15] O. Zhytniakivska, A. Kurutos, U. Tarabara, K. Vus, V. Trusova, G. Gorbenko, N. Gadjev, and T. Deligeorgiev, J. Mol. Liq. **311**, 113287 (2020), https://doi.org/10.1016/j.molliq.2020.113287
[16] S. Chernii, Y. Gerasymchuk, M. Losytskyy, D. Szymanski, et al., PLOS One, **16**(1), e0243904 (2021). https://doi.org/10.1371/journal.pone.0243904
[17] K. Vus, U. Tarabara, A. Kurutos, O Ryzhova, G. Gorbenko, et al., Mol. Biosyst. **13**(5), 1970 (2017). https://doi.org/10.1039/c7mb00185a
[18] H.L. Yang, S.Q. Fang, Y.W. Tang, et al. Eur. J. Med. Chem, **179**, 736 (2019). https://doi.org/10.1016/j.ejmech.2019.07.005
[19] K. Vus, M. Girych, V. Trusova, et al. J. Mol. Liq. **276**, 541 (2019). https://doi.org/10.1016/j.molliq.2018.11.149
[20] M. Bacalum, B. Zorila, and M. Radu, Anal. Biochem. **440**, 123 (2013). https:// doi.org/10.1016/j.ab.2013.05.031
[21] S. Dallakyan, and A.J. Olson, Methods Mol. Biol. **1263**, 243 (2015). https://doi.org/10.1007/978-1-4939-2269-7_19
[22] S. Salentin, S. Schreiber, V.J. Haupt, M.F. Adasme, and M. Schroeder, Nucleic Acids Res. **43**, W443 (2015), https://doi.org/10.1093/nar/gkv315.
[23] P. Csizmadia, in: *Proceedings of ECSOC-3, the third international electronic conference on synthetic organic chemistry*, edited by E. Pombo-Villar, R. Neier, and S.-K. Lin (MDPI, Basel, Switzerland, 1999), pp. 367-369. https://doi.org/10.3390/ECSOC-3-01775
[24] M.D. Hanwell, D.E. Curtis, D.C. Lonie, T. Vandermeersch, E. Zurek, and G.R. Hutchison, J. Cheminform. **4**, 17 (2012), https://doi.org/10.1186/1758-2946-4-17
[25] V. Trusova, East Eur. J. Phys. **2,** 51 (2015), https://periodicals.karazin.ua/eejp/article/view/4010/3568
[26] P.L. Donabedian, M. Evanoff, F.A. Monge, D.G. Whitten, and E.Y. Chi, ACS Omega, **2**, 3192 (2017). https://doi.org/10.1021/acsomega.7b00231

ДЕТЕКТУВАННЯ АМІЛОЇДНИХ ФІБРИЛ ЛІЗОЦИМУ ЗА ДОПОМОГОЮ ТРИМЕТИНЦІАНІНОВИХ БАРВНИКІВ: СПЕКТРОСКОПІЧНІ ДОСЛІДЖЕННЯ ТА МОЛЕКУЛЯРНИЙ ДОКІНГ
Ольга Житняківська[a], Уляна Тарабара[a], Анатас Курутос[b,c], Катерина Вус[a] , Валерія Трусова[a], Галина Горбенко[a]
[a]Кафедра медичної фізики та біомедичних нанотехнологій, Харківський національний університет імені В.Н. Каразіна м. Свободи 4, Харків, 61022, Україна
[b]Інститут органічної хімії та фітохімії Академії Наук Болгарії, Вул. Акад. Бончева, 9, 1113, Софія, Болгарія;
[c]Кафедра фармацевтичної та прикладної органічної хімії, Факультет хімії та фармації, Софійський університет імені Св. Климента Охридського, 1164, Софія, Болгарія;

Завдяки своїм унікальним фотофізичним і фотохімічним властивостям, а також їх високій чутливості до бета-складчастих мотивів, ціанінові барвники широко застосовуються як молекулярні зонди для ідентифікації та характеризації амілоїдних фібрил in vitro та візуалізації амілоїдних включень in vivo. В даній роботі, за допомогою спектроскопічних методів та молекулярного докінгу досліджено амілоїдну специфічність та механізми взаємодії між триметинціаніновими барвниками та нативним (LzN) і фібрилярним (LzF) лізоцимом. Встановлено, що асоціація триметину з нефібрилярним і фібрилярним білком супроводжується зміною ступеня агрегації барвників. Дослідження молекулярного докінгу між триметиновими барвниками та лізоцимом у нативному та амілоїдному станах показують, що: i) триметини мають тенденцію утворювати найбільш стабільні комплекси з «deep cleft» нативного лізоциму; ii) зв'язування барвника з нефібрилярним білком регулюється гідрофобними взаємодіями, π-стекінгом між ароматичним або циклопентановим кільцем ціаніну та Trp у положенні 63 або 108 та водневими зв'язками між ОН-групами триметинів і акцепторними атомами Asp 101 (АК3-7) і Gln 57 (АК3-8); iii) ціанінові барвники утворюють енергетично найбільш сприятливі комплекси з борозенкою Gly 2-Leu 4/Ser 8-Trp 10 ядра фібрили лізоциму; iv) взаємодія ціаніни-LzF стабілізується гідрофобними контактами, π-стекінговою взаємодією та водневими зв'язками. Барвники АК3-7, АК3-5 та АК3-11 були обрані як найбільш перспективні амілоїдні зонди.
Ключові слова: Триметинові ціанінові зонди, лізоцим, амілоїдні фібрили

A DEMONSTRATION BENCH FOR REPRESENTING THE CHARACTER OF PHASE TRANSITIONS OF THE FIRST AND SECOND KIND[†]

Ivan V. Gushchin

V.N. Karazin Kharkiv National University, Kharkiv, Ukraine
Svobody Sq. 4, Kharkiv, Ukraine, 61022
E-mail: i.v.gushchin@karazin.ua
Received October 1, 2022; revised November 22, 2022; accepted November 25, 2022

The paper presents the description of a demonstration bench, which includes a mathematical model and analysis tools for understanding the features of phase transitions of the first and second kind. The advantage of this demonstration bench is the rejection of all phenomenology and the obvious limitation of the application of various approximations and hypotheses. The description is formed on the well-known equations of hydrodynamics, which are well-tested and are a reliable basis for the construction of realistic models. The Proctor-Sivashinsky model, which was used to describe the process of convection development in a thin layer of liquid with poorly conductive heat boundaries, is the basis for the demonstration bench. Exactly this model allows to observe phase transitions of the first and second kind. The feature of the model is that it allocates one spatial scale of interaction, leaving for the evolution of the system the possibility to choose the nature of symmetry. All spatial disturbances of the same size but of different orientation interact with each other. This allows us not to distract from the main task of this work, which is to demonstrate the process of structure formation as a result of a cascade of phase transitions. The mechanism of phase transitions associated with the presence of minimums of the interaction coefficients of modes of the spectrum of the instability. There are a large number of structural defects, which appear as attributes of phase transition. The instability spectrum modes interference is the reason of the high rate of correlations in the propagation of a new phase.
Keywords: *demonstration, phase transitions of the first and second kind, Proctor-Sivashinsky equations*
PACS: 44.25.+f; 64.70.−p ; 64.70.Ja

INTRODUCTION

The process of convection development in a thin fluid layer has been considered in [1,2]. In this case a system of toroidal convective structures is formed, providing a significantly stronger heat transfer in the system. The authors of [3] noticed instabilities in this system, which were described by the Proctor Sivashinsky equations obtained in [1,2]. The Swift - Hohenberg equation, which was a simplification of the Proctor - Sivashinsky equations (instead of vector nonlinearity, the scalar one was used [4]) discussed the first kind phase transition in this description model. In this work and in work [5] the process of phase transition was discussed when from amorphous state of disorderly convection, the structure of convective rolls was formed, which in turns turned out to be unstable with formation of hexagonal convective cells.

By the way, the equations of the Proctor Sivashinsky model, after the instability of the primary structure - convective rolls, formed a system of square convective cells The question of the appearance of a phase transition of the first kind did not need to be discussed, but it remained unclear what the instability of the primary structure of convective shafts is and whether this process is a phase transition of the second kind. This is exactly what was found out later in [6-13], where the state function whose values determined the type of topology of emerging spatial structures was found and verified, the process of their formation was shown and thus it was proved that the that transition is nothing but a phase transition of the second kind (see also [14], which results in the formation of a more stable field of convective square cells [15-19]).

The aim of the work is to create a mathematical model and means of describing the bench to demonstrate the features of phase transitions of the first and second kind The advantage of this bench is the rejection of all phenomenology and the obvious limitation of the application of various approximations and hypotheses. The description is formed on the well-known equations of hydrodynamics, which are well-tested and are a reliable basis for the construction of realistic models.

1. MATHEMATICAL MODEL OF CONVECTION DEVELOPMENT IN A THIN LAYER OF LIQUID OR GAS WITH POORLY CONDUCTIVE HEAT BOUNDARIES

Below we consider the Proctor-Sivashinsky model [1-2], which was used to describe the process of convection development in a thin layer of liquid with poorly conductive heat boundaries. The feature of the model is that it allocates one spatial scale of interaction, leaving for the evolution of the system the possibility to choose the nature of symmetry. All spatial disturbances of the same size but of different orientation interact with each other. This allows us not to distract from the main task of this work, which is to study the process of structure formation as a result of a cascade of phase transitions Consider the simplest and most convenient representation of the Proctor-Sivashinsky model to describe this convection:

$$\frac{\partial A_j}{\partial t} = A_j - \sum_{i=1}^{N} V_{ij} \mid A_i \mid^2 A_j + f \ , \tag{1}$$

where the interaction coefficients are defined by the relations

$$V_{jj}=1, \qquad V_{ij}=(2/3)\left(1-2\left(\vec{k}_i\vec{k}_j\right)^2\right)=(2/3)\left(1+2\cos^2\vartheta_{ij}\right), \qquad (2)$$

and ϑ_{ij} – angle between the vectors $\vec{k}_i$ and $\vec{k}_j$. If we require zero values at the boundaries, the spatial dependence of each n - th mode will be $A_{n,m}\sin(2\pi nx)\sin(2\pi my)$ where n, m (they can be represented as $n = N \cdot \cos\vartheta_s$, $m = N \cdot \sin\vartheta_s$) – are integers, and $N^2 = n^2 + m^2$.

Expressions (1) - (2) must be supplemented with the initial values of the spectrum amplitudes A_j. That is $A_j\big|_{t=0} = A_{j_0}$. The width of the instability interval in k-space represents a ring – whose average radius is equal to one, and whose width is of the order of the value of the relative overthreshold $\mathcal{M}$, i.e., much less than one. From the results of preliminary studies [3] it became clear that in the system, besides the initial amorphous state, the existence of at least two long-lived solutions in the form of a roller structure (rolls) (see Fig. 1a), and in the form of a field of square cells (see Fig. 1b) is possible.
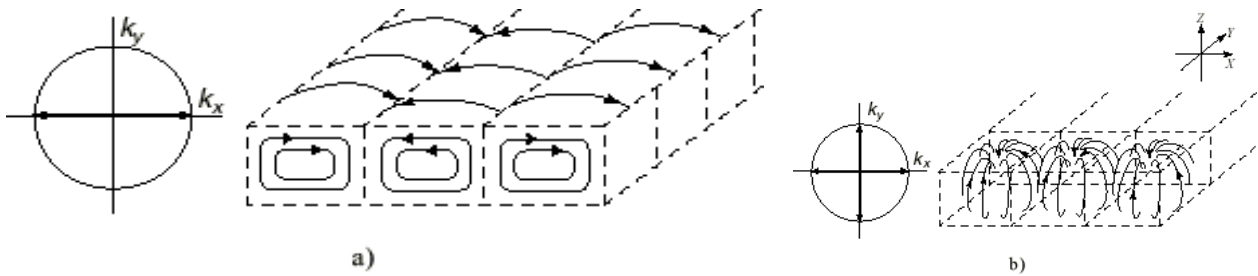

Figure 1. Convective structures: rolls (a) and square cells (b)

2. TOOLS TO DESCRIBE PHASE TRANSITIONS

Numerical analysis of the model allowed us to confirm the presence of structural-phase transitions. The state function turned out to be the quadratic form of the spectrum $I = \frac{1}{N}\sum_j A_j^2$.
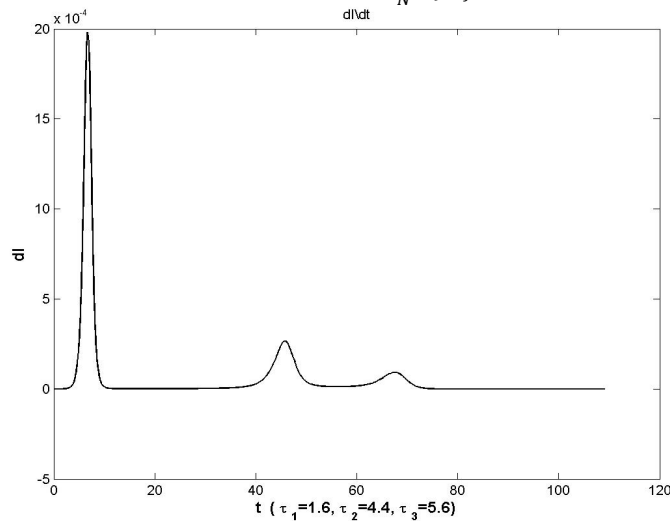

Figure 2. Behavior of the derivative state function $\partial I/\partial t$

After the first burst of the derivative $\partial I/\partial t$ an amorphous structure is formed - a system of convective rolls, and up to the second burst the value of $I \approx 0.75$ changes little. State function $I \to 1$ in the formation of a quasi-stable roller structure, later $I = 1.2$ - corresponds to the formed field of square cells. Characteristic transient times $\tau_1 = 1.6$ – the time of occurrence of the "amorphous" state $\tau_2 = 4.4$ – time of formation of pronounced roller-shaped structures $\tau_3 = 5.6$ – the time of cell system formation for one of the realizations of the process of establishing convective motion.

It can be seen that the formation times of the states τ_n is inversely proportional to the difference between the values of $I = \sum_i A_i^2$ after the structural-phase transition $I_n^{(+)} = (\sum_i A_i^2)_n^{(+)}$ and before this transition $I_n^{(-)} = (\sum_i A_i^2)_n^{(-)}$. That is,

$$\tau_n \propto \left\{\left(\sum A_i^2\right)_n^{(+)} - \left(\sum A_i^2\right)_n^{(-)}\right\}^{-1} = \Delta I_n^{-1}. \qquad (3)$$

It is easy to see that $\tau_3/\tau_2 \approx \Delta I_2/\Delta I_3$, faster phase transitions precede slower ones. By tracking the values of the state function, we can see at what stage of the process development the convective layer is.

3.   VISUALIZATION OF PHASE TRANSITIONS PROCESSES

The demonstration model must form a physical intuition, so the role of visualization of the phase transition process is very important. Consider the view of large fragments of the field of convective structures, calculated [20] using the mathematical model outlined in Section 1.
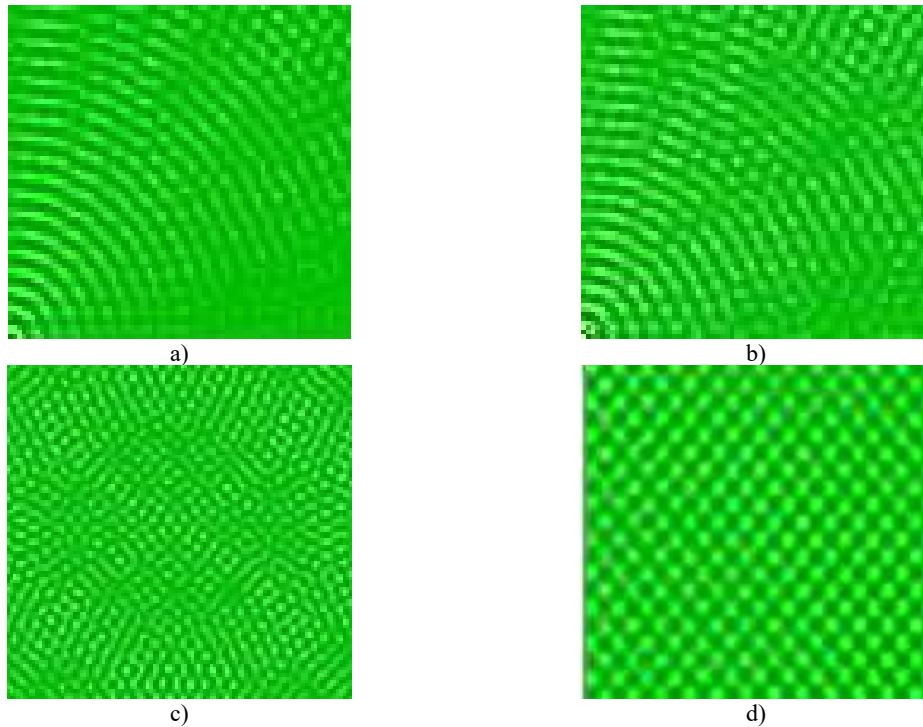
a)

b)

c)

d)

Figure 3. Temperature field distribution of convection on the layer surface

Segment (a) shows what happens after the first-order phase transition with the formation of convective rolls. The next segment (b) shows the dynamics of transverse modulation of the rolls. This is already the initial stage of the phase transition of the second kind. Segment (c) shows the process of nucleation of a new phase - formation of domains - a metastable spatial structure, after destruction of the roll system, Segment (d) demonstrates formation of a stable convective structure - square convective cells.

4.   CONCLUSIONS

Thus, there are three states in the Proctor-Sivashinsky model of description of convection. The times of phase transitions between metastable states are much shorter than the times of their existence. Characteristic size of convective structures in the regime of extended instability in accepted order units $2\pi/k \propto 2\pi$ and the length of the wave vectors of the order of one. Interaction potential of spatial modes $V_{ij} = (2/3)(1 + 2\cos^2 \vartheta_{ij})$ has a deep minimum for corners $\vartheta_{ij} = \vartheta_i - \vartheta_j$ between the vectors $\vec{k}_i$ and $\vec{k}_j$ of two spatial modes $\vartheta_{ij} = \pm \pi/2$. Exactly these minima generate the unstable structure of rolls. For the existence of a minimum V_{ij} allows modes with relatively small amplitudes to continue their growth, while suppressing the neighboring disturbances.

When approaching a stable or metastable state, the spatial structure gets rid of many defects.

Defects occur mostly on the boundaries of homogeneous areas - domains. There is a correlation between the relative proportion of visually observed (geometrically) structure defects and the defectiveness value, defined as the ratio of the squares of the amplitudes of the spectrum modes that do not correspond to the square cell system to the total sum of the squares of amplitudes (see [12, 13]).

Thus, in the model of convection, Proctor-Sivashinsky it is possible to observe both the process of phase transition of the first kind and the process of phase transition of the second kind. This description of phase transitions did not use phenomenological approaches and various speculative considerations, which allows us to consider in detail the nature of the transition processes by the example of this model.

It is important to note that the correlation speed of spatial perturbations in this case is extremely large. The process of phase transformations covers not separate local regions, but at once the entire convection zone, the spatial structure in different places of the convective layer being a consequence of interference of a set of eigenfunctions of the task. That is, the observed significant rate of these correlations is due to phase changes and is not related to the energy-momentum transfer.

ORCID ID

Ivan V. Gushchin, https://orcid.org/0000-0002-1917-716X

REFERENCES

[1]   J. Chapman, and M.R.E. Proctor "Nonlinear Rayleigh-Benard convection between the poorly conducting boundaries", J. Fluid Mech. **101**, 759 (1980). https://doi.org/10.1017/S0022112080001917

[2]   V. Gertsberg, and G.E. Sivashinsky, "Large cells in nonlinear Rayleigh-Benard convection", Prog. Theor. Phys. **66**, 1219 (1981). https://doi.org/10.1143/PTP.66.1219

[3]   B.A. Malomed, A.A. Nepomnyashchy, and M.P. Tribelsky, "Twodimensional quasiperiodic structures in nonequilibrium systems", ZhETF, **96**, 684 (1989).

[4]   J.V. Swift, and P.C. Hohenberg, "Hydrodynamic fluctuations at the convective instability", Phys. Rev. A, **15**, 319 (1977). https://doi.org/10.1103/PhysRevA.15.319

[5]   M.I. Rabinovich, A.L. Fabrikant, and L.S. Tsimring, "Finite Dimensional Disorder", UFN, **162**(8), 1–42 (1992).

[6]   E.V. Belkin, I.V. Gushchin, A.V. Kirichok, and V.M. Kuklin, "Structural transitions in the Proctor-Sivashinsky model", PAST, **68**, 296 (2010). (in Russian). https://vant.kipt.kharkov.ua/ARTICLE/VANT_2010_4/article_2010_4_296.pdf

[7]   I.V. Gushchin, A.V. Kirichok, and V.M. Kuklin, "Pattern Transitions in Unstable Viscous Convective Medium", https://doi.org/10.48550/arXiv.1311.3884

[8]   I.V. Gushchin, A.V. Kirichok, and V.M. Kuklin "Pattern formation in convective media", «Journal of Kharkiv National University», physical series «Nuclei, Particles, Fields», **1040**(1), 4-27 (2013). http://nuclear.univer.kharkov.ua/lib/1040_1(57)_13_p04-27.pdf

[9]   I.V. Gushchin, A.V. Kirichok, and V.M. Kuklin, "Pattern formation in unstable viscous convective medium", PAST, **4**, 251 (2013). https://vant.kipt.kharkov.ua/ARTICLE/VANT_2013_4/article_2013_4_251.pdf

[10] I.V. Gushchin, A.V. Kirichok, and V.M. Kuklin, "Structural-phase transitions and state function in unstable convective medium", PAST, **4**, 252 (2015). https://vant.kipt.kharkov.ua/ARTICLE/VANT_2015_4/article_2015_4_252.pdf

[11] I.V. Gushchin, A.V. Kirichok, and V.M. Kuklin, "State function in unstable convective medium", East Eur. J. Phys. **2**(1), 32 (2015). https://periodicals.karazin.ua/eejp/article/view/2811/2550

[12] I.V. Gushchin, and V.M. Kuklin, "Structural phase transition in thin convection at dependence of viscosity on temperature", PAST, **4**, 256 (2018). https://vant.kipt.kharkov.ua/ARTICLE/VANT_2018_4/article_2018_4_256.pdf

[13] I.V. Gushchin, V.M. Kuklin, and E.V. Poklonskiy, "Phase transitions in convection", East Eur. J. Phys. **4**, 34-40 (2019). https://doi.org/10.26565/2312-4334-2019-4-03

[14] V.M. Kuklin, *Selected chapters (theoretical physics)*, (V.N. Karazin KhNU, Kharkiv, 2021). pp. 244. http://dspace.univer.kharkov.ua/handle/123456789/16359

[15] L. Pismen, "Inertial effects in long-scale thermal convection", Phys. Lett. A, **116,** 241–243 (1986). https://doi.org/10.1016/0375-9601(86)90141-6

[16] A.V. Kirichok, V.M. Kuklin, I.P. Panchenko, S.S. Moiseev, and L.M. Pismen, "Dynamics of large-scale vortices formation in regime of convective instability", in: *International Conference "Physics in Ukraine"*, (Bogolyubov Institute of Theor. Phys., Kiev, 1993), pp. 130-135. https://inis.iaea.org/collection/NCLCollectionStore/_Public/25/076/25076395.pdf

[17] A.V. Kirichok, V.M. Kuklin, and I.P. Panchenko, "On the possibility of dynamo mechanism in a nonequilibrium convective medium", Reports of NASU, **4**, 87–92 (1997). (in Russian)

[18] A.V. Kirichok, and V.M. Kuklin, "Allocated Imperfections of Developed Convective Structures", Physics and Chemistry of the Earth Part A, **6**, 533–538 (1999). https://www.sciencedirect.com/science/article/abs/pii/S1464189599000678

[19] S.S. Moiseev, K.R. Oganesyan, P.B. Rutkevich, A.V. Tur, G.A. Khomenko, and V.V. Yanovskiy, "Vortex dynamo in spiral turbulence", in: *Integrability and kinetic equations for solitons*, edited by V.G. Bar'yakhtar, V.E. Zakharova, and V.M. Chernousenko. Sat. scientific. (in Russian), http://smiswww.iki.rssi.ru/files/publications/rutkevich/jetf_1988_2_94.pdf

[20] I.V. Gushchin, V.M. Kuklin, O.V. Mishin, and O.V. Priymak, "Model of physical processes due of CUDA technology", (V.N. Karazin KhNU, Kharkiv, 2017), pp. 116. (in Ukrainan). https://cutt.ly/UMH5G8f

ДЕМОНСТРАЦІЙНИЙ СТЕНД ДЛЯ ПРЕДСТАВЛЕННЯ ХАРАКТЕРУ ФАЗОВИХ ПЕРЕХОДІВ ПЕРШОГО І ДРУГОГО РОДУ

І.В. Гущин
Харківський національний університет імені В. Н. Каразіна, Харків, Україна
пл. Свободи 4, м Харків, Україна, 61022

В роботі представлено опис демонстраційного стенду, що включає математичну модель і засоби аналізу для розуміння особливостей фазових переходів першого і другого роду. Перевагою цього демонстраційного стенду є відмова від будь-якої феноменології та очевидна обмеженість застосування різних наближень та гіпотез. Опис будується на відомих рівняннях гідродинаміки, які добре апробовані та є надійною основою для побудови реалістичних моделей. В основу демонстраційного стенду покладено модель Проктора-Сивашинського, яка використовувалася для опису процесу розвитку конвекції в тонкому шарі рідини з межами, що погано проводять тепло. Саме ця модель дозволяє спостерігати фазові переходи першого та другого роду. Особливість моделі у цьому, що вона виділяє один просторовий масштаб взаємодії, залишаючи для еволюції системи можливість вибору характеру симетрії. Усі просторові обурення одного розміру, але різної орієнтації взаємодіють друг з одним. Це дозволяє не відволікатися від основного завдання даної роботи – демонстрації процесу структуроутворення внаслідок каскаду фазових переходів. Механізм фазових переходів пов'язаний із наявністю мінімумів коефіцієнтів взаємодії мод спектру нестійкості. Є велика кількість структурних дефектів, які виявляються ознаки фазового переходу. Інтерференція мод спектру нестабільності є причиною високої швидкості кореляцій поширення нової фази.

Ключові слова: демонстрація, фазові переходи першого та другого роду, рівняння Проктора-Сивашинського

INSTRUCTIONS FOR PREPARING MANUSCRIPT IN THE EAST EUROPEAN JOURNAL OF PHYSICS

Nikita F. Author[a],*, Peter V. Co-Author(s)[b],†

[a]Affiliation of first author
[b]Affiliation of second author (if different from the first Author)
*Corresponding Author: corresponding_authors@mail.com, [a]ORCID ID
†E-mail: co_authors@mail.com, [b]ORCID ID

Each paper must begin with an abstract. The abstract should be typed in the same manner as the body text (see below). Please note that these Instructions are typed just like the manuscripts should be. The abstract must have at least **1800 phonetic symbols (about 250-300 words)**, supplying general information about the achievements, and objectives of the paper, experimental technique, methods applied, significant results and conclusions. Page layout: the text should be printed on the paper **A4** format, at least **5 pages**, with margins of: **Top - 3, Bottom, Left and Right - 2 cm**. The abstract, keywords should be presented **in English** (only for foreign authors), **and Ukrainian**.

Keywords: there, must, be, 5-10 keywords
PACS: specify PACS code(s) here

This is **Introduction** section. This paper contains instructions for preparing the manuscripts. The text should be prepared in "**doc**" or "**docx**" format.

INSTRUCTIONS

The text should be typed as follows:
• **title**: Times New Roman, 12 pt, ALL CAPS, bold, 1 spacing, centred;
• **authors**: name, initials and family names; Times New Roman, 12 pt, bold, 1 spacing, centred;
• **affiliation(s)**: Times New Roman, 9 pt, italic, 1 spacing, centred;
• **abstract**: Times New Roman, 9 pt, 1 spacing, justified;
• **body text**: Times New Roman, 10 pt, 1 spacing, justified; paragraphs in sections should be indented right (tabulated) for 0.75 cm;
• **section titles**: Times New Roman, 10 pt, bold, 1 spacing, centred, without numbering, one line should be left, blank above section title;
• **subsection titles**: Times New Roman, 10 pt, bold, 1 spacing, centred, without numbering in accordance to the section (see below), one line should be left blank above subsection title;
• **figure captions**: width of the figure should be 85 or 170 mm, Figures should be numbered (**Figure 1**.) and titled below Figures using sentence format, Times New Roman, 9 pt, 1 spacing, centred (if one line) or justified (if more than one line); one line should be left blank below figure captions;
• **table captions**: width of the table should be 85 or 170 mm, tables should be numbered (**Table 1.**) and titled above tables using sentence format, Times New Roman, 10 pt, 1 spacing, justified, Tables should be formatted with a single-line box around the outside border and single ruling lines between rows and columns; one line should be left blank below tables;
• **equations**: place equations centred, numbered in Arabic: (1), the number is aligned to the right; equations should be specially prepared in **MathType** or "**Microsoft Equation**", Times New Roman, 10 pt, one line should be left blank below and above equation.

Additional instructions

Numerated figures and tables should be embedded in your text and placed after they are cited. Only sharp photographs and drawings are acceptable. Letters in the figures should be 3 mm high. The figures should be presented in one of the following graphic formats: jpg, gif, pcx, bmp, tif.

REFERENCES

List of References must contain **at least 50% of articles published over the past 5 years** and **no more than 20% of links to their own work**. Cite References by number in AIP style (https://aip.scitation.org/php/authors/manuscript). Numbering in the order of referring in the text, e.g. [1], [2-5], etc. References should be listed in numerical order of citation in the text at the end of the paper (justified), Times New Roman, 9 pt, 1 spacing:

Journal Articles
[1] T. Mikolajick, C. Dehm, W. Hartner, I. Kasko, M.J. Kastner, N. Nagel, M. Moert, and C. Mazure, Microelectron. Reliab. **41**, 947 (2001), https://doi.org/10.1016/S0026-2714(01)00049-X.
[2] S. Bushkova, B.K. Ostafiychuk, and O.V. Copaiev, Physics and Chemistry of Solid State. **15**(1), 182 (2014), http://page.if.ua/uploads/pcss/vol15/!1501-27.pdf. (in Ukrainian)
[3] M. Yoshimura, E. Nakai, K. Tomioka, and T. Fukui, Appl. Phys. Lett. **103**, 243111 (2013), http://dx.doi.org/10.7567/APEX.6.052301.

E-print Resourses with Collaboration Research or Preprint
[4] M. Aaboud et al. (ATLAS Collaboration), Eur. Phys. J. C, **77**, 531 (2017), http://dx.doi.org/10.1140/epjc/s10052-017-5061-9
[5] Sjöstrand et al., *Comput. Phys. Commun.* **191,** 159 (2015), https://doi.org/10.1016/j.cpc.2015.01.024.
[6] Boudreau, C. Escobar, J. Mueller, K. Sapp, and J. Su, (2013), http://arxiv.org/abs/1304.5639.

Books
[7] S. Inoue, and K.R. Spring, *Video Microscopy*: *The fundamentals*, 2nd ed. (Plenum, New York, 1997), pp. 19-24.
[8] I. Gonsky, T.P. Maksymchuk, and M.I. Kalinsky, *Біохімія Людини [Biochemistry of Man]*, (Ukrmedknyga, Ternopil, 2002), pp. 16. (in Ukrainian)

Edited Books
[9] Z.C. Feng, editor, *Handbook of Zinc Oxide and Related Materials: Devices and Nano Engineering, vol. 2*, (CRC Press/Taylor & Francis, Boca Raton, FL, 2012)

Book Chapters
[10] P. Blaha, K. Schwarz, G.K.H. Madsen, D. Kvasnicka, and J. Luitz, in: *WIEN2K, An Augmented Plane Wave Plus Local Orbitals Program for Calculating Crystal Properties,* edited by K. Schwarz (Techn. Universität Wien, Austria, 2001).
[11] M. Gonzalez-Leal, P. Krecmer, J. Prokop, and S.R. Elliot, in: *Photo-Induced Metastability in Amorphous Semiconductors*, edited by A.V. Kolobov (Wiley-VCH, Weinheim, 2003), pp. 338-340.
[12] A. Kochelap, and S.I. Pekar, in: *Теория Спонтанной и Стимулированной Хемилюминесценции Газов [Theory of Spontaneous and Stimulated Gas Chemiluminescence]* (Naukova dumka, Kyiv, 1986), pp. 16-29. (in Russian)

Conference or Symposium Proceedings
[13] C. Yaakov, and R. Huque, in: *Second International Telecommunications Energy Symposium Proceedings*, edited by E. Yow (IEEE, New York, 1996), pp. 17-27.
[14] V. Nikolsky, A.K. Sandler, and M.S. Stetsenko, in: *Автоматика-2004: Матеріали 11 Міжнародної Конференції по Автоматичному Управлінню [Automation-2004: Materials of the 11th International Conference on Automated Management]* (NUHT, Kyiv, 2004), pp. 46-48. (in Ukrainian)

Patent
[15] I.M. Vikulin, V.I. Irha, and M.I. Panfilov, Patent Ukraine No. 26020 (27 August 2007). (in Ukrainian)

Thesis / Dissertation
[16] R.E. Teodorescu, Ph.D. dissertation, The George Washington University, 2009.

Special Notes
1. Use International System of Units (SI system). 2. It is undesirable to use acronyms in the titles. Please define the acronym on its first use in the paper. 3. Refer to isotopes as ^{14}C, ^{3}H, ^{60}Co, etc.

Наукове видання

СХІДНО-ЄВРОПЕЙСЬКИЙ ФІЗИЧНИЙ ЖУРНАЛ
Номер 4, 2022

EAST EUROPEAN JOURNAL OF PHYSICS
No 4, 2022

Збірник наукових праць
англійською та українською мовами